

THE SLOAN DIGITAL SKY SURVEY PHOTOMETRIC CAMERA

J. E. GUNN,¹ M. CARR,² C. ROCKOSI,³ M. SEKIGUCHI,⁴ K. BERRY, B. ELMS, E. DE HAAS, Ž. IVEZIĆ, G. KNAPP, R. LUPTON,
 G. PAULS, AND R. SIMCOE

Department of Astrophysical Sciences and Princeton University Observatory, Peyton Hall, Princeton, NJ 08544

R. HIRSCH, D. SANFORD, S. WANG, AND D. YORK

Department of Astronomy and Astrophysics, University of Chicago, 5640 South Ellis Avenue, Chicago, IL 60637

F. HARRIS

US Naval Observatory, Flagstaff Station, P.O. Box 1149, Flagstaff, AZ 86002

J. ANNIS, L. BARTOZEK, W. BOROSKI, J. BAKKEN, M. HALDEMAN, S. KENT, S. HOLM, D. HOLMGREN, D. PETRAVICK,
 A. PROSAPIO, AND R. RECHENMACHER

Fermi National Accelerator Laboratory, P.O. Box 500, Batavia, IL 60510

M. DOI,⁵ M. FUKUGITA,^{4,6} AND K. SHIMASAKU⁵

Department of Astronomy, School of Science, University of Tokyo, Bunkyo-ku, Tokyo 113, Japan

N. OKADA

National Astronomical Observatory, Mitaka, Tokyo 181, Japan

C. HULL, W. SIEGMUND, AND E. MANNERY

Department of Astronomy, University of Washington, Box 351580, Seattle, WA 98195

M. BLOUKE AND D. HEIDTMAN

Scientific Imaging Technologies, Inc., P.O. Box 569, Beaverton, OR 97075-0569

D. SCHNEIDER

Department of Astronomy and Astrophysics, Pennsylvania State University, 525 Davey Laboratory, University Park, PA 16802

AND

R. LUCINIO AND J. BRINKMAN

Apache Point Observatory, 2001 Apache Point Road, P.O. Box 59, Sunspot, NM 88349

Received 1998 June 12; revised 1998 August 24

ABSTRACT

We have constructed a large-format mosaic CCD camera for the Sloan Digital Sky Survey. The camera consists of two arrays, a photometric array that uses 30 2048 × 2048 SITE/Tektronix CCDs (24 μm pixels) with an effective imaging area of 720 cm² and an astrometric array that uses 24 400 × 2048 CCDs with the same pixel size, which will allow us to tie bright astrometric standard stars to the objects imaged in the photometric camera. The instrument will be used to carry out photometry essentially simultaneously in five color bands spanning the range accessible to silicon detectors on the ground in the time-delay-and-integrate (TDI) scanning mode. The photometric detectors are arrayed in the focal plane in six columns of five chips each such that two scans cover a filled stripe 2°5 wide. This paper presents engineering and technical details of the camera.

Key words: astrometry — atlases — catalogs — cosmology: observations —
 instrumentation: detectors — instrumentation: photometers — surveys

1. INTRODUCTION

The Sloan Digital Sky Survey (SDSS) is a project undertaking a digitized photometric survey of half the northern sky to about 23d magnitude and a follow-up spectroscopic survey of 1 million galaxies and 100,000 quasars within precisely defined selection criteria. This project aims at producing a large homogeneous data sample of the northern sky with high-accuracy multicolor photometry and accurate astrometry. A wide-field telescope with accurate

and well-understood astrometric properties and very precise drives, a large-format imaging camera, a high multiplex gain multiobject spectrograph, and a data and software system capable of dealing with the high data rates and voluminous data are the indispensable elements for this project.

For the camera, we have constructed a large array of large-format CCD detectors mosaicked on the focal plane of a dedicated 2.5 m telescope with a new modified distortion-free Ritchey-Chrétien optical design. Our requirements for optical performance are quite demanding: for a large-area survey, it is crucial to realize a wide field of view for efficient photometric imaging, and fast final focal ratios for reasonable telescope apertures in order to match the pixel size for available CCD detectors. It is known that a wide, flat field of view can be achieved with a Ritchey-Chrétien design with two hyperboloids with the same curvature (Bowen & Vaughan 1973). The most successful telescope of this type is the Swope 1 m at Las Campanas, which has a 2°9 field of view (FOV) with a final focal ratio of

¹ jeg@astro.princeton.edu.

² Princeton University Observatory, Princeton, NJ 08544.

³ Department of Astronomy and Astrophysics, University of Chicago, Chicago, IL 60637.

⁴ Institute for Cosmic Ray Research, University of Tokyo, Tanashi, Tokyo 188, Japan.

⁵ Department of Astronomy, University of Tokyo, Hongo, Tokyo 113, Japan.

⁶ Institute for Advanced Study, Princeton, NJ 08540.

f/7. The SDSS telescope has a diameter of 2.5 m with a faster final focal ratio (f/5) and a slightly larger field (3°).

Our demands for optical performance are substantially more difficult to realize than are typically required in astronomical systems. We plan to carry out time-delay-and-integrate (TDI) drift scans in the imaging survey in order to increase the observing efficiency. TDI saves both the readout time of the CCD, which would be comparable to the exposure time in ordinary “snapshot” mode, and repointing and settling time. We will also thereby achieve very good flat-fielding, because the flat field becomes a one-dimensional vector; defects along a column are averaged over. This imaging technique requires carefully controlled distortion, since either a change of scale or a differential deviation from conformality of the mapping of the sky onto the focal plane across a chip immediately causes image degradation. Distortion is not normally an aberration of much concern to astronomers, and the classical optical systems used in astronomy are generally not very well corrected for it; in particular, the Gascoigne corrector used to correct astigmatism in the usual Ritchey arrangement introduces distortion that is more than an order of magnitude larger than would be acceptable for our configuration.

We therefore developed a new Ritchey-like design using two aspheric corrector lenses, one of the classical Gascoigne Schmidt-plate shape about 75 cm in front of the focal plane and the other, quite thick, with a negative Schmidt-plate form and much more strongly figured, just in front of the focal plane. This combination works by virtue of the fact that the astigmatism introduced by a Gascoigne plate is proportional to its aspheric amplitude and the square of the distance from the focal plane, whereas the distortion is proportional to the amplitude and the first power of the distance from the focal plane. Thus two correctors of opposite sign and different distances from the focus can both accurately remove astigmatism and distortion. It is fortuitous that the same combination also removes residual lateral color, which has the same dependence on the parameters as distortion. The focal surface is almost flat, deviating from a plane by less than 1.3 mm over the full 3° (650 mm) field. The optical design, its optimization for this configuration, and the desiderata that led to it will be described more fully in another publication.

The efficiency of a large-area survey is characterized by the quantity

$$\epsilon = \Omega D^2 q, \quad (1)$$

where Ω is the solid angle of the FOV, D is the diameter of the telescope, and q is the detective quantum efficiency on the sky, assuming that the seeing disk is resolved; all else being equal, the time to completion to a given depth depends inversely on ϵ . The SDSS attains $\epsilon = 4.8 \text{ m}^2 \text{ deg}^2$, which is comparable to $\approx 0.3 \text{ m}^2 \text{ deg}^2$ for 48 inch Schmidt photography. This gain enables us both to go significantly deeper than existing photographic surveys and to carry out imaging simultaneously in five color bands, which cover the wavelength range from the atmospheric cutoff in the ultra-violet to the silicon cutoff in the infrared. The bands we have chosen are u' ($\lambda_{\text{eff}} = 3550 \text{ \AA}$), g' ($\lambda_{\text{eff}} = 4770 \text{ \AA}$), r' ($\lambda_{\text{eff}} = 6230 \text{ \AA}$), i' ($\lambda_{\text{eff}} = 7620 \text{ \AA}$), and z' ($\lambda_{\text{eff}} = 9130 \text{ \AA}$). This is a new photometric system to optimize the physical advantages of each color band appropriate for the galaxy survey. Further details of the photometric system are available in Fukugita et al. (1996).

The system design was based on the then largest available CCD detectors, the Tektronix (later SITE) Tk2048E, which have a 2048×2048 array of $24 \mu\text{m}$ pixels. The focal length of the telescope is designed to match this device; the image scale $16''.5 \text{ mm}^{-1}$ corresponds to $0''.4$ per $24 \mu\text{m}$ pixel. With the $0''.8$ median free-air seeing measured at the Apache Point Observatory site, one expects about $1''.0$ FWHM images taking into account other items in the error budget. This represents quite excellent sampling, with less than 1% of the power in a star beyond the Nyquist frequency.

We can accommodate in our 3° field a $5 \text{ (colors)} \times 6 \text{ (columns)}$ array of 2048×2048 chips with an appropriate spacing among the chips; the active area of the devices is 49.15 mm (13.52), the CCD packages are 63.5 mm square, and the center-to-center spacing along a column is 65 mm, about $18''.0$. The center-to-center spacing between columns is 91 mm, about $25''.2$, slightly less than twice the active width of the chips, so that two scans cover a filled stripe $2''.54$ wide, with an 8% (about $1''$) overlap between the two scans along each edge. We will scan at sidereal rate, so the effective exposure time is 54.1 s for each of the five colors along a column; a star remains on the photometric array for 342 s, and the spacing in time from one color to the next is 72 s. The limiting magnitudes (defined to be at a signal-to-noise ratio $S/N = 5$) in an AB system for the five colors are expected to be about 22.1 for u' , 23.2 for g' , 23.1 for r' , 22.5 for i' , and 20.8 for z' for stellar images at an air mass of 1.4, near the planned median for the survey.

We use the extra space in the focal plane above and below the photometric array to arrange 22 smaller CCD chips (2048×400 with $24 \mu\text{m}$ pixels) for astrometry and two more as monitors for automated focusing. These are arrayed (see Fig. 1) in a dewar with 12 devices above (the *leading* astrometric array) the photometric array and another (the *trailing* astrometric array) identical array of 12 below the main array. The 11 astrometric devices in one dewar are arranged in two rows, one of six aligned with the photometric columns (the *column chips*) and a second of five (the *bridge chips*) straddling the columns. The centers of the first row and second row of astrometric devices are 204.5 and 220 mm, respectively, above and below the center of the field. The astrometric CCDs have passband filters nominally identical to the r' ones and 3.0 mag of neutral-density filters as well. Data from the astrometric array enable us to tie the coordinates of the objects observed in the photometric camera to the reference astrometric system which is based on bright stars that would saturate the photometric camera in the survey mode. The choice of filters for the astrometric devices is such that there is a roughly 3 mag range of useful overlap between them and the photometric array. The two focus devices, whose centers are 235.5 mm above and below the center, have r' filters as well, though no neutral filters, and have a three-piece stepped thickness plate incorporated into the filter. Though they are pretty far out in the field, the optical design (largely fortuitously) delivers excellent images there at the relevant wavelength, and one can do very critical focusing. The trailing astrometric array not only increases the astrometric precision by a factor of $\sqrt{2}$ but allows accurate monitoring of the tracking of the telescope.

Though we believe that this camera is the largest and most complex of its kind now extant and operating, there are many other cameras operating, near operation, or under construction that are at similar levels of complexity. The

National Astronomical Observatory, Tokyo, mosaic, (Sekiguchi et al. 1992; Kashikawa et al. 1995) based on $1K \times 1K$ TIJ virtual-phase devices, has been in operation in various guises for several years and now is using 40 CCDs, though they cannot be read simultaneously. The MOA mosaic (Abe et al. 1997) is a smaller array using these chips. Another large array using relatively small devices is the ESO one used for microlensing searches (Arnaud et al. 1994). Tyson's group has built and has been using for some years a camera with four of the $2K \times 2K$ devices like ours (Wittman et al. 1998). Most of the attention now is on mosaics of three-side buttable $2K \times 4K$ devices with $15 \mu m$ pixels being produced or promised by several manufacturers, including SITE, Lincoln Laboratories, Orbit, EEV, Hammamatsu, and Loral. Cameras using these devices either in operation or in advanced stages of testing have been described by Abe et al. (in preparation, 3×1), Ives et al. (1996; 4×1), Luppino et al. (1996; 4×2), and Boroson et al. (1994; 4×2). Another relatively large pair of arrays, the EROS cameras, each using eight $2K \times 2K$ Loral devices, are described in Bauer & de Kat (1998). Even larger cameras are planned using the $2K \times 4K$ devices, including a 2×5 array for Subaru (Miyazaki et al. 1998) and the Canada-France-Hawaii Telescope "MEGACAM" project (Boulade 1998), using an 8×4 array, which will be larger in terms of total pixels than the SDSS camera. Two large mosaics of these chips will be used in the DEIMOS spectrograph for the Keck telescope (James et al. 1998).

The field of our system is so large that one must perform the TDI scans along great circles in order to obtain satisfactory image quality, but the ability to park the telescope on the equator and take data is perceived by all to be a great advantage both for testing and for obtaining the highest astrometric accuracy, and was a significant driver in the choice of the scanning rate. The SDSS will make use of this in our southern survey, in which a stripe one full camera width ($2^\circ.5$) wide and about 90° long on the equator will be imaged in this fashion repeatedly when the northern Galactic cap is inaccessible.

We are aiming for high astrometric accuracy: Kolmogorov seeing theory with parameters relevant to our site suggests that we should be limited by seeing at about the 30–40 mas level, and we have striven to be in a position so that seeing will be the limiting factor in astrometric performance, both in the design and construction of the camera and the telescope and in the design, specification, and construction of the telescope drives, mirror supports, and controls. Thirty milliarseconds corresponds to $2 \mu m$ in the focal plane, and stability at this level is not trivial to achieve over such a large focal plane.

Thus the problem of the design of the camera comes down to housing the 54 detectors in a way that is geometrically stable at the level of a few microns, adjustable to conform to the focal surface, allows them to work cooled to CCD operating temperature (about $-80^\circ C$) in a good vacuum, and attend to their complex electronic needs with sufficiently modular and compact circuitry that assembly and maintenance are not an impossible nightmare. This has been altogether a rather challenging set of problems, and in this paper we discuss how they have been solved.

The plan of this paper is as follows: In § 2, we briefly review the telescope optics insofar as they are relevant to the camera. In § 3, we discuss the photometric system and the characteristics of the CCD chips. Section 4 describes the

mechanical design of the photometric array, and § 5 the astrometric array and focus monitor. There is a discussion of the CCD cooling system in § 6, and the electronics is detailed in § 7. The overall mechanical structure of the camera, its "life-support" system, and its mounting to the telescope is discussed in § 8.

2. TELESCOPE OPTICS: DESIGN AND PERFORMANCE

We have reviewed the principles of the optical design in the introduction; here we concentrate only on those details relevant to the design of the camera, namely, the final distortion corrector, the form of the focal surface, and the imaging performance.

The focal surface sagitta s (mm) is given adequately by

$$s = -0.276 + 2.754 \times 10^{-5} r^2 - 4.724 \times 10^{-10} r^4 + 2.870 \times 10^{-16} r^6,$$

where r is the field radius in millimeters. The design is almost distortion-free in the sense that the radius in the focal plane is proportional, to high accuracy, to the field angle (not its sine or tangent); zero distortion for most wide-field imaging is defined for the condition that the radius in the focal plane is proportional to the tangent of that angle, which results in faithful representations of figures on planes, but we wish as faithfully as possible to image figures on a sphere onto a surface that is almost planar. For this case a compromise is necessary between the wishes for constant scale in the sense that meridians have constant linear separation in the focal plane, and the desire that parallels of latitude do likewise. The optimum case depends somewhat on the aspect ratio of the field and is somewhere between the radius in the focal plane going like the sine of the input angle and its tangent. For a square focal plane, which is close to the situation at hand, the radius approximately proportional to the angle itself is the best, and we have made this choice. The errors can be minimized by clocking different chips at different rates to correspond to the local scale along the columns, but we have chosen not to do so for reasons of noise reduction and simplicity in the data system. Our design results for the best compromise tracking rate in worst-case image smearing along the columns of $0'.06$, $3 \mu m$, or 0.14 pixels over the imaging array. Stars do not quite follow straight trajectories in the focal plane, but this can be compensated for by a slight rotation of the outer chips, amounting to about $0'.006$ at the corners. If it is ignored, the resulting error is about 0.24 pixels; both of these are entirely negligible (and are, in fact, of the same order as residual distortions arising from the deviations of the focal height from the desired strictly linear relationship with angle), but the problem quickly becomes severe for bigger fields and can only be properly addressed with anamorphic optics.

The second corrector is very close to the focal plane, and we made use of that in a very fundamental way in the design of the camera: we use this element, which is made of fused silica, as the substrate upon which the camera is built and rely upon it to maintain the exacting mechanical tolerances required for image quality and astrometry. It has a central thickness of 45 mm, and the front face is very strongly aspheric, having an aspheric sagitta of more than 8 mm. The required global accuracy, however, is not terribly stringent since it is placed close to the focal plane. It was figured using mechanical metrology by Loomis Custom Optics to a

set of specifications that basically placed limits on the structure function of the slope of the element to assure negligible image degradation and astrometric error. The rear (plane) face of the corrector is 13 mm above the focal surface at the center, about 10 mm at the extreme edge. The thickness was chosen primarily for mechanical strength and stiffness in view of the mechanical role it plays, with some small detriment to the image quality owing to the longitudinal color that such a thick element introduces. This plane face is the surface to which the dewars that house the CCDs and the kinematic mounts for the optical benches upon which the CCDs are mounted are attached and registered.

The CCDs are mounted in such a way that they can be adjusted to conform to the focal surface. This requires a tilt slightly smaller than 1° at the edge of the field. There is one further complication brought about by the fact that the CCDs as produced are slightly convex, with a reasonably well controlled radius of about 2.2 m. Thus the best-fit plane results in focus errors of about $100\text{ }\mu\text{m}$ rms, which at $f/5$ corresponds to an image degradation of about $20\text{ }\mu\text{m}$. We correct this curvature (to the mean chip radius—corrections for each chip individually results in unacceptable scale variations from device to device) for each chip with weak field deflatteners cemented to the rear face of the filter, which in turn is cemented to the back side of the second corrector surface. The central thickness of the filter/deflatener element is 5 mm for the photometric filters and 6 mm for the astrometric ones, so the vertices of the CCDs are nominally about 8 and 7 mm behind the filters.

The front side of the second corrector is antireflection coated in four strips that match each color band (the same coating was used for i' and z') using appropriate masks in the coating process. The coating was done by QSP Optical Technologies and results in reflectivities below 0.2% in each band. Thus there are only two surfaces near the detectors, and, with the excellent antireflection coatings on the corrector, the primary source of ghosts in this system is the reflection from the CCD surface to the back surface of the filters only about 7 mm away and back. Though the interference coatings of the filters (which are on this back surface) are quite good antireflection coatings in-band, there are inevitable very high reflectivities (accompanied by very low transmission) in the short-pass cutoff region, and at the cutoff wavelength the transmission and reflectance are necessarily of order 50%. It is in these narrow-transition spectral regions that most of the ghost flux originates; the u' and z' do not suffer from this phenomenon because they do not use interference short-pass filters, but the others do. (The filters and their makeup are discussed in more detail in Fukugita et al. 1996.)

The discussion of the optical performance of the camera configuration is a bit complicated because of the complexity of the focal plane, with different filters in different locations and the effect of residual distortion on the final TDI image quality.

To facilitate more detailed discussion of image quality we show the optical layout of the camera focal plane in Figure 1, which shows the locations of the 30 2048×2048 photo-

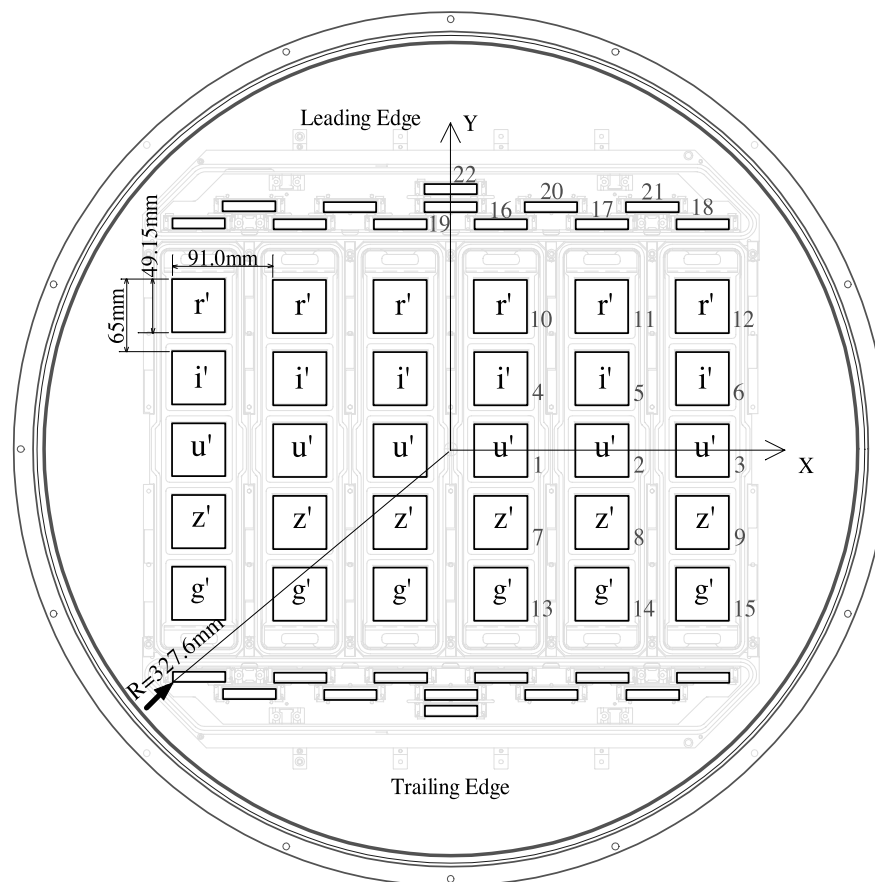


FIG. 1.—Optical layout of the focal plane of the SDSS camera. Field 22 (top and bottom) are focus CCDs; fields 16–21 are astrometric chips, and 1–15 are the photometric array. The TDI scan direction is upward, so a star traverses the array from top to bottom.

metric CCDs, the 22 2048×400 astrometric chips, and the two 2048×400 focus-monitoring sensors. The five filters are arranged in (temporal, leading to trailing) order along the columns: r' , i' , u' , z' , and g' .

The camera is right-left-reflection symmetric and the lower astrometric/focus array is the mirror image of the upper array, so only 22 chips are given identifying field numbers. The direction of the TDI scan is upward in this diagram, so a given star first encounters an upper (leading) astrometric device, then an r' chip, then a i' chip, and so on until, 485 s later, it encounters the trailing astrometric chip located at the bottom in the figure. The arrow points to the extreme field radius used by the camera. This is at the corner of field 18, 327.6 mm, or about $90'6''$ from the center.

To evaluate the image quality, we have performed a polychromatic ray trace and composited several images along a CCD column to simulate the effects of the TDI scan. For each CCD, at each point of the 5×5 array on the device the system has been traced with five wavelengths chosen such that each is the mean wavelength of the corresponding quintile of the filter/system photon response; thus each has equal weight in the final image.

The final images (five per CCD) are composed of the five individual monochromatic images and, because TDI integrates along a column, of a composite of the five images along a CCD column, taking account in the first instance of any lateral color shifts and in the second of any residual

distortion perpendicular to the column and residual distortion and scale error along the column. The images are defocused to lie in the best-fitting focal surface with the mean curvature of the CCDs for each subfield (tilt and piston are fitted). The input angles along the column accurately represent images at successive equally spaced time intervals in TDI mode, and the geometry on the sky for TDI is accurately modeled. The final images are shown in Figure 2. There are two panels: the bottom panel shows the images as delivered by the design optical system, and the top as convolved with $0''.8$ (FWHM) Gaussian seeing. The point-spread functions (PSFs) were generated by fitting discrete Zernike polynomials to the slope errors in the system and using those fits to generate intercepts in the desired focal plane for 1200 rays for each of the 25 images that go into the polychromatic TDI composite. Those rays were binned in $0''.05$ pixels to generate the intensities for the gray-scale images. In each panel, each row of images is the model of TDI output for the array as labeled in Figure 1; thus the bottom row consists of five images each across fields 13, 14, and 15, the next 7, 8, and 9, and so forth. The top two rows are the astrometric fields 16, 17, 18 and 19, 20, 21. The images for the focus array are discussed and shown later in § 5. The spacing between successive closely spaced images in the mosaic is $3''$.

The situation is summarized quantitatively in Table 1, where each row lists the properties of one detector field. The

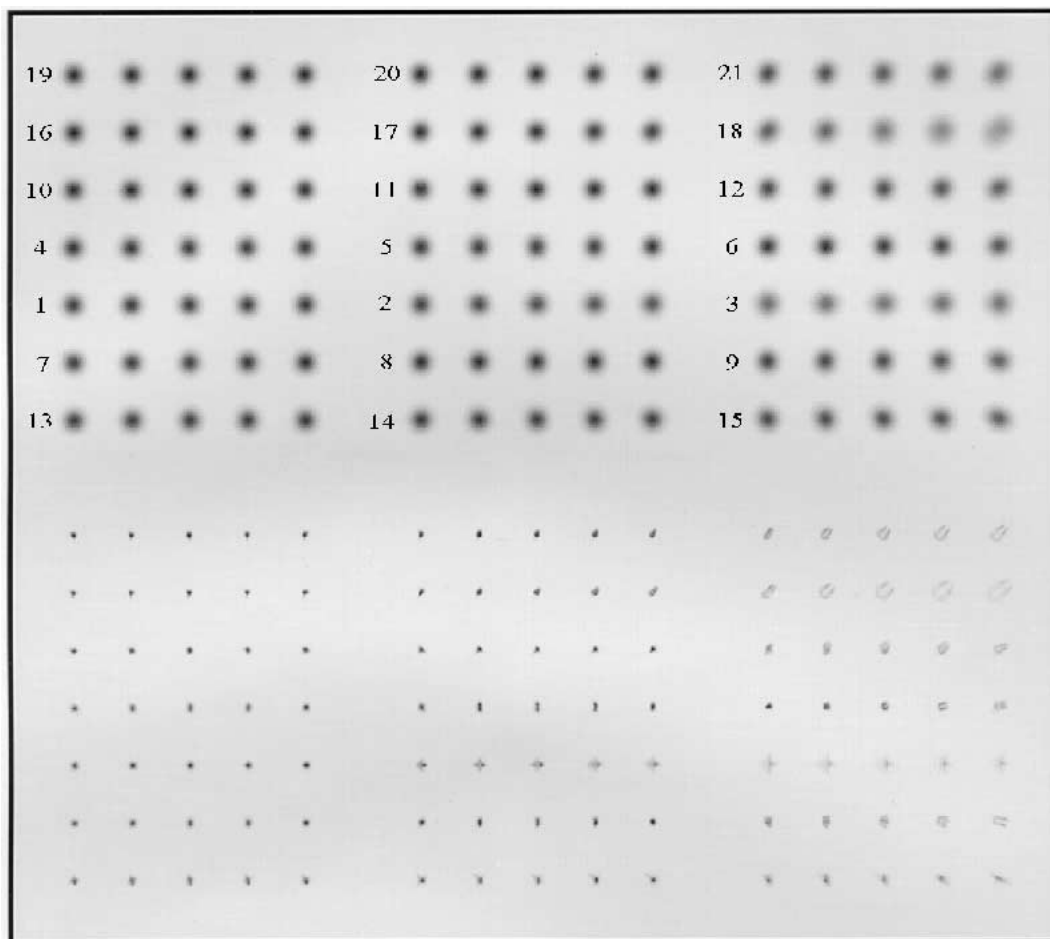


FIG. 2.—Gray-scale images of the PSF in the distinct optical fields identified in Fig. 1. The bottom panel shows the output of the optical design with no seeing; the top images are those convolved with $0''.8$ FWHM Gaussian seeing. The five images for each field are for five positions horizontally across the chip, evenly spaced from one extreme edge to the other.

TABLE 1
SUMMARY OF TDI IMAGES WITH SCAN SCALE $3.6343 \text{ mm arcmin}^{-1}$

Field	x (mm)	y (mm)	CCD size (mm \times mm)	Filter	ffc3 (mm $^{-1}$)	ccd4 (mm $^{-1}$)	vscale (mm arcmin $^{-1}$)	dfoc (μm)	dc4 (mm $^{-1}$)	em (μm)	eM (μm)
1	45.5	0.0	49.2×49.2	u'	$1.37\text{E}-3$	$4.3\text{E}-4$	-3.6317	5	$0.3\text{E}-4$	17	35
2	136.5	0.0	49.2×49.2	u'	$1.37\text{E}-3$	$4.3\text{E}-4$	-3.6332	8	$-0.3\text{E}-4$	19	25
3	227.5	0.0	49.2×49.2	u'	$1.37\text{E}-3$	$4.3\text{E}-4$	-3.6335	28	$-1.3\text{E}-4$	30	38
4	45.5	65.0	49.2×49.2	i'	$1.40\text{E}-3$	$4.3\text{E}-4$	-3.6350	4	$0.2\text{E}-4$	18	21
5	136.5	65.0	49.2×49.2	i'	$1.40\text{E}-3$	$4.3\text{E}-4$	-3.6353	13	$-0.4\text{E}-4$	20	24
6	227.5	65.0	49.2×49.2	i'	$1.40\text{E}-3$	$4.3\text{E}-4$	-3.6339	30	$-1.3\text{E}-4$	25	35
7	45.5	-65.0	49.2×49.2	z'	$1.40\text{E}-3$	$4.3\text{E}-4$	-3.6348	4	$0.1\text{E}-4$	18	21
8	136.5	-65.0	49.2×49.2	z'	$1.40\text{E}-3$	$4.3\text{E}-4$	-3.6350	13	$-0.5\text{E}-4$	20	25
9	227.5	-65.0	49.2×49.2	z'	$1.50\text{E}-3$	$4.3\text{E}-4$	-3.6347	26	$-1.1\text{E}-4$	28	39
10	45.5	130.0	49.2×49.2	r'	$1.30\text{E}-3$	$4.3\text{E}-4$	-3.6342	12	$-0.5\text{E}-4$	18	19
11	136.5	130.0	49.2×49.2	r'	$1.30\text{E}-3$	$4.3\text{E}-4$	-3.6338	25	$-1.0\text{E}-4$	20	23
12	227.5	130.0	49.2×49.2	r'	$1.50\text{E}-3$	$4.3\text{E}-4$	-3.6347	37	$-1.4\text{E}-4$	26	32
13	45.5	-130.0	49.2×49.2	g'	$1.30\text{E}-3$	$4.3\text{E}-4$	-3.6350	10	$-0.4\text{E}-4$	19	22
14	136.5	-130.0	49.2×49.2	g'	$1.30\text{E}-3$	$4.3\text{E}-4$	-3.6347	23	$-0.9\text{E}-4$	21	23
15	227.5	-130.0	49.2×49.2	g'	$1.40\text{E}-3$	$4.3\text{E}-4$	-3.6350	39	$-1.5\text{E}-4$	27	31
16	45.5	204.5	49.2×9.6	r'	$1.50\text{E}-3$	$4.3\text{E}-4$	-3.6354	2	$-0.1\text{E}-4$	19	21
17	136.5	204.5	49.2×9.6	r'	$1.50\text{E}-3$	$4.3\text{E}-4$	-3.6350	10	$-0.8\text{E}-4$	22	26
18	227.5	204.5	49.2×9.6	r'	$1.80\text{E}-3$	$4.3\text{E}-4$	-3.6362	20	$-1.4\text{E}-4$	30	40
19	0.0	220.0	49.2×9.6	r'	$1.50\text{E}-3$	$4.3\text{E}-4$	-3.6353	1	$-0.0\text{E}-4$	20	21
20	91.0	220.0	49.2×9.6	r'	$1.50\text{E}-3$	$4.3\text{E}-4$	-3.6352	6	$-0.4\text{E}-4$	21	24
21	182.0	220.0	49.2×9.6	r'	$1.60\text{E}-3$	$4.3\text{E}-4$	-3.6355	17	$-1.2\text{E}-4$	26	33
22	0.0	235.5	49.2×9.6	r'	$1.50\text{E}-3$	$4.3\text{E}-4$	-3.6353	2	$-0.2\text{E}-4$	22	23

table lists the field center in millimeters measured from the optical axis ($-y$ is the TDI scan direction), the size of the CCD for that field, the filter, the field-flattener curvature in units of 10^{-3} mm^{-1} ("ffc3"), the CCD curvature in units of 10^{-4} mm^{-1} ("ccd4"), the vertical (along the CCD columns, the scanning direction) scale in that field ("vscale" in mm arcmin $^{-1}$), the rms focus error in microns over the CCD caused by mismatch between the final best focal surface and the curved CCD surface ("dfoc"), the residual field curvature in units of 10^{-4} mm^{-1} ("dc4"), and the minimum ("em") and maximum ("eM") rms image diameters over the field in microns. We should perhaps comment on the residual curvature; the overall scale in the focal surface is $3.615 \text{ mm (arcmin)}^{-1}$, for the optical design, but the field deflaters change the scale locally for each chip to a number close to 3.643, which is the "scan scale," i.e., the assumed tracking rate. Changes in this scale from chip to chip, and color to color, represent errors in the TDI images, and the field-flattener curvatures are chosen for the best compromise between keeping the scale constant and matching the focal curvature. The as-manufactured optics give a scale very nearly the design value but uncertain by about a unit in the third place; in practice, the scale will be determined by tests on the sky. Scale errors are in general much more serious for image quality than focal errors, so there is usually some residual curvature.

The results indicate that for the photometric array, the maximum rms image diameters are for the UV fields, reaching $0''.63$ for the outermost one. The difficulty of achieving good images in the u' band (owing to the loss of proper aberration correction by the correctors with the large index shift at u') is the reason we have placed the u' row in the center. The increase from $27 \mu\text{m}$, the average diameter of monochromatic non-TDI images in the u' field 3, to $38 \mu\text{m}$ in the full TDI polychromatic treatment is mostly due to longitudinal color, with tiny contributions from defocus and lateral color and substantial ones from TDI effects. Images as large are seen at the field extremes at the other end of the spectrum in z' , where they reach $39 \mu\text{m}$, $0''.65$ rms.

(Recall that for Gaussian images, the FWHM is 0.83 times the rms diameter; these aberrated images are not by any means Gaussian, but if the seeing dominates the image size, the resulting convolution does not change the form of the PSF very much, and for image degradation considerations these worst images can be considered equivalent to Gaussians with FWHMs of $0''.53$ for the u' and $0''.54$ for the z' one.) The other images are of order $0''.5$ or better (rms) over the whole field. The problems in z' are also due to the extreme wavelength; the optimization of the system involves balancing the color effects at the wavelength extremes, and because the polychromatic effects at u' are so large the monochromatic optimization is biased toward the UV. The optimization of the system was done in a very detailed way, taking account of the filter/detector combination at a given location in the focal plane. There is, of course, further image degradation caused by differential atmospheric refraction, which is fairly serious in u' and g' , particularly near the northern and southern survey limits at about 1.8 air masses.

The images for the astrometric chips are almost as good as those over the photometric array except for the outer half of field 18, the outermost of the first rank of CCDs, where the images again reach two-thirds of $1''$ in rms diameter.

The images for the focus chips (field 22) are still quite good, about $0''.38$ rms diameter, and with almost no variation over the field of the focus devices, so even though the focus sensors are near the outer edge of the field, the sensitivity of the focus servo is still essentially determined by seeing.

3. CCDs AND PHOTOMETRIC SYSTEM

3.1. CCDs

The whole SDSS project hinged on the availability of many (42, including spares) 2048×2048 CCD sensors, for this camera, for a small photometric monitor telescope, and for a pair of two-channel fiber spectrographs. At least eight of these need excellent UV sensitivity and very low readout noise ($< 5 e^-$). At the inception of the work more than seven

years ago, it was by no means obvious that the chips could be obtained. The Tektronix 2048D, the $24\text{ }\mu\text{m}$ pixel 2048×2048 device around which we were designing the optics (because it was a good match to a reasonable-sized telescope with a reasonable focal ratio and was the only commercial possibility at that time) was supposedly a commercial item, but in fact was in very short supply, and without the very large order for the devices from this project might well have been discontinued. Anxious moments continued to occur for a long time after the order was placed and accepted, but the situation improved markedly in the intervening years, and the requisite number of chips arrived, worked, and are now operating in the camera. We cannot thank the crew at Tektronix/SITe enough for their patient persistence and unflinching cooperation in this effort.

Our cosmetic requirements were not as severe as those of many of the customers of Tek/SITe, since TDI gets rid of a whole suite of defects that would mar performance in normal imaging mode, and we have procured chips with special grading qualitatively different from and in general somewhat lower than that used for their normal grade 1 devices.

Our requirements differ quite widely from filter to filter, since in z' and i' the expected sky levels are over $1000\text{ }e^-$, but in u' they are only about $40\text{ }e^-$, so quite noisy devices can be tolerated in some places and very quiet ones are needed in others. We began by setting up a complex set of requirements, but in the end took the results of the best efforts of SITe, which turned out to be quite satisfactory. The chips are also not all alike—we decided on economic grounds to use front-side-illuminated devices for the z' band, at what we believed at the time to be a price of about a factor of 2 in quantum efficiency (QE). This was fortuitously an exceedingly fortunate choice that we have not regretted at all because of a later-discovered internal scattering phenomenon exhibited by thinned devices in the infrared that would have made data reduction with thin chips working as far into the infrared as z' very difficult. (We discuss this matter further below; it is not a serious problem for our other bands, where we do use thinned chips). For the detectors for g' , r' , and i' , we use the standard visible anti-reflection coated (VIS/AR) thinned back-side-illuminated devices. It also appeared at the time that special coatings for the u' were desirable to enhance the QE in the UV; the wisdom of this choice is now not so clear. The characteristics of the CCDs in the camera are summarized in Table 2. The mean QEs are measured in $100\text{ }\text{\AA}$ wide bands at the indicated wavelengths and have a very small dispersion for all chips except the u' ones, where it is about 10% of its typical value. The room temperature QE at $3500\text{ }\text{\AA}$ is between 40% and 50% with our UV coating, but we have found that this high QE in UV declines at low operating temperatures and is between 35% and 40% for all our

devices at -80°C . The gain over the standard VIS/AR devices is not very large, though the steep falloff of their QE to the UV would significantly lengthen the effective wavelength of the u' band. The expected sky fluxes are for the mean sky brightness at the site at 1.4 air masses, scanning at sidereal rate. The QEs for thinned CCDs with the normal and the UV-enhanced antireflection coating, as well as unthinned devices, are shown in Figure 3.

The cosmetics and charge-transfer characteristics of the devices are in general very good. As part of the testing, the charge transfer efficiency (CTE) was measured at a level of $200\text{ }e^-$. It is typically better than 0.99999 both horizontally (serial) and vertically (parallel). We measure CTEs of around 0.99998 horizontally and 0.99994 vertically at illumination levels of $30\text{ }e^-$. At the lower level, which is somewhat less than the UV sky level, the net transfer efficiency is 86% from the upper center of the chip, and 92% for the mean pixel in the TDI scan. The effect on the PSF is essentially to increase its rms height by convolving it with an exponential with an exponentiation length of about 0.4 pixels. The seeing typically has a Gaussian core with a σ of about 1 pixel, so the core is widened by about 8% for objects at sky level and less for brighter ones; for objects at the detection limit, the central pixel is about twice as bright as the sky in u' , and the effect is roughly halved. For PSF-fitting photometry, which we will use, the photometric error is approximately one-half the width error for each dimension, so the error induced is about 0.04 mag at the sky, and about 0.02 mag at the detection limit in u' (faint objects are biased slightly bright). There is also a shift, of course; this is of order of 0.02 pixels horizontally and 0.07 pixels vertically (8 and 28 mas, respectively) after averaging over the column as TDI does. Again, these errors are much reduced for detectable objects.

For the higher background chips the astrometric shifts are 0.007 pixels horizontally and 0.02 pixels vertically, and the photometric errors are completely negligible. The overall cosmetic uniformity is excellent as well, with rms large-scale QE variations of about 7% in the blue and 4% in the red and infrared. The main defects we have seen are parallel traps of various strengths, many of which are strong

TABLE 2
CCD NOISE AND QUANTUM EFFICIENCY

Filter	Max Noise (e^-)	$\langle\text{QE}\rangle$	λ (\AA)	e^- in Sky
u'	7	0.36	3500	45
g'	7	0.73	4700	400
r'	9	0.82	6400	700
i'	20	0.69	7700	1200
z'	16	0.18	9200	1100

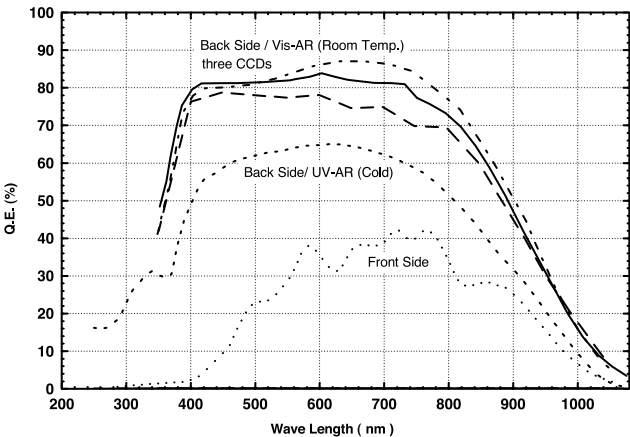


FIG. 3.—Quantum efficiencies of the three varieties of CCDs used in the camera, showing for the thinned VIS/AR coated chips a representative range of variability encountered among different devices of the same type. Note that the VIS/AR curves are for room temperature, the others cold. At operating temperature the infrared response of the VIS/AR devices is comparable to the others. On the scale of this figure it is not possible to see easily the extended infrared response of the front-side devices.

enough to cause serious CTE degradation in the vertical direction with the backgrounds we are using, though, as we discuss below, they are not fatal if they involve only isolated columns. A subimage in the corner farthest from the amplifier for a typical device operated with only one amplifier of a Ronchi target with $30\ e^-$ signal in the bright bars is shown in Figure 4, in which the excellent cosmetic appearance and low-level CTE are seen.

The full well is in the neighborhood of $300,000\ e^-$, except for the u' devices, where the parallel gates have to be run at lower potentials in order to avoid shot noise from spurious charge generation; we measure about 200,000 for them. The signals in u' are so much lower than in the other bands even for very blue objects that this is not a problem.

We specified in our selection criteria that no device can have adjacent bad columns; this is driven by the fact that we are well enough sampled that we can interpolate effectively over a single bad column using linear predictive coding techniques, but we cannot over two or more. The number of single bad columns varies a great deal from device to device and goes from none to about 30 for the worst z' chip. The front-side z' devices were produced early in the program and have the worst cosmetics, but fortunately the signal levels are very high in this band.

These chips can in principle operate in multipinned phase mode, but we cannot use it effectively in the scanning array, since it is clocking all the time. They are driven by three-

phase clock signals generated from high-stability DC rails with CMOS switches, and all the chips are clocked synchronously. The typical output gain of the on-chip FET is $1\ \mu\text{V}$ per electron, and the dynamical range is 30,000:1 with full well of $300,000\ e^-$. Dark current at 20°C is typically less than $200\ \text{pA cm}^{-2}$ for the front-illuminated and back-illuminated VIS/AR devices and somewhat higher for the UV devices; in no case does the dark current produce appreciable signal or shot noise at -80°C .

The devices are designed and bonded out so that the four quadrants can be read independently, which for many applications results in a factor of 4 improvement in readout time; for us, it is the split in the serial direction that is useful, since we must integrate over the full chip vertically. The requirement of reading out the whole device in 54 s for sidereal rate scans results in a pixel time of about $24\ \mu\text{s}$ with the split serials. Unfortunately, this does not work for all chips in hand: acquiring enough devices demanded that we accept a few (six) that have only one good on-chip amplifier. For these, we must clock the serial register twice as fast, which incurs a noise penalty of about a factor of 1.3, so the one good amplifier has to be better. We generate two synchronized serial clocking streams to service the one- and two-amplifier devices, one synchronized to but exactly twice as fast as the other.

The devices, first characterized roughly at SITE, were evaluated with a cold-test station at Princeton having elec-

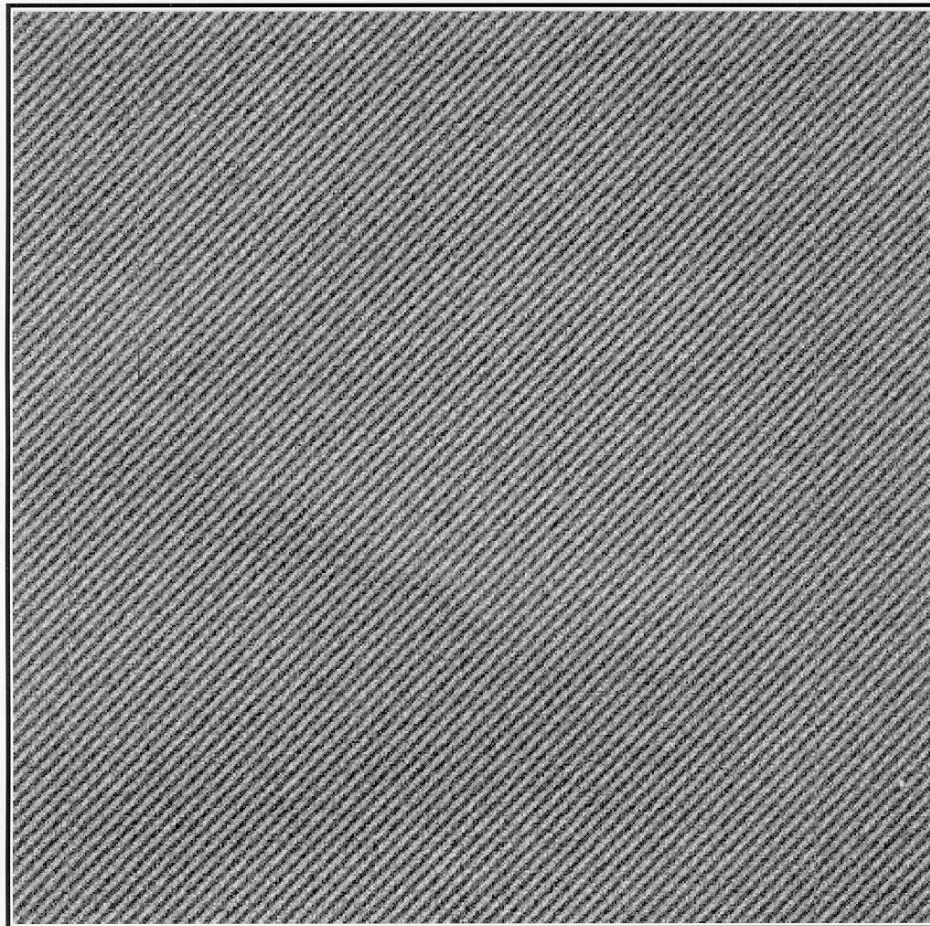


FIG. 4.—Image of a Ronchi ruling at a peak exposure level of $30\ e^-$. The period of the ruling is about 6 pixels, and the image is taken from a single-amplifier frame from the corner farthest from the amplifier. Defects associated with a small number of vertical traps can be seen in the image; the most prominent one and its associated head are slightly above the center near the left edge of the image.

tronics similar to the survey electronics. The system noise is about 1 electron, and we have the capability to measure CTE and QE as a function of wavelength, uniformity, and also to test the vertical CTE in TDI mode using a special parallel-bar target and a flash lamp. The technique involves running the chip for some time with a uniform “sky” background of appropriate level and then exposing the bar target, which consists of about 200 thin bright lines parallel to the rows of the CCD, with a flash lamp to impose a low-level signal. This frame of data is then captured as the chip continues to scan in TDI mode, and the bars are superposed to simulate a single such bar traveling along the chip following the charge packets. This test is important, because some very low-level parallel traps that show up in single frames are satiated by the sky in TDI mode and disappear; other stronger traps permanently damage the CTE in the affected columns.

We verified an effect first reported by R. Reed (1995, private communication), which has a drastic effect on the spatial resolution of thinned chips in the far red; there appears to be a halo of the form $B \propto S \exp(-r/r_0)r^{-1}$, where S is the point-source total signal, with a characteristic radius r_0 that is a strongly increasing function of wavelength; we found that $r_0 \simeq 50\lambda^2$, with λ in microns and r_0 in pixels, for these devices. The fraction of light f in the halo is reasonably well represented by the exponential relation $f = \exp[11.51(\lambda - 1.05)]$, essentially unity for $\lambda > 1.05 \mu\text{m}$. The fraction of light in the halo is about 0.9%, 5%, and 30% in the r' , i' , and z' bands, respectively. The phenomenon is apparently caused by the trapping of transmitted radiation between the metallic solder surface used to attach the translucent substrate of the thinned die to the package and the silicon substrate. The surface brightness in this scattering halo is roughly the same order as that from the atmospheric/optical scattering wings for a small range of radii in i' and slightly complicates the algorithms we use to subtract bright stars, but is otherwise not serious. Its effect is negligible in the shorter bands. If we had used thin chips for z' we would have been in serious trouble and would, in fact, have been no better off purely from a signal-to-noise point of view than we are with the supposedly less sensitive thick devices. The signal from small sources like stars is not very much greater in the thin chips than in the thick ones with one-half the QE because much of it is scattered into the sky, but the sky gets the full QE increase; the result is that the S/N is essentially the same for faint sources with thick devices as with thin, but the thick chips do not have the halos.

We elected to take chips mounted in their standard Kovar header packages even though this led to significant mechanical difficulty in their mounting and cooling; demanding better packaging would have precluded culling our devices from a commercial production stream and would have prohibitively increased the cost and probably made the endeavor economically impossible. The problems incurred are fairly serious, however. The expansion coefficient of Kovar matches silicon (and the substrate for the thinned devices, which does match silicon well) so poorly that the overall curvature of the devices, already serious at room temperature because of problems in high-temperature processing, is much worse at operating temperature. As mentioned above, the chips are convex toward the incoming light by about $230 \mu\text{m}$ center to corner, and that value roughly doubles in cooling to -80°C . We have dealt with

this problem by cementing a heavy Kovar stiffener, which is part of the CCD ball-and-socket mounting discussed below, to the back. It was also necessary to build a precision measuring microscope to aid in the gluing of the photometric chips to this mount, since we wished to position the chips to subpixel accuracy and the chips are not mounted very accurately in their headers. We thus used reference points on the die itself to reference the CCD to its mounting system and succeeded in doing so to an accuracy of about $3 \mu\text{m}$ rms.

The front-side (thick) 2048×400 astrometric/focus CCDs were also produced by SITE for us in two foundry runs. Except for the decrease in parallel gate capacitance due to the decrease in the number of rows, the devices are electrically identical to the photometric CCDs. These chips have been mounted on precisely machined Invar 36 headers of our design that allow them to be mounted quite close together in the column (short) direction, as shown in Figure 1; the minimum distance is, in fact, determined by the filters, which must be oversized to allow for the $f/5$ beam. The headers are machined with a slight convex curvature to match the photometric chips in the long direction; the chips are flexible enough that they bend to this curvature easily and are mounted to the headers with a thin thermally setting epoxy film. The electrical signals to and from the chips are carried by a Kapton flexible printed circuit (FPC) on each end with very thin and narrow copper conductors. These FPCs are mounted permanently on the CCD headers, and the chips are bonded out to pads on them.

3.2. The Photometric System

Our photometric system comprises five color bands (u' , g' , r' , i' , and z') that divide the entire range from the atmospheric UV cutoff at 3000 \AA to the sensitivity limit of silicon CCDs at 11000 \AA into five essentially nonoverlapping passbands. The system was described in detail in Fukugita et al. (1996) for the SDSS photometric monitor telescope, which is identical to the system for the main camera except for the fact that the monitor has a single UV-coated CCD for all bands and slightly different mirror coatings. We review the system here and describe in detail only those features that are unique to the camera or are associated with the camera sensitivity.

The filters have the following properties: u' peaks at 3500 \AA with a FWHM of 600 \AA , g' is a blue-green band centered at 4800 \AA with a width of 1400 \AA , r' is the red passband centered at 6250 \AA with a width 1400 \AA , i' is a far-red filter centered at 7700 \AA with a width of 1500 \AA , and z' is a near-infrared passband centered at 9100 \AA with a width of 1200 \AA ; the shape of the z' response function at long wavelengths is determined by the CCD sensitivity.

While the names of these bands are similar to those of the Thuan & Gunn (TG) photometric system (Thuan & Gunn 1976; Schneider, Gunn, & Hoessel 1983), the SDSS system is substantially different from the Thuan-Gunn bands. The most salient feature of the SDSS photometric system is the very wide bandpasses used, even significantly wider than that of the standard Johnson-Morgan-Cousins system. These filters ensure high efficiency for faint object detection and essentially cover the entire accessible optical wavelength range.

The filter responses are in general determined by a sharp-cutoff long-pass glass filter onto which is coated a shortpass interference film and thus exhibit wide plateaus terminated with fairly sharp edges. The exceptions are the u' filter (the

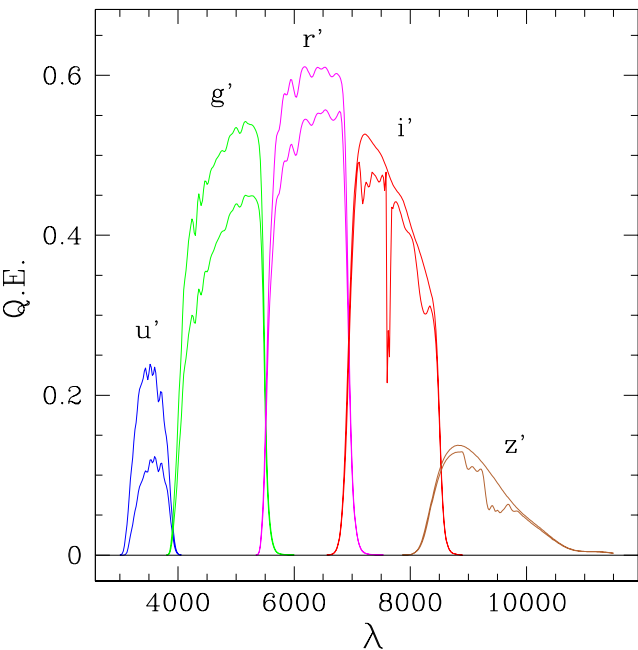


FIG. 5.—System QE for each filter/detector system in the photometric array. The expected throughput of the optics is included; the lower of each pair of curves includes the expected atmospheric extinction associated with 1.2 air masses at our site.

passband is defined by the glass on both sides, and it is much narrower than the others) and the z' filter (no long-wavelength cutoff). The division of the passbands is designed to exclude the strongest night-sky lines of O I $\lambda 5577$ and Hg I $\lambda 5460$. The u' -band response is similar to TG u and Strömgren u in that the bulk of the response is shortward of the Balmer discontinuity; this produces a much higher sensitivity (combining with g') to the magnitude of the Balmer jump at the cost of lower total throughput. Proper consideration of photon noise indicates that this is to be preferred to a wider band with dilution by redder light. The makeup of the filters is detailed in Fukugita et al. (1996); the interference coatings were done by Asahi Spectral Optics, Ltd., Tokyo.

The photometric filters are 57 mm² and are all brought to 5 mm thickness by adding a neutral glass element (BK7 or quartz), so that all filters have approximately the same optical thickness; this is necessary to keep the scale variations on the CCDs small. The neutral glass element (GG 400 for g') is a plano-concave lens with a radius of curvature of 670–770 mm, serving as a field flattener as discussed above. These filters are cemented to the back side of the second corrector.

The system response functions, S_ν are shown in Figure 5. The response curves include the filter transmission, the QE for CCD, flux loss due to the correctors, and the reflectivities of the two aluminum surfaces. Figure 5 also presents

TABLE 3
SDSS FILTER CHARACTERISTICS AND PHOTOMETRIC SENSITIVITY, 1.4 AIR MASSES

Filter	λ_{eff}	FWHM	q_t	Q
u'	3549	560	0.111	0.0116
g'	4774	1377	0.436	0.113
r'	6231	1371	0.549	0.114
i'	7615	1510	0.490	0.0824
z'	9132	940	0.128	0.0182

the response curves including atmospheric extinction at 1.4 air masses, based on the standard Palomar monochromatic extinction tables scaled to the altitude of the Apache Point Observatory (2800 m). The characteristics of the passbands (with 1.4 air masses) are tabulated in Table 3.

The response functions differ slightly from chip to chip. We define the SDSS photometric system by the response function of the SDSS “Monitor Telescope,” a 60 cm reflector located at the same site. The telescope is equipped with a thinned, back-illuminated, UV-antireflection-coated CCD, the same as those used for u' imaging of the photometric array. We will apply a color transformation to the instrumental magnitude obtained with the photometric array, converting it into the system defined by the Monitor Telescope detector. These corrections are small (of order 0.02 mag) except in the z' band, which is significantly redder and broader in the camera than in the monitor system owing to more extended infrared response in the thick devices and the steep wavelength dependence of the scattering, which effectively depresses the QE for stars, in the thin chips.

In Table 3, the quantity q_t is the peak system QE in the system, and $Q = \int (\ln \nu) S_\nu \approx q_t \Delta\lambda/\lambda$ is the system efficiency, which relates the monochromatic flux averaged over the filter passband to the resulting signal expressed in terms of the number of photoelectrons:

$$N_{\text{el}} = 1.96 \times 10^{11} t Q 10^{-0.4 \text{AB}_\nu}, \tag{2}$$

where t is exposure time in seconds; a 27% obscuration of incoming flux by the secondary mirror and the light baffles are taken into account. AB_ν is AB magnitude at frequency ν , corrected for atmospheric extinction.

Table 4 gives the expected sky background counts and expected saturation levels for the camera, assuming a zenith sky V brightness of 21.7 mag arcsec^{−2} and a Palomar sky spectrum (Turnrose 1974) modified to remove the strong mercury and sodium lines from Los Angeles and San Diego. Saturation corresponds to an assumed full well of $3 \times 10^5 e^-$. The effective sky brightness in the tables is corrected for atmospheric extinction so that it is treated properly along with the flux from the star.

The counts and S/Ns for stellar objects with a double Gaussian PSF with $\sigma = 0''.38$ and $1''.09$ with the same sky

TABLE 4
PHOTOMETRIC SATURATION AND SKY BACKGROUND

Parameter	u'	g'	r'	i'	z'
Star saturates at AB	12.0	14.1	14.1	13.8	12.3
Effective sky (mag arcsec ^{−2})	22.1	21.8	21.2	20.3	18.6
Sky + background (counts pixel ^{−1})	40	390	670	1110	1090

TABLE 5
PHOTOMETRIC SENSITIVITY FOR $V_{\text{sky}} = 21.7$ AND $\sec z = 1.4$

AB	u'		g'		r'		i'		z'	
	Counts	S/N	Counts	S/N	Counts	S/N	Counts	S/N	Counts	S/N
17.0.....	28033	160.4	194863	428.2	194863	420.2	140849	338.2	31281	124.2
17.5.....	17688	124.5	122950	334.4	122950	325.0	88869	255.0	19737	86.7
18.0.....	11160	95.5	77577	258.8	77577	248.1	56073	188.3	12453	59.0
18.5.....	7042	72.1	48947	197.9	48947	186.1	35380	135.7	7857	39.3
19.0.....	4443	53.3	30884	148.7	30884	136.6	22323	95.2	4958	25.7
19.5.....	2803	38.5	19486	109.4	19486	97.8	14085	65.2	3128	16.7
20.0.....	1769	27.1	12295	78.5	12295	68.2	8887	43.6	1974	10.7
20.5.....	1116	18.6	7758	54.8	7758	46.4	5607	28.7	1245	6.8
21.0.....	704	12.4	4895	37.4	4895	30.9	3538	18.6	786	4.3
21.5.....	444	8.2	3088	24.9	3088	20.2	2232	12.0	496	2.7
22.0.....	280	5.3	1949	16.4	1949	13.1	1408	7.6	313	1.7
22.5.....	177	3.4	1230	10.6	1230	8.4	889	4.9	197	1.1
23.0.....	112	2.2	776	6.8	776	5.4	561	3.1	125	0.7
23.5.....	70	1.4	489	4.3	489	3.4	354	1.9	79	0.4
24.0.....	44	0.9	309	2.8	309	2.2	223	1.2	50	0.3
24.5.....	28	0.6	195	1.7	195	1.4	141	0.8	31	0.2
25.0.....	18	0.4	123	1.1	123	0.9	89	0.5	20	0.1

are given in Table 5. The noise is assumed to be given by

$$N_{\text{el}}(\text{noise}) = (N_{\text{el}} + n_{\text{eff}} f_{\text{sky}} + n_{\text{eff}} \text{RN}^2)^{1/2} \quad (3)$$

for a noise-effective image size of n_{eff} pixels. The exposure time is taken to be 54 s, and the read noise RN is taken to be $7 e^-$. The dark current is negligible.

The limiting magnitude for detection, set at $S/N = 5$, will be approximately $u' = 22.1$ mag, $g' = 23.2$ mag, $r' = 23.1$ mag, $i' = 22.5$ mag, and $z' = 20.8$ mag for stars. An S/N of 50:1 (and hence photometry at the 2% level) is reached at 19.1, 20.6, 20.4, 19.8, and 18.3 mag in the five bands. Typical galaxy images reach a given S/N of half a magnitude to a magnitude brighter at the faint end, depending on their surface brightness.

4. MECHANICAL DESIGN OF THE PHOTOMETRIC ARRAY

The CCDs for the photometric array are housed in six long thin dewars (Figs. 6 and 7) machined from aluminum blocks, each containing five chips in one column. The CCDs are kept cooled at -80°C during operation by an autofill liquid-nitrogen system that will be described in the next section. The optical system is so fast and the focal plane so large that mounting the chips and maintaining dimensional stability is potentially a difficult problem. We require astrometry at the 30 mas per coordinate level, which corresponds to $2 \mu\text{m}$ in a focal plane 650 mm in diameter. We have solved this problem in a rather unusual but, we think, very satisfactory manner. The final corrector in the optical system is a quite thick piece of fused quartz with a flat rear face, 45 mm thick in the center and some 8 mm thicker at its thickest point; we use this element as the mechanical substrate to which all the CCDs are registered and all the dewars attached. The corrector thus serves as both a mounting substrate and a window for the camera dewars. Quartz is strong, reasonably stiff, and has excellent dimensional stability and very small thermal expansion coefficient. The small mechanical deflections ($\approx 1 \mu\text{m}$) associated with loading it with the camera have completely negligible impact on its optical performance. Figure 8 shows the front view of the whole assembly through the final corrector as it would look with the shutters removed. Figure 9 shows the assembled corrector plate, mounted in its support, with the dewar mounting rails.

The CCDs in the column are mounted 65 mm center to center, which leaves 1.5 mm gaps between the 63.5 mm square Kovar packages in which the devices are mounted. There is a somewhat larger gap between the edges of the packages and the side walls of the dewars. It is important to mount the CCDs in the camera so that each of them is adjustable for rotation, tilt, and piston to high precision, and that this precision is stably maintained for the whole period of the survey once they are fixed.

The CCDs are individually cemented to the inner cone element of a mount that has double cone structure. The outer cone, made of Invar 36, acts as a socket. It has machined into its base a precise 45° cone that engages a spherical surface on the inner cone. This piece, made of Kovar, is movable within the socket and works like a ball floating in the outer socket within a restricted angle range, with the center of curvature at the surface of the chip (Fig. 10; see also Figs. 11 and 12). The surface of the ball is mostly cut away, so that three small segments of the sphere 120° apart engage the conical socket. This ensures that the inner ball part sits stably in the outer part even if the conical socket is somewhat distorted. These ball-and-socket mounts provide tilt adjustment via a set of four push-push screws diagonal to the chip direction close to the edge of the cone on each socket (see the leftmost cone in Fig. 12 where screws are seen). These assemblies are in turn mounted on a “T”-shaped Super Invar optical bench (the “Tbar”) in a manner that allows small independent rotation of the chips and shimming for piston. The Tbars are stiff laterally, reasonably stiff vertically, but quite limber in torsion. The load of their own mass and that of the CCDs with their double cone mounts amount to about 2.7 kg. Under the full gravitational load the worst-case deflections are $2 \mu\text{m}$ in the focus direction and $1 \mu\text{m}$ in the image plane when moving from the horizon to the zenith, somewhat less over the operating range of the survey (above 35° elevation).

Two important desiderata for the mounting of the Tbar on the quartz corrector are thermal isolation and mechanical stability against deflection. These requirements are fulfilled by mounting the optical benches, one per CCD column, by a ball-and-rod kinematic mount, which consists of a quartz column bonded and screwed to the corrector, and a set of four ball-and-double-rod pads (Figs. 11 and 13

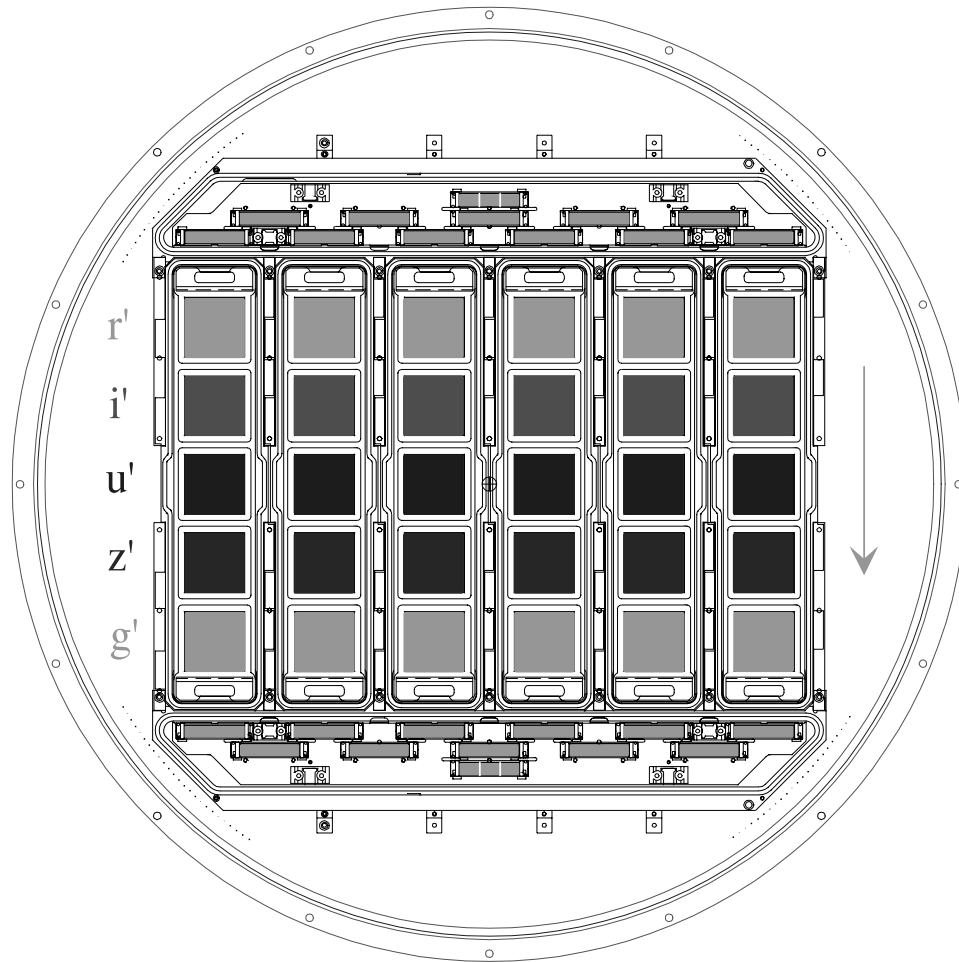


FIG. 6.—Layout of the six photometric and eight astrometric dewars in the camera. The photometric dewars interlock with each other on the mounting rails (see Fig. 8), and the astrometric dewars interlock with the ends of the photometric ones. Note the three filters associated with each focus device.

for an enlarged view), one assembly at each corner of the Tbar. On one end of the Tbar, the arrangement consists of two balls on sets of parallel ways, one parallel to the long axis of the bench and the other perpendicular, which locates that end in both dimensions to within small rotations (Fig. 13). On the other end, one ball rests in a set of parallel ways parallel to the bench, which with the set at the other end fixes the rotation but is free to move along the bench. The ball rests in sets of mutually perpendicular ways, which is completely free to slide in the plane. With this structure the effect of different thermal expansions of quartz and Invar are buffered, and, more importantly, manufacturing variations do not affect the kinematic nature of the mount.

The bench is sufficiently flexible in torsion that the four vertical constraints can be mated independently with quite reasonable dimensional tolerances and forces (50 N) on the balls and, in fact, needs the four-point support for torsional stability. The $\frac{1}{4}$ inch balls are made of titanium, which is tough, and combines reasonably good Young's modulus and reasonably low thermal conductivity. The $\frac{3}{32}$ inch rods are of hard 302 stainless steel. The conductive losses for each ball joint are about 0.5 W, with the 100°C temperature drop shared roughly equally between the ball joint and the quartz column. The heat flux across the mount can be calculated to be $(\Delta T \times \text{conductivity})/(\text{force} \times \text{radius}/\text{elastic modulus})^{1/3}$. The measured conductivity of the ball-rod

joint was within about 20% of the calculated value for a wide variety of materials we tried. The scheme appears to work very well. We expect a total of about 2 W of heat loss through the kinematic mount. The total deflection in the ball-rod mounts under their static 50 N load is 3 μm ; in addition, each ball can support as much as 7 N vertically and 20 N longitudinally from variable gravitational loading. The resulting differential deflections from the zenith to the survey altitude limit is of the order of 0.8 μm .

The one disadvantage we know about this scheme is that the stresses on the balls and rods are very high owing to the tiny contact area. There is no danger of failure at the static stress levels, but dynamic loading associated with handling could easily permanently deform either member. To avoid this, each dewar uses a set of four electroformed nickel bellows that are pressurized with dry nitrogen at about 300 kPa (these exert the roughly 10 N static forces referred to above) to bring the optical benches into contact with the kinematic mounts for observing (Fig. 14). When the camera is being mounted or moved, this pressure is relieved, and springs retract the optical benches about 1 mm. At the same time the retraction of the bellows engages a latch at each end of the Tbar that snaps into place as the Tbar retracts and latches it away from the kinematic mounts.

In general, since the loading changes as the survey goes on are very slow and the astrometric calibration through

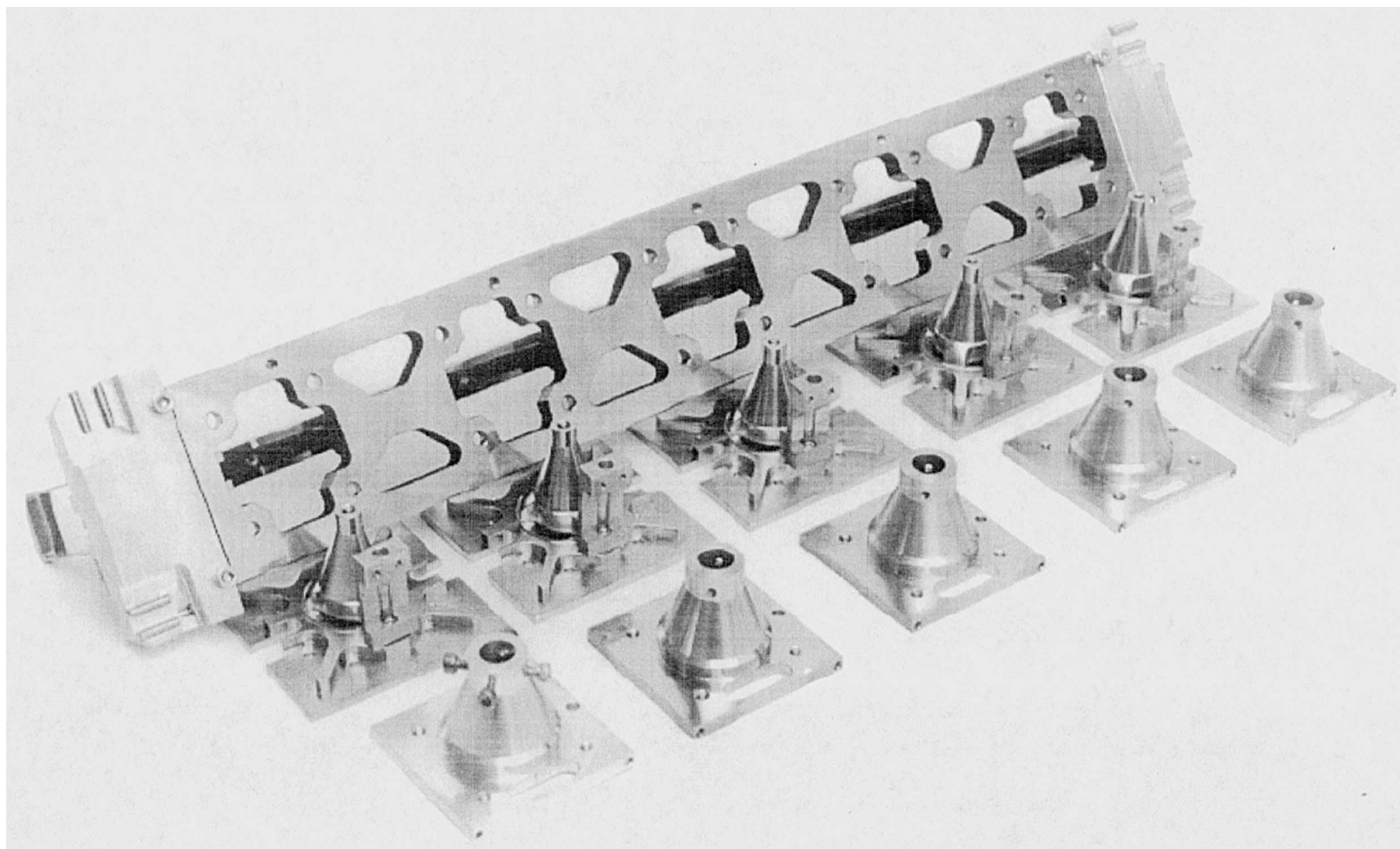


FIG. 7.—Photograph of a disassembled photometric dewar at an early stage of construction. The tubes that carry pressurized nitrogen to the kinematic mount bellows can be seen, as well as the backplane circuit board, which interconnects the in-vacuum preamp/clock-driver boards with the hermetic connectors that carry the signals into the vacuum. The CCD mountings on the Tbar can be seen, as well as the copper cold posts, which carry heat from the CCDs to the cold strap assembly.

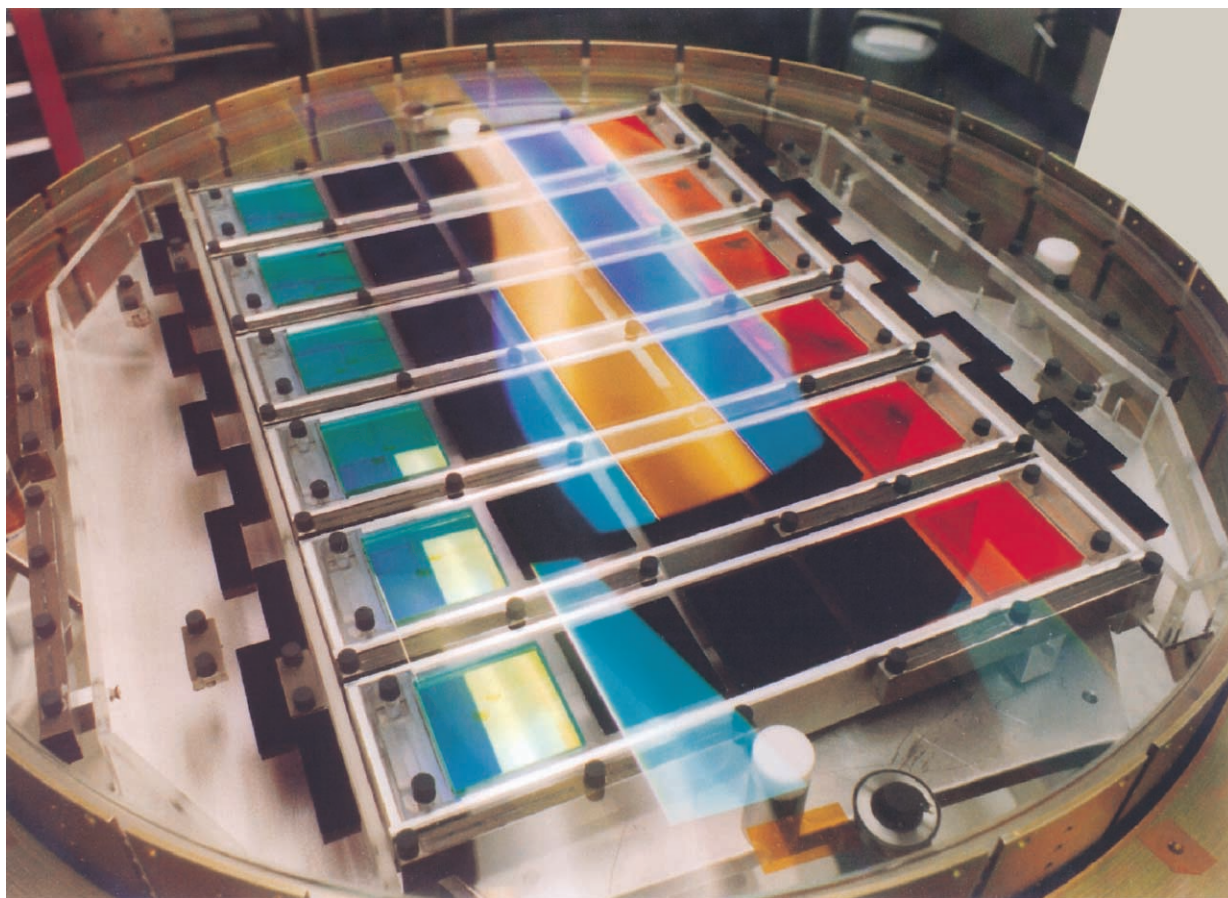


FIG. 8.—Photograph of the front surface of the corrector showing the filters cemented onto the back face. The striped antireflection coating can be seen in the foreground, as well as a hint from the reflection of the ceiling fluorescent light tubes of the extremely aspheric surface of the element. The focus chip filters had not been glued on at the time this photograph was taken.

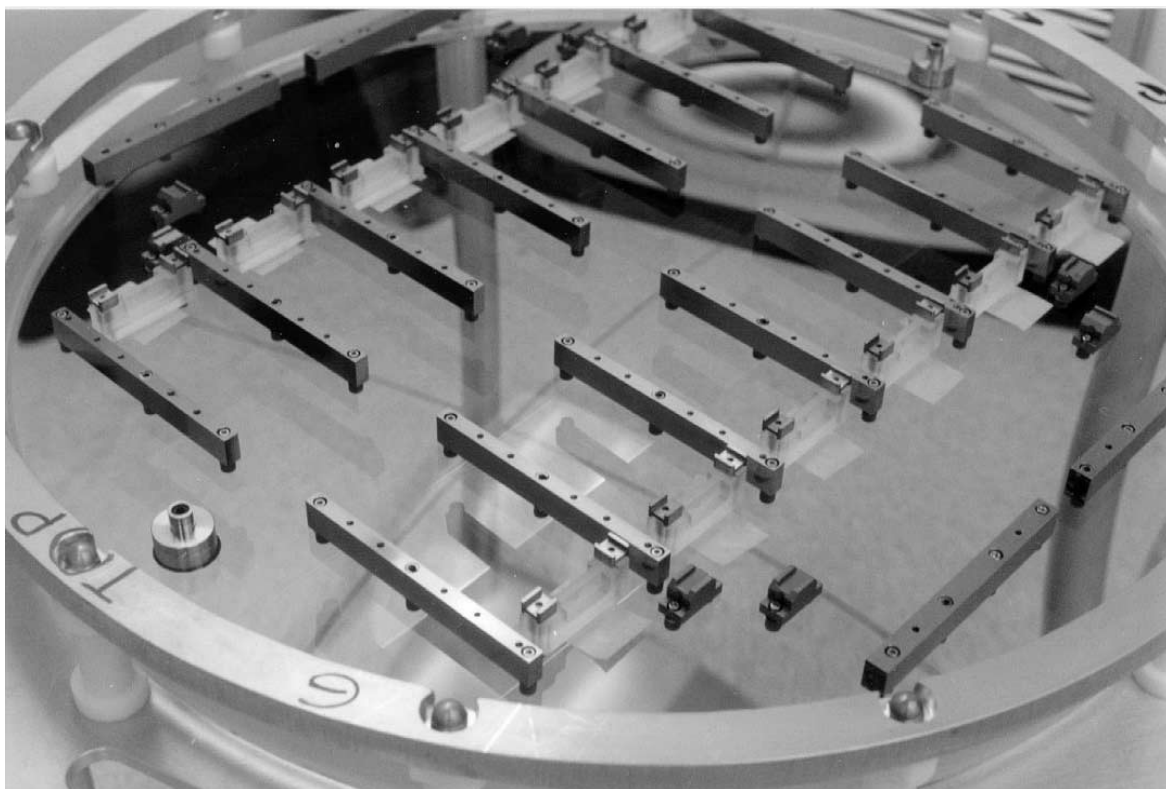


FIG. 9.—Photograph of the rear surface of the corrector before the filters were cemented on, showing the dewar mounting rails and the quartz pillars for the Tbar kinematic mounts. Again the reflections of the ceiling fluorescents (the ring-shaped feature in the top right) show the peculiarity of the front figure.

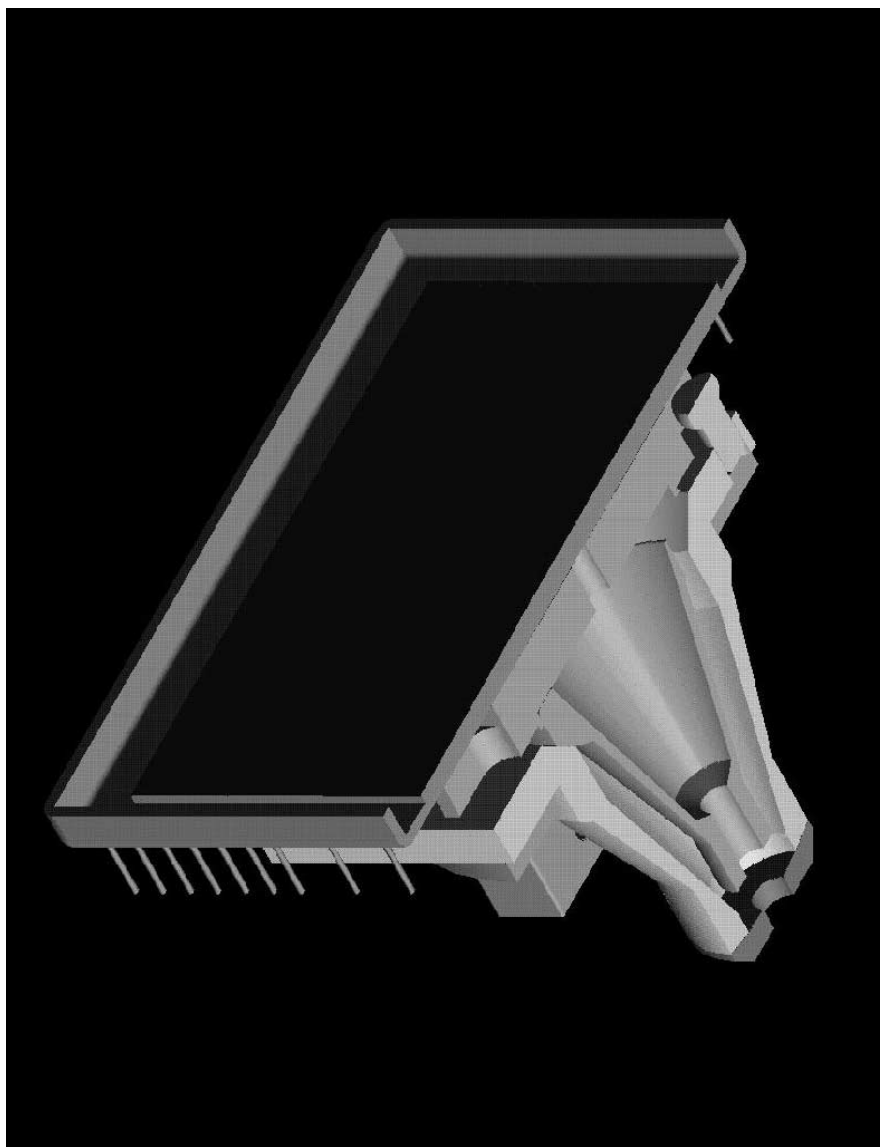


FIG. 10.—Pro/Engineer CAD drawing of the CCD on its mount, here displayed as a cutaway. The ball-and-cone socket nature of the mount can be seen, as well as the Kovar stiffener to which the CCD is cemented.

astrometric standards is a continuous process, the contribution to the astrometric error from the deflections discussed above should be negligible; in any case, the errors are much smaller than those expected from telescope deflections and drive irregularities. The overall deflection of the corrector in the focus direction (which is the only direction there are appreciable deflections) is about $2\text{ }\mu\text{m}$ neglecting the stiffening by the dewar bodies. At worst, focus changes induce centroid motion (from an overall scale change) a factor of 20 smaller, so there is no appreciable error from this source. Since the dewars in this design are simply vacuum enclosures and, except for the flexibly coupled preload bellows, pushrods, and thermal straps (see § 6), do not even contact the optical benches, the load paths are very direct from the kinematic mounts to the telescope structure. The only tricky part of the design is the fact that there was a fair amount of machining to do on the quartz corrector. There are about 100 holes for screw anchors for the kinematic columns and the dewar mounting rails. The screw anchors consist of knurled brass inserts epoxied into these holes (see

Fig. 9). The whole process went without mishap, though there was a fair amount of anxiety in the beginning, as there was in applying the striped coatings onto the corrector.

Thermal stability is a major concern for the Tbars, as are the physical dimensions; locating the CCDs in all three dimensions to the required accuracy was not easy. The photometric Tbars are made of Super Invar ($^{32}\text{Fe}^{5}\text{NiCo}$), whose thermal expansion coefficient is around 0.4×10^{-6} at room temperature. The Tbar, because of its complex shape and the required precision, had to go through a special manufacturing process. The machining was done in the new shops at the National Observatory of Japan in Mitaka, Tokyo, with extensive use of wire EDM in order to minimize mechanical distortion. The Tbars were annealed (600°C for 1 hr) five times, once after every major cutting operation, in order to release mechanical stress and ensure stability. The last annealing was done by holding the temperature at -100°C (near the detector operating temperature) for 1 hour and then raising it to 200°C for 1 hour. The final measurements of the mounting face of the

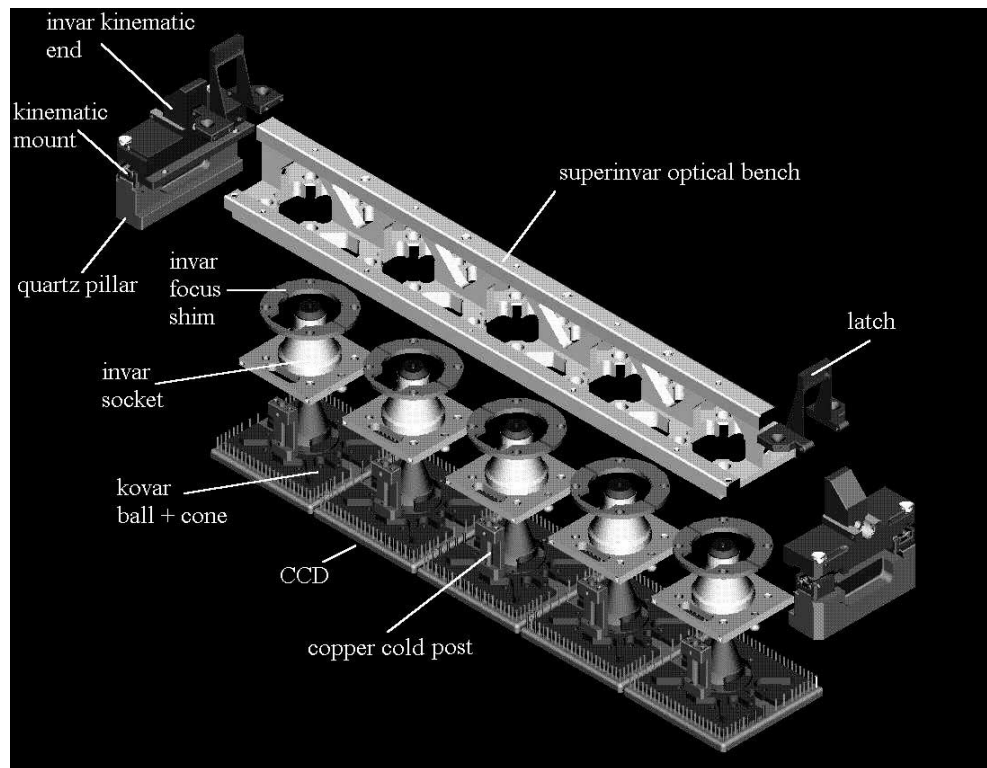


FIG. 11.—Pro/Engineer CAD representation of an exploded view of the Tbar assembly. Refer to the photographs in Figs. 7 and 12.

Tbar show that deviations from an ideal flat plane were typically smaller than $20\text{ }\mu\text{m}$, and most of this was essentially pure twist. The 50 N forces holding the Tbar to the kinematic mounts are more than sufficient to flatten this.

It is necessary to adjust the tilt, rotation, and focus of each CCD on the Tbar fairly exquisitely; we allow $25\text{ }\mu\text{m}$ tilt error, $5\text{ }\mu\text{m}$ rotation error, and $25\text{ }\mu\text{m}$ total piston error. The tolerances on the absolute (x , y) location of the CCD are not so severe, though we succeeded in locating all the chips within about 1 pixel ($24\text{ }\mu\text{m}$).

The tilt adjustment was done on initial assembly of the ball-and-socket joint to theoretical optical design values. It can be changed on the basis of later tests but only with some difficulty; we feel, however, that it is the most reliable of the adjustments to predict. The rotation and tilt adjustments were done on a measuring machine that incorporates an accurate XYZ stage carrying a microscope and a precision linear slide upon which the Tbar is mounted on kinematic mounts like the ones on the corrector (Fig. 15). Precisely made stepping blocks allow positioning the Tbar on its slide so that each CCD in turn is positioned accurately at the same position in front of the microscope stage by the insertion of one more block. The microscope has a very fast inverse-Cassegrain objective that allows z -motions to be measured using focus alone to an accuracy of about $2\text{ }\mu\text{m}$; a crosswire reticle allows positioning in the image plane to about $1\text{ }\mu\text{m}$. The three-dimensional coordinates of six reference points on the CCD die (four at the corners and two at the serial register splits) are obtained and the adjusting screws manipulated until the tilt and rotation are correct; the rotation is adjusted by means of a long (250 mm) rigid lever attached temporarily to the socket part of the CCD mount and moved with a micrometer. Though the adjustments are not in themselves micrometric and a

certain amount of iteration was necessary the procedure converged reasonably quickly, the adjustment of a Tbar was typically accomplished in less than 1 day. The piston was set with a set of shims to match the design focal plane (see Fig. 11 above) and it may be necessary to refine these (and the rotation) using measurements of the sky, though the measured parameters of the as-built optics indicate that the real focal plane will deviate from the design one by no more than $10\text{ }\mu\text{m}$.

The measurements show this procedure is quite accurate; the rotation is fixed within $3\text{ }\mu\text{m}$ rms, and the error of tilt and piston is together only $10\text{ }\mu\text{m}$ rms, which results in image degradation of only $2\text{ }\mu\text{m}$ and tiny (less than 1 mas) maximum astrometric errors.

The dewar bodies themselves are machined of aluminum (see Fig. 7) and have O-ring seals to the quartz in front and to a fitted lid, which carries the cooling system and electronics in back (Figs. 16 and 17). They are about 75 mm tall and 330 mm long, so the atmospheric pressure on the side walls results in about 2500 N when they are evacuated. This force is taken up by a lip on the lid of the dewar in back and in front by a frame machined integrally into the piece, which consists of horizontal stiffening bars between the filters. Thus the forces do not act on any dimensionally critical element. A similar force in the focus direction acts to seal the quartz to the dewar body and demands that the face of dewar body be quite accurately flat in order that it not distort the rear surface of the corrector. This would have no optical consequence, but would change the effective shape of the focal plane. This strong bond with the dewars results in considerable stiffening of the corrector by the dewars, since the Young's moduli of aluminum alloys and quartz are similar; though the dewar walls are relatively thin (about 1 cm) they are twice as deep as the corrector is thick,

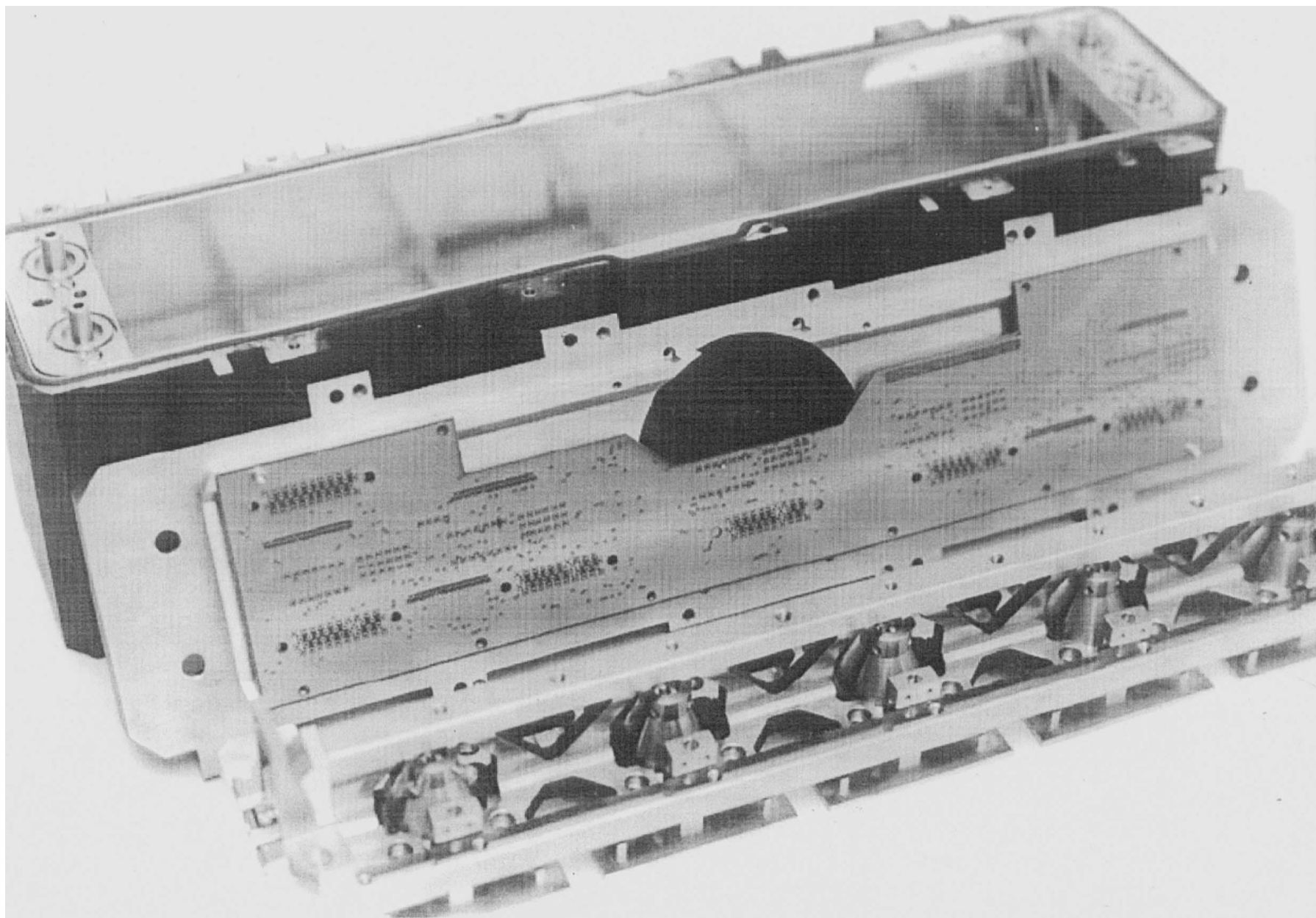


FIG. 12.—Photograph of the photometric Tbar assembly, showing the Tbar itself and a set of ball-and-socket mounts. Note the four tilt-adjusting screws in the front socket. The Kovar stiffener/ball mounts have the copper cold posts attached, and the Tbar has its kinematic ends mounted with the upper set of rods for the kinematic mounts in place.

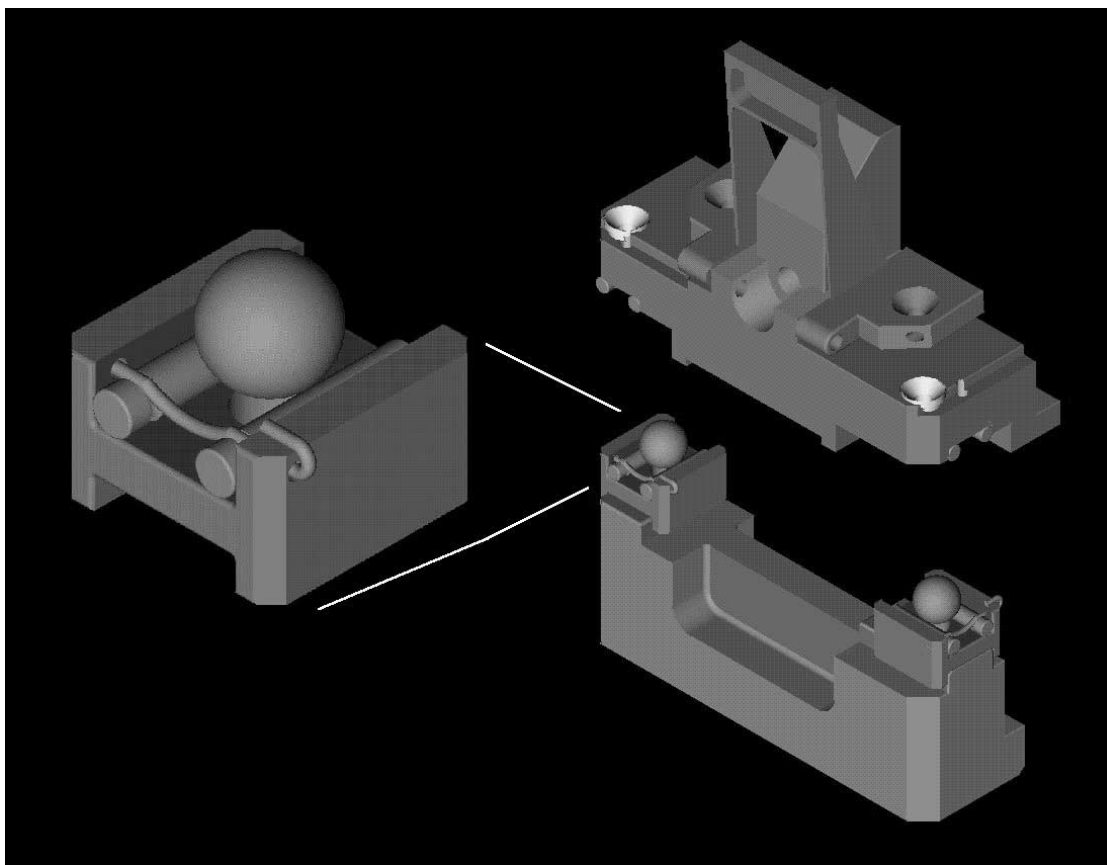


FIG. 13.—Pro/Engineer exploded view of a Tbar kinematic mount and latch. The bellows have Delrin extension posts, which engage the conical holes in the latch plate and pivot the plate down to disengage the latch hook as they extend.



FIG. 14.—Photograph of bellows and springs that pull the Tbar away from the kinematic mounts when the bellows are relaxed. Missing is the small spring that keeps the latch engaged then. The Tbar is raised by the springs and engages conical stops mounted on the thin-walled tubular stainless steel tripod structure when the bellows are relaxed. It is held reasonably securely there, but the camera must be vertical for the latches to operate satisfactorily.

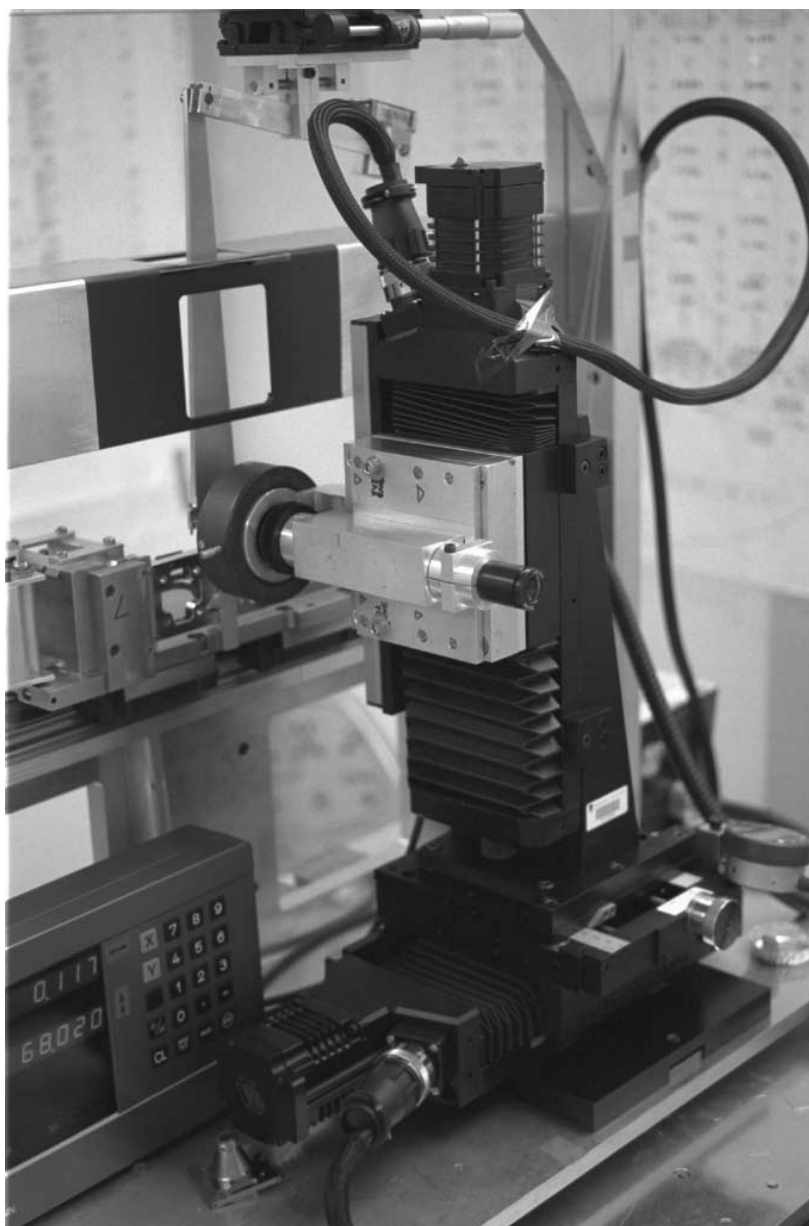


FIG. 15.—Stage of the XYZ measuring machine used to set up the tilt and rotation and verify the focus of the photometric CCDs on the Tbars. A Tbar can be seen mounted on the carriage of the linear rail just in front of the microscope illuminator.

and most of the stiffness is, in fact, in the dewars. The great disparity of their thermal expansion coefficients, however, demands that the joint have rather low friction; thin polyimide gaskets appear adequate to the task. When the dewar is removed, cleats machined into it bring the optical bench away with it for ease of maintenance. The optical bench can then be removed from the dewar through the top, carrying the in-dewar circuit boards with it after they are detached from the wall of the dewar and attached via special fixtures onto the optical bench.

5. THE ASTROMETRIC/FOCUS ARRAY

5.1. Concept

We need reasonably good relative astrometry to place the fibers for spectroscopy. Allowing for errors arising from differential refraction with wavelength and position, hole

placement uncertainties, etc., it seems necessary to find positions to accuracies of the order of ≈ 200 mas ($12 \mu\text{m}$ in the focal plane). This is difficult to do with the photometric array, because it saturates at about 14th magnitude in the bands most useful for astrometry (g' and r' , with r' preferred because of the smaller refraction corrections), and there are very few astrometric standards at this brightness level. It would be, in principle, possible to calibrate the camera astrometrically, but one would have to depend on its stability and the stability of the telescope drives for relatively long periods to make use of the calibrations without suffering intolerable overheads. This problem can be solved, however, by using the astrometric array of CCDs, which allow us to tie much brighter astrometric standards to the positions obtained from the photometric array.

The astrometric/focus camera uses 24 2048×400 front-side CCD chips working in the r' band and mounted in the

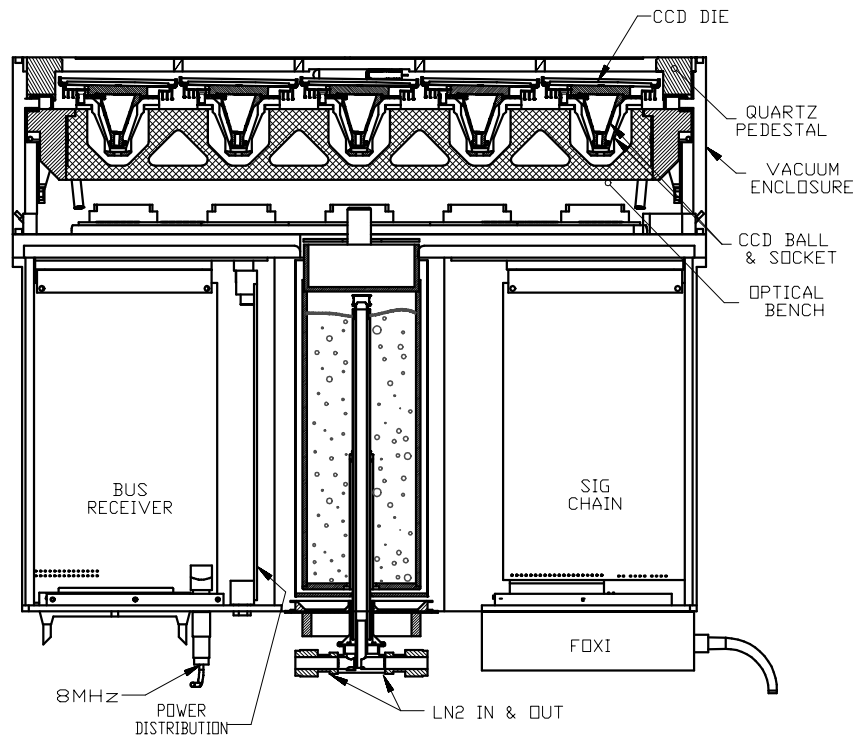


FIG. 16.—Cutaway drawing of a photometric dewar, showing the layout of the CCDs and kinematic mounts, and that of the circuit boards, FOXI transmitter, and LN2 container.

available space above and below the photometric array (see Fig. 1). With these chips the integration time is reduced by about a factor of 5 (400/2048) relative to the 54 s photometric exposure time; the chips are front-illuminated devices without coatings, which are less sensitive in the red than the thinned photometric chips by a factor of about 2, so without further filtration the saturation level is brightened by about 2.5 mag, to about 11.3. This is still not particularly useful, since the *Hipparcos*/Tycho net and the AGK3 (whose positions are probably not good enough anyway) both have very few objects as faint as 11.3. To reach brighter standards, we employ neutral-density filters with 3.0 mag of attenuation, which, together with shorter integration times and the use of front-illuminated devices, enable us to observe astrometric standards as bright as $r' = 8.3$.

The disadvantage of the shorter columns is that the shorter integration times lead to larger position errors because of seeing-related image wander. With an 11 s integration time in 1" seeing, Kolmogorov seeing theory suggests that the one-dimensional positional accuracy achievable in that time is about 50 mas with the two passes for each star. We will see below that we encounter about one astrometric standard every 10 s or so, so the ultimate astrometric accuracy is critically dependent upon the short-timescale accuracy of the drives (as well, of course, on the short-timescale dimensional stability of the camera and telescope, but we expect negligible errors from these sources). Given sufficient stability so that we need to make negligible corrections on the 1 minute effective exposure timescale, we should be able to standardize to of the order of $50/\sqrt{5} \approx 20$ mas.

The response of the astrometric detector system is given in Figure 18, where the sensitivity of the astrometric system has been multiplied by a factor of 10 to facilitate compari-

son with the photometric system. The filters, 15 mm wide and 55 mm long, are composed of a 2.5 mm thick piece of NG4 and a 3.3 mm thick piece of OG 550 with the short-pass interference coating on the free surface. The OG 550 is figured on the coated surface to act as a field flattener; the astrometric CCDs are manufactured to have the same curvature as the mean photometric device. We intended the filters to have the same passband as the photometric r' , but the short-pass interference coating on them, which was supplied by a different vendor from the r' filters in the photometric array, was delivered with a cutoff wavelength 50 nm too long. It was deemed in the light of schedule pressure that replacement was not warranted; the main effect is that the attenuation is slightly less than desired.

These chips can be run somewhat warmer than the photometric imaging devices because we are not interested in low signal-to-noise objects and the integration time is short. Cooling to -60°C is sufficient, which yields a background of about $10\text{--}20\ e^-$ per pixel in the 11 s integration time. This background is actually useful; the astrometric chips display rather poorer horizontal CTE than the photometrics for reasons that may be connected with cross talk in the clock signals in the FPC connecting the chips to the electronics, and the effect is lessened in the presence of even such a small background.

The centroid of a star that deposits about $2000\ e^-$ ($r' \approx 16.6$) can be measured to about 30 mas (shot and readout noise errors alone) in 1" seeing with this background. A star that saturates in the central pixel ($4 \times 10^5\ e^-$ for these devices, $r' \approx 8.3$) has a total signal of about $4 \times 10^6\ e^-$, so the dynamic range for 30 mas accuracy, considering shot and read noise alone, is about 8.3 mag. This yields an overlap of about 2.5 mag between saturation of the imaging array (about 14.0 mag) and the 30 mas accu-



FIG. 17.—Photograph of circuit boards under test on a photometric dewar lid, showing power cable, CCD clock bus ribbon, 8 MHz line, and top boards. A set of power supply boards can be seen in the background.

racy limit for the astrometric array. There are more than 200 stars deg^{-2} in that magnitude interval near the pole, so that of order 10 are on any photometric CCD at any given time. Thus the frame defined by the astrometric chips and the one defined by the red imaging chips (and with only a little more difficulty, that defined by any band in the imaging array) can be tied together very accurately.

The array uses 12 devices in each of two nearly identical dewars, one leading the photometric array and one trailing; one device in each dewar (which has a special stepped-thickness r' filter but no neutral-density filter) is devoted to monitoring the camera focus. The sensors at the trailing edge provide a check on the tracking rate and direction as well as an independent astrometric calibration; stars cross

the bottom set 7.5 minutes after they cross the top, and they go through the red photometric sensors 1.4 minutes after they leave the top. Thus drive errors with frequencies lower than 2×10^{-3} Hz can be corrected for, and we can monitor higher frequencies statistically. The astrometric and red sensors define a continuous frame that will drift slowly with respect to any initially defined absolute frame because we are basically measuring rates. We will use the astrometric standards only to pin this instrumental frame to the sky at intervals.

There are about 11 *Hipparcos*/Tycho stars per square degree at the pole in our magnitude interval, and the CCD array will encounter one every 10 s on average. If the drives can be held to the accuracy we would like (25 mas rms

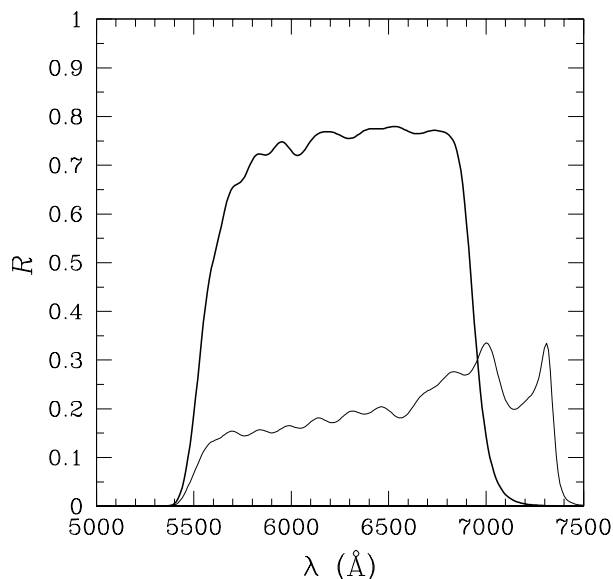


FIG. 18.—Response of astrometric detector/filter system (*light curve*) scaled up by a factor of 10 and compared with the photometric r' response (*heavy curve*). The extension to the red of the astrometric passband is clearly seen. Not included in the scaling is the effect of the factor of 5 shorter exposure times owing to the reduced extent of the astrometric CCDs in the scan direction.

stochastic component in the frequency interval 2×10^{-3} to 3×10^{-1} Hz), as seems very likely from measured errors on the manufactured parts, we should be able to tie the survey to the *Hipparcos* net to an accuracy of better than 50 mas. In order to measure positions well enough to place fibers for the spectroscopic part of the survey, it is necessary to have errors of the order of 200 mas or less, and the seeing places limits of 30 or 40. Various scientific desiderata demand, of course, arbitrarily high precision. Bettering the limits imposed by seeing would have been prohibitively difficult and expensive, but we decided early in the project to attempt to keep the errors near that limit. This has been relatively easy and inexpensive to do in the design and construction of the camera; the situation for the telescope and its bearings and drives is not quite so clear at the time of this writing.

5.2. Mechanical Design of the Astrometric/Focus Array

The linear dimension associated with the expected 30 mas seeing error is about $2 \mu\text{m}$, and achieving dimensional stability to this order over a focal plane as large as ours is not an easy task. Invar 36 has a thermal coefficient of expansion of about 1.5×10^{-6} per degree Celsius, and a temperature change of 1°C induces a dimensional change of $0.7 \mu\text{m}$ over the 455 mm width of the array, so a 1°C temperature control is adequate. The coefficient for silicon is similar, and changes on the scale of one chip with reasonable temperature control are negligible. Our approach to the astrometric array is thus very similar to that for the photometric except for the mounting of the CCDs; the Invar 36 headers for the astrometric chips are mounted with screws onto an Invar 36 optical bench, which goes across the array, on Invar shims machined with the tilts necessary to fit the field curvature. The astrometric Tbar is shown in Figures 19 and 20. The shorter vertical dimension means that rotation is not so critical, and shimming for piston will be the only adjustment normally performed. The optical bench is located to the corrector with kinematic mounts of the same

sort as used in the photometric dewars, but here the pillars are much smaller, shorter, and are made of Invar instead of quartz (see Fig. 9). The optical bench is housed in an aluminum dewar attached to the corrector in the same fashion as the photometric ones, again with an O-ring seal against the quartz. Reinforcing the dewar against transverse atmospheric pressure is trickier in this case than in the photometric case because there is no clear place to put a spreader bar close to the focal plane with the chips overlapping as they do, but spreaders behind the main horizontal web of the optical bench through holes in the vertical web serve here. This complicates the assembly somewhat, but not overly. A dewar of either variety can be disassembled to the point of removing the optical bench or reassembled in the order of an hour.

The dimensional relationship between front and rear ranks of the astrometrics is also crucial to control, since it determines the accuracy with which errors in the drive rate and direction can be measured. This is greatly facilitated by our use of the quartz corrector as the metering substrate. The dimensions should not be much less accurately maintained than those within one of the optical benches, particularly when one considers that the deflections associated with the kinematic mounts are the same for the front and rear benches (and furthermore quite similar to those for the photometric benches).

5.3. The Focus Chips and Focus Servo

One of the major contributions to image degradation in normal observing circumstances at most telescopes is the inability to keep up with focus changes brought about by flexure and temperature changes. Our requirements are especially severe because of astrometry, but it appears that a simple scheme will suffice to provide excellent control.

There are two astrometric-type sensors housed in each of the astrometric dewars, which are used as focus sensors; though they are quite far from the center, the image quality is sufficiently good at their locations that they are ideally suited to monitor the focus. They have only an r' filter with no neutral density; this filter is cut into three parts, and the optical thickness associated with the neutral filter on the sensors is taken up by three clear glass (BK7) spacers of varying thickness (1.9, 2.8, and 3.7 mm, in addition to a 3.4 mm Schott OG 550 glass element). When the rest of the array is in focus, the center of the focus chip is also, but the ends are $300 \mu\text{m}$ inside and outside of focus, respectively; this defocus, which results in image degradation from defocus comparable to the expected $1''$ seeing, is optimal from a focus-determination signal-to-noise point of view. In this way, comparison of the images in the outer two-thirds will provide a sensitive differential measure of the focus, which we will adjust dynamically; the resolution of the secondary motion is such that it should cause us no difficulty. Figure 21 shows images at five positions on the focus sensor through focus with $150 \mu\text{m}$ focus steps, as produced by the design optical system and convolved with 0.8 Gaussian seeing.

We need to control the focus very accurately to maintain astrometric accuracy. If we require $2 \mu\text{m}$ positional accuracy in the focal plane, we must control the focus to about $35 \mu\text{m}$, since the maximum angle that the central ray makes to the focal plane is about 0.055 rad. Focus errors of this size contribute only $7 \mu\text{m}$ rms to the image diameters and are negligible, but we would like the focus errors to be



FIG. 19.—Photograph of astrometric CCDs on a partially assembled astrometric Tbar. The focus sensor and bridge chips are mounted. The FPCs and light shields mounted on the CCDs can be seen.

negligible for the astrometric determinations. The factors that contribute to focus errors are residual aberrations across the field of the focus chips, photon statistics, and most important, seeing. The focus errors from aberrations and photon statistics (the actual errors will almost certainly

be dominated by seeing) are about $3\ \mu\text{m}$ for any star brighter than about $r' = 15.5$, the limit set by PSF variations across the focus chip. For fainter objects, photon noise becomes important, and the errors are about $6\ \mu\text{m}$ at 17 mag, $9\ \mu\text{m}$ at 18 mag, and $20\ \mu\text{m}$ at 19 mag. At the Galactic

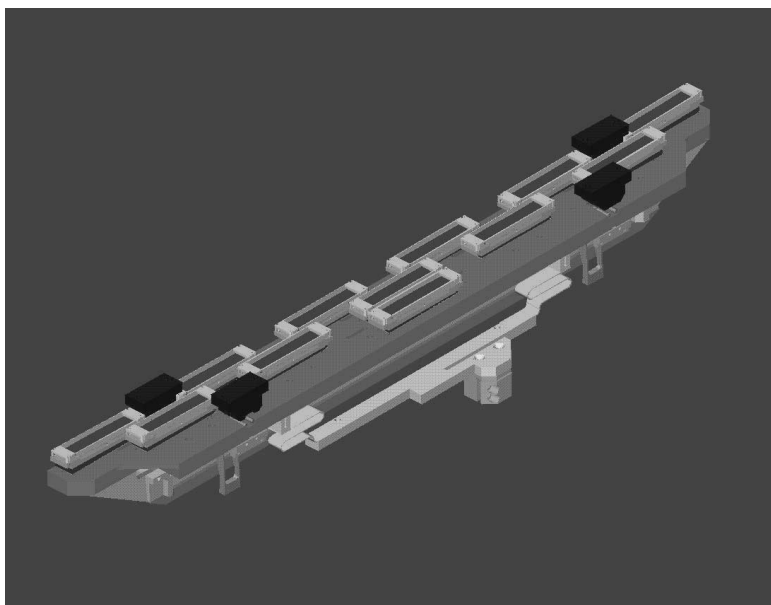


FIG. 20.—Pro/Engineer drawing of an astrometric Tbar, showing all CCDs, the astrometric kinematic mounts, and the cooling assembly

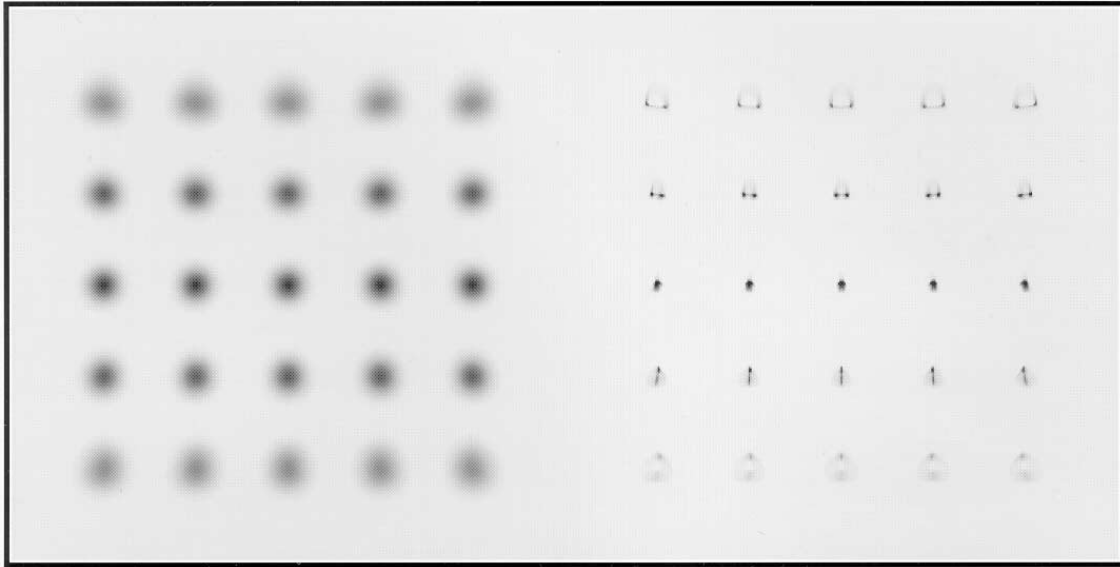


FIG. 21.—Images at the focus sensor through focus, as produced by the optics alone on the right and convolved with $0''.8$ FWHM Gaussian seeing on the left. The five images horizontally are at five locations across the chip. The center images vertically are in focus, and progressively out of focus in $150\ \mu\text{m}$ steps in both directions.

pole, the star counts are about 160, 350, 550, and $880\ \text{deg}^{-2}$ brighter than 15.5, 17, 18, and 19 mag, respectively, and fainter than the saturation limit at $r' = 11.3$ mag. The three focus zones are each about $4'$ wide, so the camera will see about 0.0167 square degrees per minute of time in each of the zones. Thus it will see three stars brighter than 15.5 mag, six brighter than 17 mag, nine brighter than 18 mag, and 15 brighter than 19 mag per minute. The timescale for focus changes is not well known yet, but the thermal time constant for the telescope is of the order of 1 hour, so it seems not unreasonable to expect that one can effectively average over a hundred to a few hundred stars to generate a focus signal, and the statistical errors are expected to be negligible.

6. THE CCD COOLING SYSTEM

The dark currents for the Tek/SiTe CCDs range from 30 to about $200\ \text{pA cm}^{-2}$ at 20°C . At -80°C , this is reduced by about a factor of 3×10^5 , which for a $24\ \mu\text{m}$ pixel becomes $0.01\ e^- s^{-1}$ for 100 pA at room temperature. The sidereal-rate exposure time of 54 s thus yields a dark signal of about $0.5\ e^-$, which does not contribute significantly to the read noise. We could have chosen to run the devices warmer without serious degradation of the data, though considerably more care in monitoring the dark current contribution to the background would have been necessary. The thermal losses at -80°C are roughly evenly divided between conductive (which scale linearly with the difference between operating and room temperature) and radiative (which are almost independent of operating temperature), and operating warmer would not have made a major impact on the thermal design. The CTE of the detectors, which is not outstandingly good by today's standards, seems to be influenced not at all by temperature over any interesting range. It is true that we could have bought some extra sensitivity in the z' chips by operating warmer, but they, the oldest and hence earliest produced devices in the camera, have cosmetics that are much better at low tem-

peratures, and the extra sensitivity is mostly bought by extending the response into the infrared where the optical performance is not very good. The savings in liquid nitrogen consumption that might be realized by operating warmer are also not very great. All these factors and a general conservatism ("We'll design it to run cold, but if we have to back off it will not kill us") led to the choice of operating temperature.

The total thermal losses for the dewar design we are using come to about 10 W per dewar, 3 W from radiation from the detectors (mostly from the active detector area itself), 2 W through the kinematic mount, 1 W from radiation to the optical bench (which has a gold-plated thermal shield), 1 W from radiation to the nitrogen container (also gold-plated with a secondary shield), about 2 W from the temperature-control makeup heaters, and another 1 W from miscellaneous sources such as conductive losses through the flexible printed circuits (FPCs) connecting the CCDs to their support circuitry, conductive losses to the force actuators on the kinematic mounts, etc.

We use an autofill LN2 cooling system similar to the one used on the 4-Shooter camera at Palomar (Gunn et al. 1987). Each dewar has a small LN2 container holding about 400 ml of liquid (Fig. 22), which keeps the detectors cool for a little less than 2 hours. Under normal operating conditions all the LN2 dewars vent through a common vacuum-jacketed fill line and are kept under moderate pressure. There is a temperature sensor on the LN2 dewar body that is monitored continuously, and the dewar is filled when its temperature rises, but normally the dewars are filled on a schedule kept by the executive microprocessor (see below—we currently fill once an hour) that ensures that they never go empty. The fill is accomplished by opening all the solenoid valves on the individual vent lines and allowing liquid under pressure to enter; these are closed one by one as the dewars fill (as indicated by thermistor-based liquid sensors in the vent lines).

The heat is conducted from the chips through the Kovar



FIG. 22.—Photograph of the LN2 container used in both the photometric and astrometric dewars. It is a vacuum-brazed assembly of copper with welded stainless steel plumbing. It holds 400 ml of liquid nitrogen. The Swagelok fittings at the near end mate to the supply and vent lines; the post at the far end mates to the cold-strap assembly shown in Fig. 23.

cone mounts cemented to them, and then to copper posts that are connected via multilayer silver straps the individual leaves of which are $50\text{ }\mu\text{m}$ thick (silver is only slightly more conductive than copper but is nearly a factor of 2 more flexible at a given cross section) to a cold finger on the base of the LN2 container, which houses a Zeolite molecular sieve getter. The very low heat conductivity of Invar makes it difficult to keep the optical bench isothermal, but we keep the chips at a uniform constant temperature with small makeup heaters associated with each CCD and mounted to the copper posts, as seen in Figure 23, which attach directly to the CCD mounts. It is possible because of the low conductivity of Invar and the rather poor thermal contact between the CCDs and the optical bench to operate the devices at quite different temperatures if desirable, and we may choose to operate the u' devices colder to minimize their somewhat higher dark currents, though it is not a serious problem at -80°C . The thermal expansion coefficient

of Invar is so small that small deviations from isothermality have little effect on the dimensional relationship in the bench. The temperatures are measured with small platinum resistors fed with resistive dividers that result in a reasonably accurately linear response over the relevant temperature range. Sensors of the same type are used to monitor the temperature of the LN2 container.

The situation for the astrometric dewars is quite similar. At an operating temperature of -60°C the total heat load to the astrometric optical bench is about 6 W, roughly the same as the photometric dewars. We have decided for simplicity and economy to use a cooling system essentially identical to the one adopted for the photometric dewars, and in fact one which shares many parts with its photometric counterpart. For astrometric accuracy, we must endeavor to keep the bench as isothermal as possible. The bench has a cross section of about 7 cm^2 , and the conductivity of Invar is about $0.2\text{ W }(^{\circ}\text{C cm})^{-1}$, so a flux of 1 W in

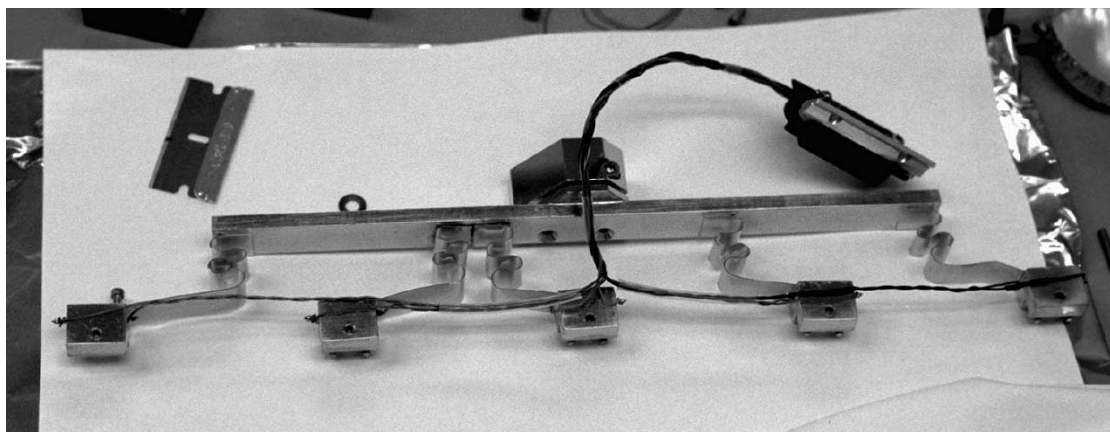


FIG. 23.—Photograph of the cold-strap assembly for a photometric dewar. The clamp at the top mates to the cylindrical post on the LN2 can, and the blocks at the bottom attach to the copper cold posts on the CCD mounts (see Figs. 7, 11, and 12). The leaves that attach these blocks to the heavy copper spreader bar are made of multiple layers of 2 mil thick silver and are very flexible.

the bench is associated with a temperature gradient of about $0.7^{\circ}\text{C cm}^{-1}$. Temperature differences across the bench of 1°C induce a bow in the bench with an amplitude of about $1\text{ }\mu\text{m}$. We distribute the heat load from the bench to a heavy cold bar attached to the LN2 container's cold finger at four points along the optical bench, each point associated with a makeup heater and a temperature sensor. The connection is again made using thin silver straps. This results in temperature inhomogeneities of the order of 1° , but in a pattern that should remain quite stable and hence astrometrically innocuous.

On the saddle that carries the power supplies (see § 8) are mounted two 10 liter intermediate supply dewars that supply the autofill system, each one supplying LN2 for one astrometric and three photometric dewars through a vacuum-jacketed transfer line into the camera body and then along thin-wall stainless tubes insulated with closed-cell polyethylene foam to the individual CCD dewars. These in turn are kept filled from a 160 liter dewar on the rotating floor of the enclosure, using an autofill system of necessarily rather different design but similar principle.

The approximately 10 W of dissipation in a dewar means that about 250 ml of LN2 is consumed per dewar every hour. Including six dewars and two astrometric dewars, the total consumption of LN2 is about 2 liters per hour, or 50 liters per day. Thermal losses inherent in venting the camera dewars back through their intermediate supply dewars

increase this consumption by about a factor of 1.5, and losses incurred in transfer roughly double this with the system in its present preliminary state. We hope to reduce the consumption significantly when the system is properly tuned.

7. THE ELECTRONICS

7.1. Overall Design

The electronic circuitry for the camera is implemented on 207 circuit boards of 31 basic types. The boards are a mixture of through-hole and surface-mount PC cards, and in addition there are several one-of-a-kind logic and utility boards that are wire wrapped. For the most part, the boards can be accessed and replaced without serious disassembly (not true of a few boards in the dewar vacuum) and it is planned to keep a complete set of spares with the camera. The object of the design was to make the system as modular as possible, and to eliminate as far as possible hand wiring of boards, cables, and connectors. In this we feel that we were moderately successful. We discuss here primarily the active boards associated with the detectors and describe briefly some of the other circuitry.

The conceptual diagram of the CCD electronics is shown in Figure 24. As in any CCD system, the electronics consists basically of two streams, the digital signals that control and clock the CCD and the outgoing analog video signals that

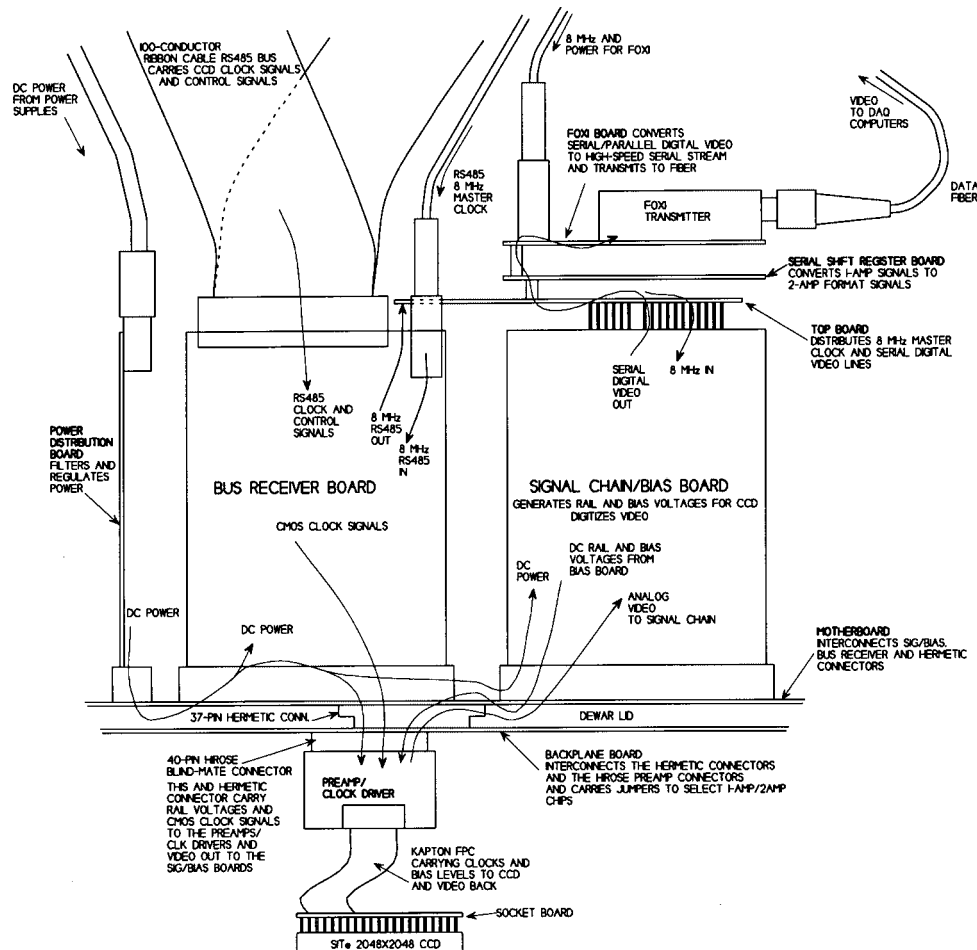


FIG. 24.—Conceptual diagram of the wiring of a photometric dewar, showing the main signal pathways and functions of the various circuit boards. See Figs. 16 and 17 for the actual physical layout.

must be processed and digitized. The clock waveforms are generated by one of two on-board microprocessors, the *phase micro*, which forms the intelligence for the *CCD controller*. These signals are bussed to all the dewars over an RS-485 bus and are received and converted to CMOS digital signals by the *bus receiver board* in each dewar. The rail voltages are generated by digital-to-analog converters (DACs) and buffered on the *bias board* for each chip. The CMOS clock signals and the rail voltages go into the vacuum to a small it clock driver board, where they are combined to generate the clock signals at the proper levels to drive the CCD. The video signals from the output FETs on the CCD go to a small *preamp*, which is mounted piggy-back on the clock driver board, one per detector. There they are amplified by a factor of 10 and converted to a low-impedance analog signal. It emerges from the vacuum and goes to a *signal chain board*, which is physically the other side of the bias board, where the signal is level-shifted, double correlated, sampled, and digitized. The serial output stream from the analog-to-digital converters (ADCs) on the signal chain board goes to the *serial shift register board*, one per dewar, which formats the digital output from single-amplifier chips into two data streams with the same timing as those from a two-amplifier chip. The 10 resulting serial streams then go to the *FOXI transmitter* where the streams are combined, converted to parallel, and then back to serial at 100 MHz to a fiber driver that sends the data to the data acquisition system in the operations building. The controller also handles various housekeeping chores, such as setting the bias DACs, monitoring the resulting voltages, controlling the shutters, monitoring among other things various system pressures and temperatures, and generating and driving the RS-485 bus signals and master 8 MHz clock signals. Most of the control jobs are handled by the *executive micro*, whose RS-232 line is one of two control links to the outside world. The numbers of the boards of various types and their electrical power dissipation are given in Table 6.

The clock drivers and the preamps are mounted in the dewars to minimize noise, ensure ground integrity, and minimize danger from electrostatic discharge, as was done in the Palomar systems (Gunn & Westphal 1981). The optical design has sufficiently good distortion characteristics, as we discussed in § 2, to allow clocking all the chips in the array synchronously, and hence the driver and digital control circuitry is relatively simple. The preamp, clock

driver, and signal chain/bias boards each have two independent channels corresponding to the split serial registers' CCDs. Each CCD is associated with either one or two analog signal chain channels, depending on whether it has one or two good amplifiers on the serial register in use. One channel on the boards belonging to single-amplifier chips is idle. Most dewars have only one single-amplifier device, but one has none and another has two. This peculiar circumstance was demanded by the distribution of readout noise and the acceptable noise thresholds for our five bands.

7.2. CCDs: Electrical Characteristics

The CCDs electrically are typical three-phase devices. The parallel waveforms as generated by the clock driver are sketched in Figure 25; T is the transfer gate signal. P3 is an MPP gate and must be clocked about 3 V more positive on its positive rail than the other two in order to buck the implanted potential for normal operation. We clock all the time, so there is not really an “integration” phase, but we hold P1 and P2 both high during the serial transfer time, which is the bulk of the time. The serial transfer signal (S1, S2, S3) is sketched in Figure 26. SW and R are signals for the summing well and reset, respectively. There are four other signals (IPC, I+, I−, and IR) synchronous with these for controlling the input clamp on the preamp and the double-correlated sampling integrator on the signal chain board. Recall that there are two sets of these serial signals a factor of 2 apart in frequency for the one- and two-amplifier chips.

The architecture of the serial registers on the devices is such that there are 20 “extended” pixels between the edge of the imaging array and the on-chip source follower amplifier, and we will read another 20 overscan pixels in the two-amplifier chips. Hence each half-row will consist of $1024 + 20 + 20 = 1064$ pixels. The single-amplifier chips will have the 20 leading and trailing extended pixels at either end of the data pixels and will, in addition, have 40 overscan pixels at the end. At sidereal scanning rate, the scale of $3.643\text{ mm arcmin}^{-1}$ corresponds to 38.05 lines per civil second, or $26.28\text{ ms line}^{-1}$. The vertical transfers require about $900\text{ }\mu\text{s}$, leaving 25.38 ms per line. We use 30 master clock cycles per pixel for all the functions in a classical dual-slope double-correlated sampling system (see Fig. 26), so a 1.3333 MHz (750 ns) clock yields $22.5\text{ }\mu\text{s}$ pixels.

TABLE 6

CIRCUIT BOARD COMPLEMENT

Part	Photometric	Astrometric
CCD	30	24
Photometric preamp	30	
Photometric clock driver	30	
Astrometric clock preamp		2
Astrometric clock driver		2
Signal/bias	30	12
Bus receiver	6	2
Power regulator board	6	2
Serial shift register	6	0
FOXI board	6	4

NOTE.—There are, in addition, eight unique boards associated with the camera controller, eight each of two different boards in the power supplies, and a board that controls the intermediate dewar automatic fill.

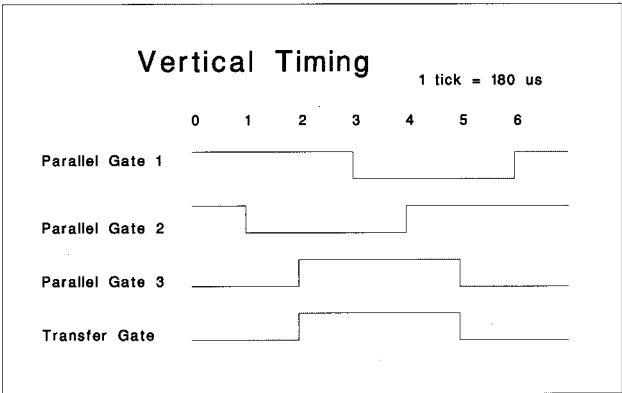


FIG. 25.—Timing diagram for the parallel transfer of charge. The time unit is eight complete (slow) pixel times, and the horizontal clocks except for the serial gates and the start-convert signal (see Fig. 26) continue to run during the vertical sequence to minimize line-start transients. Note that this parallel sequence is the same for all devices, slow and fast.

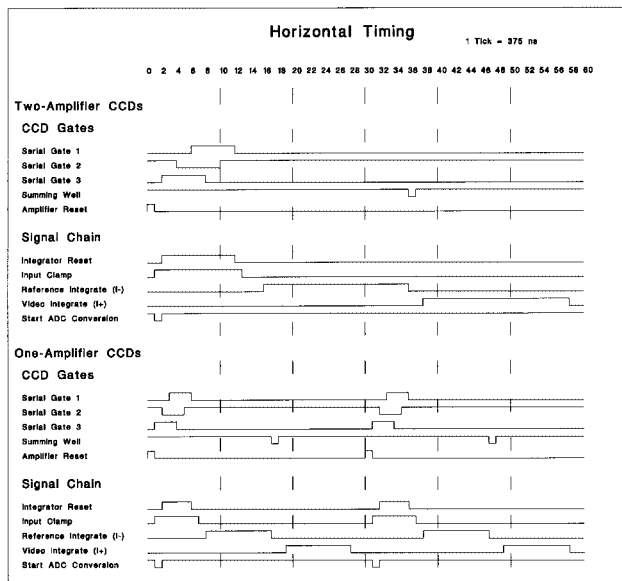


FIG. 26.—Timing diagram for the serial transfer of charge and the signal processing control for one- and two- amplifier CCDs.

(The fast channels run at $11.25 \mu\text{s}$ per pixel.) At $22.5 \mu\text{s}$ per pixel, the time for 1064 pixels is 23.94 ms, safely less than the 25.38 we have for this activity scanning at the sidereal rate. The 750 ns pixel clock for the normal chips and 375 ns one for the fast chips is derived from an 8 MHz master clock, which is needed by the A/D converters and the data transmitters.

The photometric CCDs are electrically connected to the preamp/clock-driver assembly via a 25-conductor Kapton

flexible printed circuit (FPC) with very thin copper conductors (see Fig. 27). This FPC terminates in a connector on the preamp board and is soldered to a BT-resin PC card that acts as a socket and fan-out board for the CCD on the other end. The astrometric chips, as discussed above, have no pins but are built with two FPCs as part of their structure. We have used BT-resin and polyimide boards throughout in the vacuum to avoid bromine contamination from the flame-proofing in ordinary FR4 (“G10”) fiberglass boards. This is standard practice in the high-energy physics community; we have no direct evidence of corrosive damage from vapor-phase bromine, but the dewars have a lot of electronics in a relatively small vacuum volume, and we chose to be cautious.

7.3. Preamps

The photometric preamps and the clock drivers are two small ($43 \text{ mm} \times 53 \text{ mm}$) piggyback BT-resin printed circuit cards using mixed through-hole (large hermetic tantalum electrolytics and the preamp operational amplifiers) and surface mount (everything else) technologies mounted on the inner wall of the dewar (Fig. 28). The preamps are made on board with 0.8 mm thick aluminum cores to which the preamp operational amplifiers are cemented using thermally conductive epoxy. The board mounts also contact this metal core and the walls of the dewar, forming a good thermal path from the amplifiers, which dissipate 140 mW each, to the dewar wall. They are electrically connected with a backplane, also made of BT-resin, which carries their signals to hermetic subminiature DB-37 connectors

The preamp circuit diagram is shown in Figure 29. The preamplifiers are coupled to the output of the CCDs using a fairly standard DC restoration circuit. The switches in U1

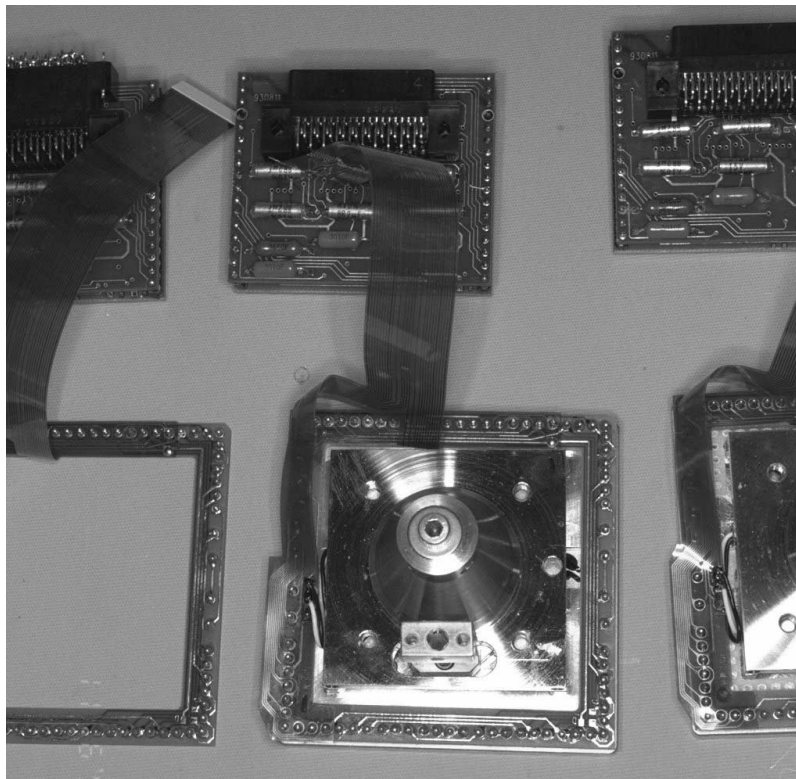


FIG. 27.—Photograph of the socket board assembly on a CCD mount and the preamp/clock-driver module, showing the FPC used to carry the CCD signals to the electronics.

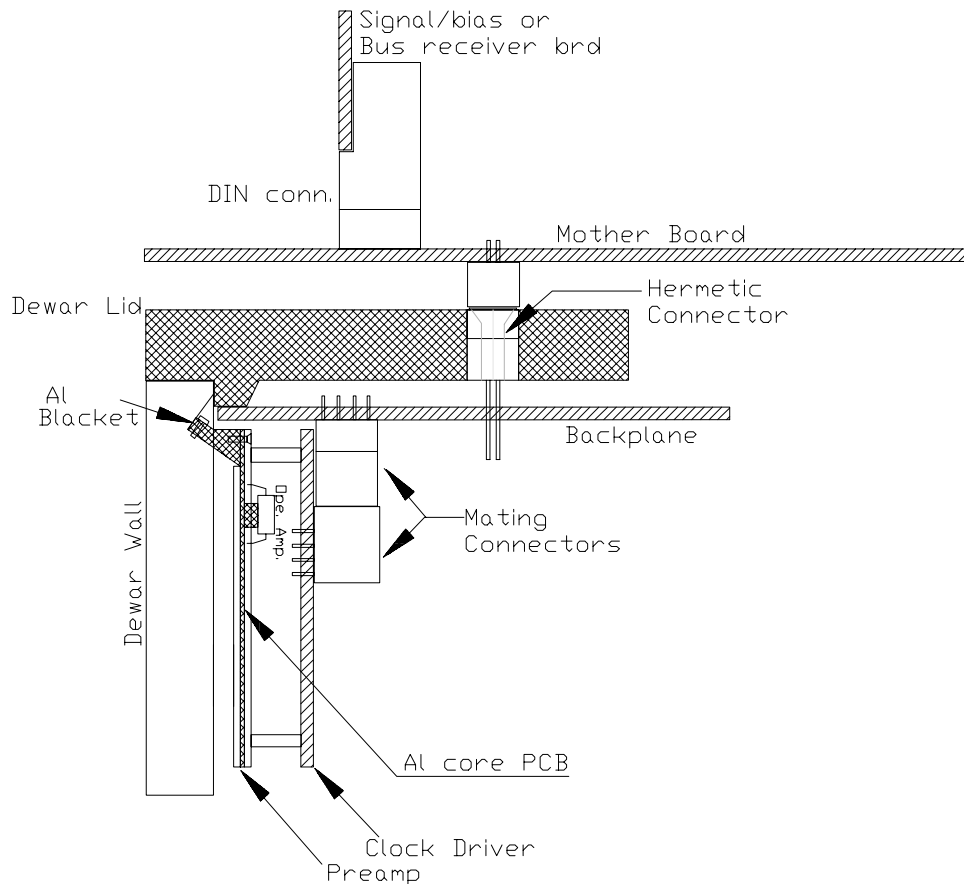


FIG. 28.—Sketch showing how a preamplifier is mounted to the dewar wall, how it plugs into connectors on the backplane board, and how the backplane board is connected to the motherboards on the dewar lids through the hermetic connectors. Note that it is the in-vacuum backplane board that is soldered to the connectors epoxied into the lid and is hence nonremovable; the motherboards on top can be removed with care.

are open during the video reference and sampling time, and are closed during serial transfer time by the logic signal IPC; the video level at sampling is thus set approximately to $I-TR/100$, the voltage at the bottoms of the 2 k Ω

resistors R6 and R7. The effective time constant for the circuit is the RC time constant $C1R6$ divided by the duty cycle of IPC, which is $4 \mu s/0.16$, $24 \mu s$, or a little longer than 1 pixel, but there are no AC coupling effects during the

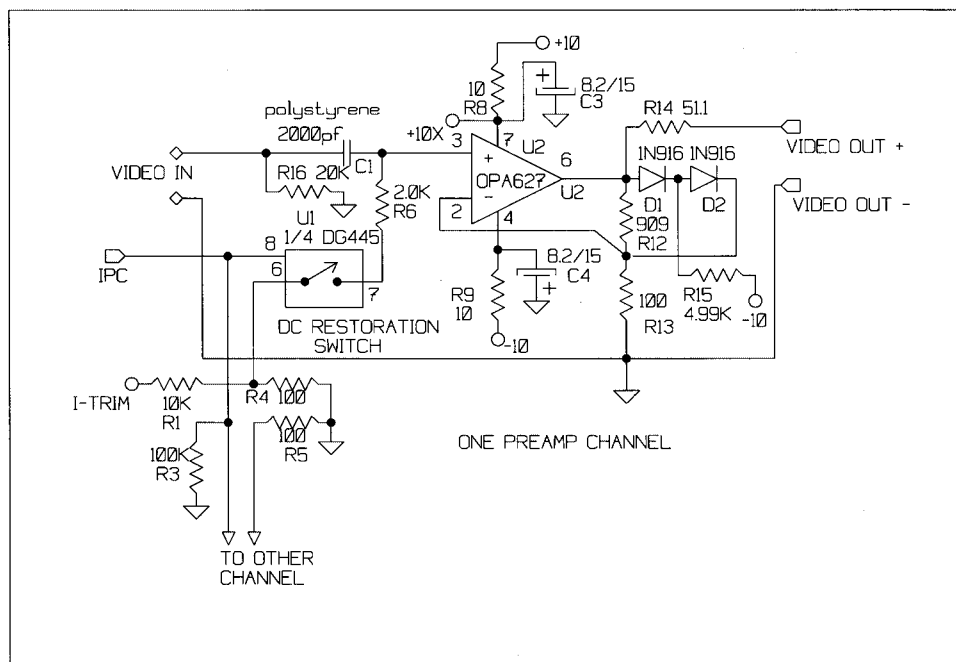


FIG. 29.—Schematic diagram of one channel of the preamplifier

period critical to the sampling of the video. The mean video level is supposed to be irrelevant in a double-correlated sampling system, but real systems are never perfectly balanced, and it is useful to maintain tight control over the sampling level; this circuit accomplishes this. The amplifier itself is a fairly fast monolithic op-amp with low-noise JFET inputs, the Burr-Brown OPA627, run with a noninverting gain of 10. The gain drops to unity for positive-going output signals (such as the reset pulse feedthrough) greater than two diode drops by virtue of the clamp circuit formed by D1 and D2. With the typical output gain of $1 \mu\text{V}$ per electron for our CCDs, the preamp saturates at a signal level of 600,000–700,000 e^- . With the typical input noise level of 3.5 $\text{nV Hz}^{-1/2}$ in the relevant frequency range, the preamp noise at our sampling rate is about $1 \mu\text{V}$, or about $1 e^-$.

7.4. Clock Drivers

The clock drivers are four CMOS DG403 analog switches with RC pulse-shaping circuitry on the inputs to the CCD gates (see Fig. 30). These switches, used basically as single-pole double-throw pairs, generate the CCD clocks by attaching a CCD gate to one or another DC rail voltage supply through suitable pulse-shaping RC circuits to limit the slew rates. The switches used, DG403's, have switching times of order 100 ns, which is sufficiently fast for this application. (The serial overlap is one master clock, 750 ns for the slow chips and 375 ns for the fast ones). Two switches are used for the parallel and transfer gates, and the other two for serial and summing well signals. The rail voltages ($\text{VP12}\pm$, $\text{VP3}\pm$, $\text{VT}\pm$, $\text{VS}\pm$, and $\text{VSW}\pm$) are generated

by DACs on the bias board. We have found that the CCDs are wonderfully insensitive to the operating voltages except near the inevitable instability thresholds, and we use voltages near the factory-recommended ones except for the parallel levels on the UV chips, which must be run at appreciably higher negative rails to avoid spurious charge, as remarked earlier. The VDD levels need to be trimmed for some chips as well to get the operating region safely away from incipient breakdown with attendant nonlinearity and high noise.

The astrometric preamps and clock drivers are substantially the same, but space constraints did not allow us to use the same boards; instead, the circuitry for 12 channels of video and the equivalent of six sets of clock drivers is built onto one piggyback pair of boards that run the whole length of the astrometric dewar and carry small adapter cards into which the astrometric CCD FPCs are plugged. Some modularity is sacrificed by this approach, but the handling and testing is really no more difficult than with the photometric design.

7.5. Signal Chain Board

The signal chain electronics and bias voltage supply are implemented in surface-mount technology on opposite sides of one small eight-layer 3U Eurocard. This board is mounted using a 96-pin DIN connector to a passive motherboard mounted to the outside of the dewar lid.

The signal chain board handles the double-slope integration of the CCD signal and its A/D conversion. It also contains RS-485 drivers to feed the serial A/D output to

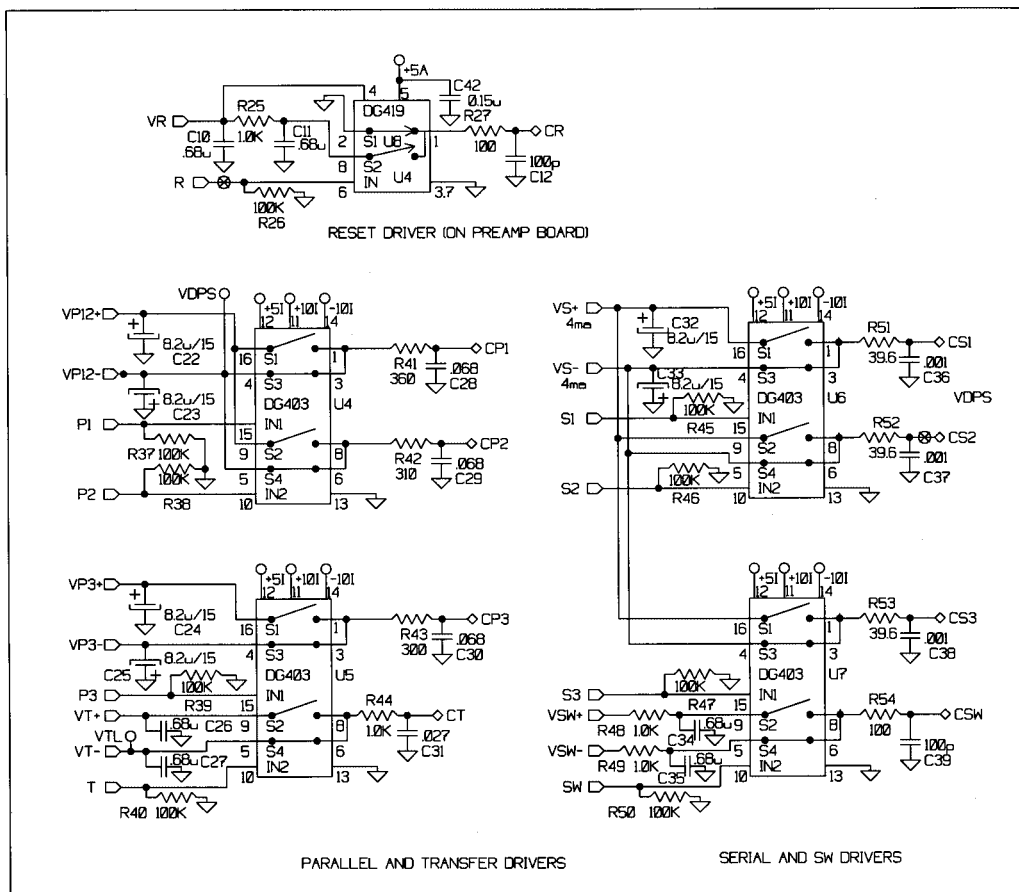


FIG. 30.—Schematic diagram of the clock driver circuitry

FOXI data transmitter. The circuitry, shown in Figure 31, consists of five blocks. U1 (differential amplifier, gain setting, and level shifting), U2 (inversion), and U4 (integration) are fast low-noise Burr-Brown OPA627's, and U3 is a CMOS DG445 switch, which handles the switching of the (inverted) reference level during the I⁻ period and the video during the I⁺ period into the input of the integrator and the reset of the integrator after the A/D acquisition.

The input amplifier U1 operates as a differential amplifier against the video input VID⁺ and VID⁻, which is preamp ground. The output impedance of the in-dewar preamplifier is 50 Ω from the op-amp and ground. The dewar amp output (VID⁺) is fed to the noninverting input of U1. The gain of the amplifier is near unity, but is trimmed by adjusting R5 and R6 for the output gain of each CCD and to set the desired conversion gain (e^- ADU⁻¹). This is set nominally at 2 for the u' band, 5 for g' , and 6 for the others. The output level of the CCD at about 1 μ V per electron results in about a 4 V negative signal from the preamp at saturation, about 400,000 e^- .

The signal chain runs with a virtual ground at the ADC reference level, VREF⁻, -4.5 V, to accommodate the ± 4.5 V range of the ADC, with zero output at -4.5 V. U1 performs the level shift using a current injection from the VREF2 (9 V) signal derived from the ADC reference. The video level at the output of U1 goes from -4.5 V at zero signal to (nominally) -9 V at saturation. Gains and resistor values are chosen so that the noise contributed by all of the

circuitry here is small compared with the input noise of the preamp.

The output of U1 goes to the input of U2, a unity-gain inverter, and through the I⁺ switch through a 2K resistor to the input of U4, the integrator. The reference voltage of for the integrator is VREF⁻, which is the zero level of the ADC, and the output of U2 is used to generate the inverted video signal for the reference level. Thus the integrator output goes from -4.5 V positive; the effective gain of the integrator is set by the 2K input resistors, the integration capacitor C12, and the integration time, nominally 7.5 μ s for the slow chips and 3.75 μ s for the fast ones. This gain, just $t_{\text{int}}/(R_{\text{in}}C_{\text{int}})$, is set nominally to a value near 2 with the choice of 1800 pF for C12 for the slow chips and 910 pF for the fast ones. Thus the nominal saturation signal of -4.5 V at the input results in a level presented to the A/D of +4.5 V, its saturation level. One ADU is 130 μ V; the net noise of the circuitry on this board through the double-correlated sampling including Johnson noise and amplifier input noise is about 23 μ V, much less than 1 ADU.

There is overload protection in the input to the integrator: the 2K input resistor (for the noninverting signal) is split into two 1K parts, R14 and R23, and the junction is clamped to a low-impedance VREFD⁻ level by the combination of a Schottky (D1) and an integrated 2.5 V Zener (D2) and is prevented from going more negative than -4.5 - 2.5 = -7.0 V, which would arise from a -5 V input signal. The input resistor is not connected to the input of the integrator op-amp except during the video I⁺ phase, and

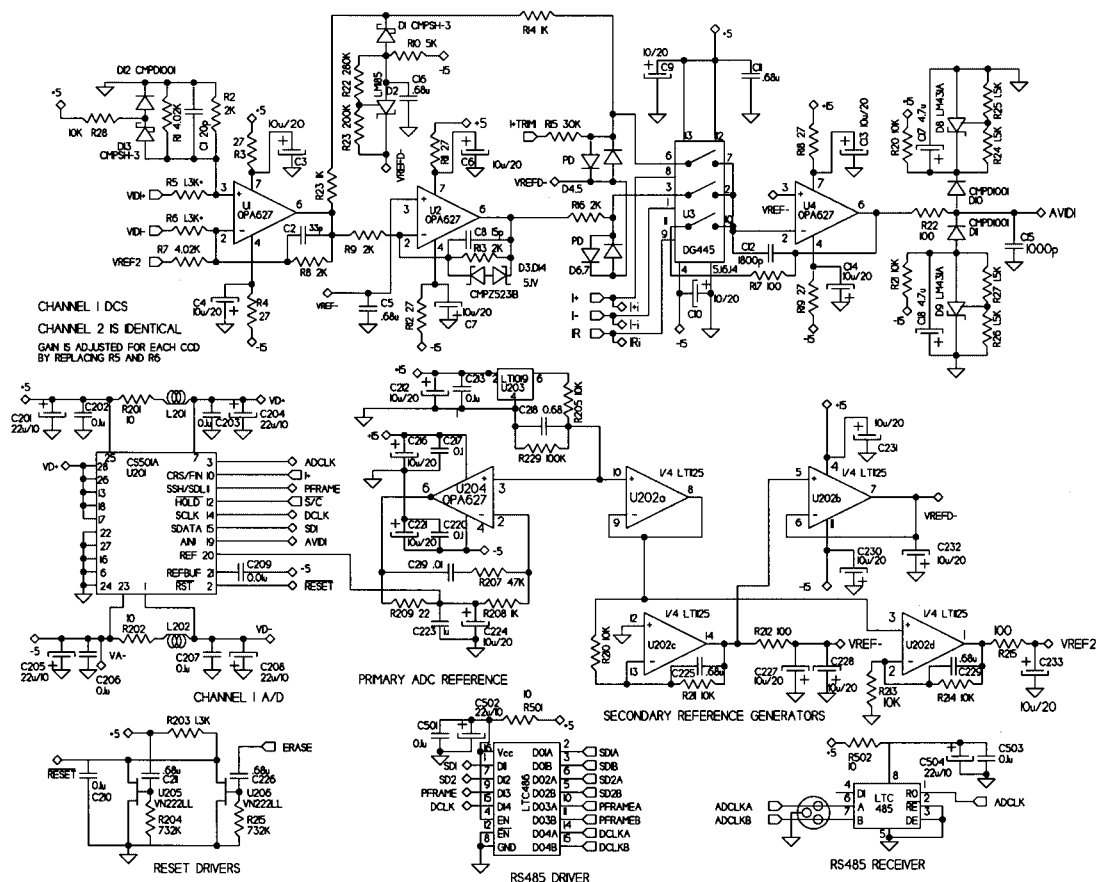


FIG. 31.—Schematic diagram of the signal chain, showing the reference voltage generators and one channel of signal processing and analog-to-digital conversion.

the integrator end is kept from moving very far from ground and thereby charging stray capacitance by the back-to-back low-leakage junction diodes (we use the base-collector diodes of signal transistors) at the input to the switch (D6, D7). CCDs typically exhibit considerable capacitive cross talk from the gate (SW), which dumps the video charge onto the output node, and even if the SW is pulsed (which we do) to dump the charge the cancellation is not perfect. This signal needs to be subtracted from the video signal. This is accomplished by an adjustable voltage (I + TRIM) across the 20K resistor R15. The input to this resistor is 10 times less noise sensitive than the input to the integrator, so can easily tolerate $\approx 100 \text{ nV Hz}^{-1/2}$ of noise and still contribute negligibly.

In the double-slope integration sampling, the video level is subtracted from a reference level established just prior to the video dump (I—). The simplest way to do this is to have the integrator integrate the negative CCD output waveform for the same time as the positive one is integrated for the video. The negative waveform is generated by the inverter U2, which inverts the output of U1 relative to the -4.5 V reference level. It is protected by a clamp consisting of a signal diode and a 5.1 V Zener against overload associated with extreme saturation. This clamp was originally implemented with back-to-back Zeners, which leaked so badly and exhibited so much hysteresis that serious instability was introduced into the background level; considerable sleuthing was required to find the problem, so be warned. (It may well be that this is a known problem, but it was certainly not known to us.) The output of this stage is connected to the integrator input also through a 2K resistor (R16) and another section of the switch.

The I— switch connects the output of the inverter U2 to the integrator during the $7.5 \mu\text{s}$ video sampling interval I—. The switch is opened and one clock cycle elapses for the video to settle to its final value before the $7.5 \mu\text{s}$ video sampling interval I+ is initiated, during which the output of the input amplifier U1 is connected to the integrator. When this period ends, the I+ switch is opened, and the double-slope sampling video level is held on the output of the integrator. One clock cycle elapses before the conversion is begun.

Our A/D converter is Crystal Semiconductor CS5101A, which converts to 16 bits in $8 \mu\text{s}$ with an 8 MHz input clock and which has internal calibration circuitry that keeps the internal accuracy at $\pm 1/4 \text{ LSB}$. It requires an external 4.5 V reference and an external clock of 8.0 MHz . The timing diagram is shown in Figure 26. The reference input must be a stable low-impedance source. It is implemented as an OPA627 voltage follower (U102) operating from an LT1019 reference, which also feeds the amplifiers in a quad LT1125 to generate the other reference voltages, $\text{VREF2} = 9.0 \text{ V}$, $\text{VREFD} = -4.5 \text{ V}$, and the critical $\text{VREF} = -4.5 \text{ V}$, through U202a–d. The OPA627 has a $4.5 \text{ nV Hz}^{-1/2}$ maximum input noise and is connected to the reference input of the amplifier via a filter consisting of a 220Ω resistor and $11 \mu\text{F}$ (C227 and C228) of filter capacitance, the DC loop being closed around the filter. The noise bandwidth is less than 1 kHz , and the noise injected into the reference input is less than $1 \mu\text{V}$.

There is some concern about whether 16 bits is enough, but the problem is not severe. In the g' , r' , i' , and z' bands the sky levels are such that digitizing at roughly $6e^- \text{ ADU}^{-1}$ results in a step that is small compared with the standard

deviation in the background, and accommodates with 16 bits the nominal 300,000 electron full well of the device. In the u' chips the situation is not quite so good. The sky in each chip is only of order $60 e^-$, and the noise with $5 e^-$ read noise per chip is about $9 e^-$. If we demand that we digitize at least two levels per unit sigma, this will result in a digital full well of somewhat less than the physical full well of the CCD. This is not a serious problem, however, since the fluxes and efficiencies are such that no object that does not saturate in one of the other bands is likely to overflow the u' A/D. In practice, we also back off a bit for the g' chips to an inverse gain of $5 e^- \text{ ADU}^{-1}$.

In addition to the problem with the Zener clamp on the inverting amplifier, we had another serious problem with this board that manifested itself in rather troublesome levels of $1/f$ noise in the video. This was not present in the test data taken with much older electronics, so the CCDs themselves seemed to be absolved. The culprits, again after much investigation, turned out to be resistors. We had been careful to use metal-film resistors in all the gain-determining places on the boards but had used ordinary precision thick-film surface-mount resistors elsewhere. These turn out to have completely unacceptable current noise in 16-bit systems; replacing the feedback components and voltage divider resistors in the reference circuit with metal-film ones (which fortunately can be had in the small 0603 SMT format for which the boards were designed) finally solved the problem. If we had the boards to redo from scratch, we would use metal-film resistors everywhere.

The signal chain board dissipates about 1.5 W ; there is one per chip in the photometric dewars, and one per two devices (all single-amplifier) in the astrometric dewars.

7.6. Serial Shift Register and FOXI Board

The Crystal A/Ds have a serial output, which is fed (again over RS-485) to a pair of small cards mounted piggyback on the dewars whose function is to format the data and transmit it over fiber to the data system in the operations building. In the photometric dewars, there is typically a mixture of single- and two-amplifier chips, and the fast serial data from the single-amplifier devices must be formatted to look like two streams so that it is compatible in timing and data rate with the output of the normal chips. This is accomplished by the serial shift register card, which processes the single-amplifier data and passes it on along with the unprocessed two-amplifier data to the second card, which carries the fiber transmitter.

The FOXI card carries a Xilinx programmable logic array that can receive up to six double-amplifier serial data streams with their associated clocks, produces sequential parallel byte-wide data, and sends it to a FOXI fiber transmitter, which reserializes the data at about 100 MHz and drives the data fiber.

The astrometric dewars have two FOXI boards with slightly different firmware and no serial shift-register boards; though there are only 12 single-amp data channels, the data rates are such that two transmitter boards are required.

7.7. Bias Board

The bias board generates the DC voltages necessary for operation of CCDs and their associated linear support electronics (except the ADC and associated signal chain references, which are independent; there is no good reason for

this, and it may well have been a mistake; it would probably have been better to derive all voltages from the ADC reference). In addition, there are two more functions of the bias board, viz., it acts as an analog multiplexer to allow measurement of those voltages by a remote ADC incorporated into the camera microprocessor, and it provides temperature control for CCDs. The circuitry is shown in Figure 32.

The CCD voltages and the voltage required to trim the dual-slope circuitry are generated by a set of three octal 8-bit DACs, Maxim 528's, for each chip. These voltages provide rail potentials for CCD gates that have small (a few tens of pF) capacitances (T, SW, R) or are nearly constant current loads (VDD). Simple filters and slow operational amplifiers suffice to keep the voltage nearly constant. For instance, for the transfer gate (T) the gate capacitance is ≈ 100 pF and switched every 40 ms through a range of about 10 V. At every transition the charge on the filter cap changes by 1000 pC, so the voltage across 11 μ F of filters drop by 100 μ V. With a 200 Ω series resistor, the voltage is reestablished with a time constant of about 2 ms, sufficiently short compared to the line time.

Another example of a low-capacitance gate but one with very high sensitivity to voltage errors is the summing well. It has 10 pF capacitance and switched every 22.5 μ s. It has a two-stage passive filter with a time constant of about 3 ms, and the average current 4.2 μ A. The total filter resistance is 1200 Ω , so the drop is 5 μ V. The summing well is an especially sensitive case for CCDs, since feedthrough from the summing well transition emerges directly in the video

output: while all other clock feedthrough is differentiated by the double slope sampling, the SW clock dumps the charge directly on the output diffusion. This feedthrough amounts to a signal corresponding to 15,000 e^- of image charge. If therefore one wishes a system controlled to $1e^-$, it is necessary to keep the rail voltage of the SW switch stable to of the order of 1/15,000, or 0.8 mV for the switching range of 12 V. The voltage drop of our system is 5 mV, but the summing well runs all the time, so it is stable to the order of resistor stability, clock stability, and reference stability; there are no timing glitches in the reading sequence of the CCD that interrupt it. In practice, we pulse the summing well to dump the charge, which to some approximation cancels the feedthrough, but the stability requirements still apply.

The serial drives have about 1000 pF capacitance per phase with another 1000 pF buffer on the dewar board, and each phase is switched every 22.5 μ s, with a given transition followed by another in 1.5 μ s. The switching time occupies 5.25 μ s of the 22.5 μ s serial read time. The switching amplitude is typically 12 V, and the switching current about 3 mA. With the individual gate time constant 120 ns, the instantaneous switching currents are large, about 200 mA. At each switching transition 25 nC of charge is removed from the 22 μ F filters, and so the voltage changes by about 1 mV. If we must recover from this by the next transition from the same rail 1.5 μ s later, it would require a current from the regulator of about 16 mA with response time shorter than 2 μ s. This could be done with high-speed op-amps, but there is really no need to respond this fast: the three transitions

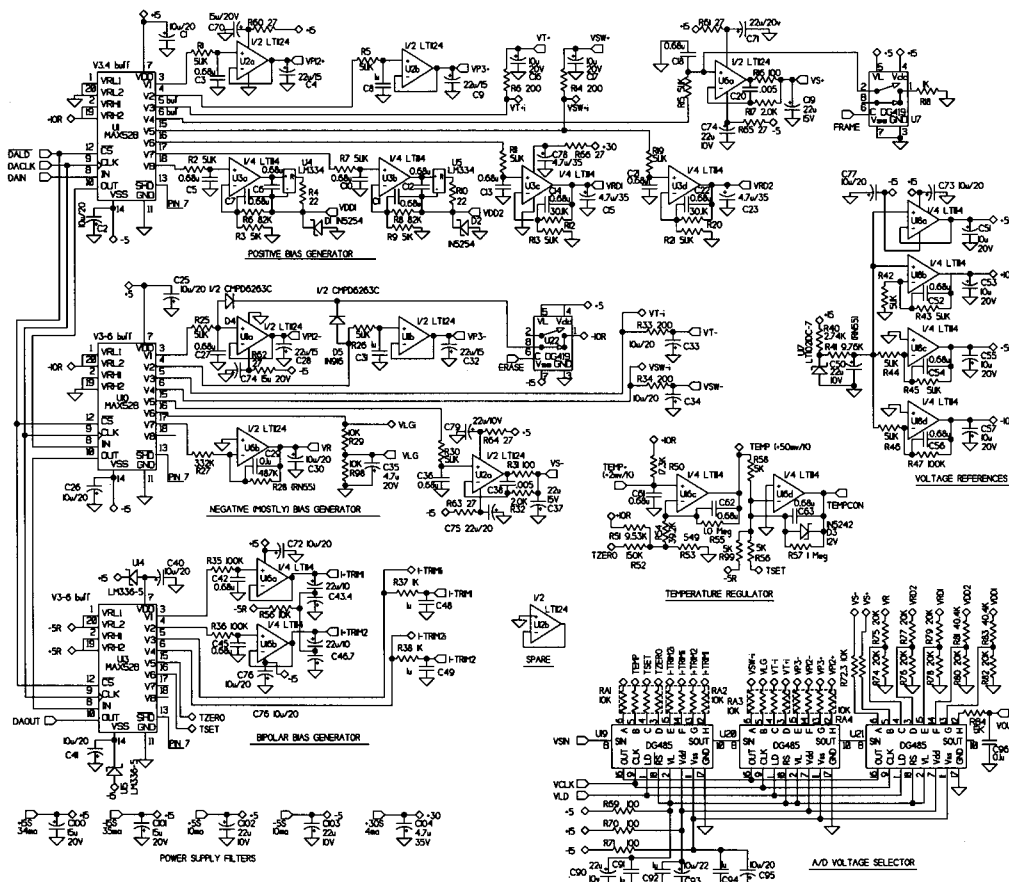


FIG. 32.—Schematic diagram of the bias board

from one rail changes the voltage by only 3 mV in 6 μ s, tiny compared with the total swing and small enough to keep the op-amp out of slew, and the regulator then has 14 μ s to recover.

The parallel drives pose a similar problem. The parallel gate capacitance is very high, 80 nF per phase. There is 70 nF of buffer on the dewar board, and so the total switched capacitance is about 150 nF. Each parallel clock is 8 pixels long, or 180 μ s. The waveform is controlled by the clock capacitance, buffer, and an external series RC circuit (400 Ω , 40–100 Ω from effective gate resistance and 300–360 Ω of serial buffer resistance). With a voltage swing of 12 V, the peak current is about 30 mA. The switch transitions to a given rail are about 360 μ s, and two transitions follow by 37 ms of silence, during which the parallel voltages must be very stable. The gates cover so much of the device that potential changes show up in the output as gain changes in the output amplifier. Here we have elected to allow the regulator op-amps to go nonlinear. A transition subtracts about 1.8 μ C of charge from the 22 μ F filters with a step of about 82 mV. The regulators, U2 and U11, are directly connected to the filters. This voltage step drives the op-amps into current slew, and they deliver their short-circuit current, 25 mA for LT1124, until the deficit is made up about 60 μ s after. There is a glitch of about 10 μ s until the amplifier settles, but the voltage is well stabilized before the next transition occurs and very well settled after the last transition in the 360 μ s before the serial readout starts.

The regulators, U3, for VDD1 and VDD2 used in the output amplifier incorporate some current protection. The LM334 current sources act like forward-biased diodes so long as the current through them is less than their set currents, 3 mA, but go to a very high impedance state as the current approaches the set value. The nominal output FET drain current is 1 mA, and the op-amp divider and measurement divider require another 0.7 mA. For these currents the resistance of LM334 is of the order of 100 Ω ; the high-frequency impedance is reduced by the 0.68 μ F shunt capacitor. Another 0.68 μ F shunt to the inverting input limits the noise output to input voltage noise of the op-amp, which is 18 nV Hz^{-1/2}.

The DACs have serial input, and all the converters in the system are daisy-chained to be set up with one very long serial word. The output voltages are sampled and placed on an output bus for measurement with a set of serial-input eight-position analog switches, U19, U20, and U21. Twenty-three of the switches are used for voltages to be monitored, and the last to connect or disconnect the selected voltage from the output line from the board. This last enables a crude bus architecture in which one line going to the ADC on the executive microprocessor can monitor all the voltages in the camera. The steering logic is contained on the bus receiver board.

The default voltage information is stored in EPROMs in the controller micro but can be modified in software.

The voltages generated by the DACs are monitored by a 10-bit ADC that is built into the Hitachi H8 Forth microcontroller that runs the camera. The voltages are switched one by one onto a dewar-wide voltage bus by the DG486 serial-input octal switch arrays and then buffered and switched onto a camera-wide bus by circuitry on each dewar's bus receiver board. The time constants are such that the camera can measure accurately one voltage per five line times during the operation, with the setup happening

during a 900 μ s parallel transfer time. Thus the system can run gathering one voltage value per 130 ms. There are 24 voltages for each of 30 photometric and 12 pairs of astrometric CCDs, so the process requires about 130 s for one cycle. For all voltages which have passive filters the measurements are taken ahead of the filters to avoid any disturbances to the operating voltages.

The bias board also contains the temperature regulator for the chip it serves. The CCD temperature sensors are platinum resistors that have a resistance of 1.00 k Ω at 0°C. They have a characteristic temperature dependence of resistance that is almost proportional to the absolute temperature. The slight nonlinearity in this relationship can be compensated approximately by feeding the platinum resistor with a stable voltage source through a suitably chosen (relatively large) stable resistor and using the voltage across the platinum resistor as the temperature signal. This resistor is the 17.3K unit R50. The first stage of the regulator amplifier U16cd is a gain 25 noninverting amplifier, whose output is +50 mV °C⁻¹ and is biased so that its output is zero at 0°C. The zero can be trimmed with the DAC-generated level TZERO. The output is compared with another level, TSET, by the very high-gain second stage, which drives the emitter-follower pass transistors located on the power distribution board that supplies current to the makeup heaters on the CCDs. TSET determines the threshold temperature at which the resistors turn on, and the gain is such that the transition from full OFF to full ON is over a range of about 1°. Not having an abrupt transition appears to be necessary to avoid hunting in the temperature servo, and the accuracy and stability with this gain is satisfactory.

There is one of these cards per chip on the photometric camera. Some of these cards, associated with the single-amplifier chips, use only one signal channel, but all the cards are identical except for the input resistors that are used to trim the gains to match the individual output amplifier gains for each CCD, and the integrator capacitor, which is a different value for the fast single-amplifier circuitry. Thus each photometric dewar contains five of these cards, plus one card that is basically a bus receiver for the clock signals described below; the astrometrics employ six plus a bus receiver. All astrometric chips run with only one amplifier (they are front-side devices and will all run fast) to save cards and space, and so we run two chips with each signal chain bias card—the performance penalty is negligible, and the astrometric chips are sufficiently homogeneous in electrical (and other) properties that the loss of ability to generate voltages tailored to a specific CCD is of no concern; in any case, we retain the ability to set the output drain voltage and reference voltage for each chip.

Each bias board consumes altogether 1.3 W, of which about 0.5 W is associated with DACs. Since the bias board is physically associated with a signal chain board, each serves one device in the photometric dewars and two in the astrometric.

7.8. Bus Receiver

The bus receiver is a modified small Eurocard that converts the RS-485 timing signals on the 100-pin ribbon cable bus to CMOS logic levels, which are fed to the rest of the camera circuitry. It also contains a shift register and circuitry that decodes the last byte of the monitor voltage-selection word. The voltage-selection word is 4 bytes long,

the first three of which have one bit set among them to select the voltage one wishes to connect to the executive micro's ADC and the last of which contains the dewar and CCD address. The dewar ID is set with jumpers on the board, and if the dewar address agrees with the dewar ID, the output of the buffer amplifier U12 is connected to the bus. The CCD address is decoded and translated into an enable signal for each CCD's signal/bias board, which routes the serial selection bits to the relevant dewar via the multiplexer U9. The switches on the bias boards come up with all switches cleared; the procedure is then to send a setting word of all zeros to the last dewar/CCD addressed to turn off the switch for the last voltage measured, send a byte to connect the new one, and send a word to connect the desired voltage for that dewar/CCD. When it has been measured, the sequence is repeated. Figure 33 shows the circuitry.

7.9. Camera Controller

The camera controller is built around two Hitachi H8/532 FORTH microprocessors from Triangle Data Services. One, the *executive micro*, manages the housekeeping and communications, and the other, the *phase micro*, generates the CCD clock waveforms. There is also support circuitry required to implement the various housekeeping functions and bus interfaces. Each micro is mounted piggy-back on a small Eurocard and there are, in addition, five other Eurocards that are part of the controller system: a *bus driver*, which drives the RS-485 CCD timing bus and implements the check byte comparator for the long serial DAC-setting word; a *star driver*, which generates the master 8

MHz clock, derives the 2.3333 MHz pixel clock from it, and has the 24 RS-485 drivers to send the master clock to all the dewars and all the FOXI transmitters; an *LN2 board*, which implements all the autofill logic for the dewars; a *pressure board*, an electropneumatic nightmare that handles the bellows pressure/vacuum for the Tbar latches, monitors those pressures, and handles the interface to the telescope control system that commands the latches; and a *temperature/shutter board*, which controls the electropneumatic shutters and buffers all the various other pressures, temperatures, and miscellaneous states monitored by the executive micro. These include air temperatures in the camera and in the power supplies, the temperature of the steel main support ring for the camera, pressures in the intermediate LN2 supply dewars, and the state of a flow switch in the water/glycol cooling system for the electronics. The analog signals are multiplexed by this card to send to the executive micro ADC, and the digital ones buffered for sending to a port on that micro.

The phase micro generates the CCD clocks from programs stored in EPROMs and controlled by an Hitachi H8/523 FORTH microcontroller. One controller runs the entire camera; all CCDs are clocked synchronously with identical clocking waveforms (though there are two sets of serial waveforms for the "fast" and "slow" chips.) The system diagram is shown in Figure 34.

The executive micro has an (optical fiber) RS232 connection that is one of the two communications connections to the outside world. It controls the phase micro with another RS-232 connection. The Hitachi microprocessor has an integral four-channel 10-bit A/D that is used to measure the

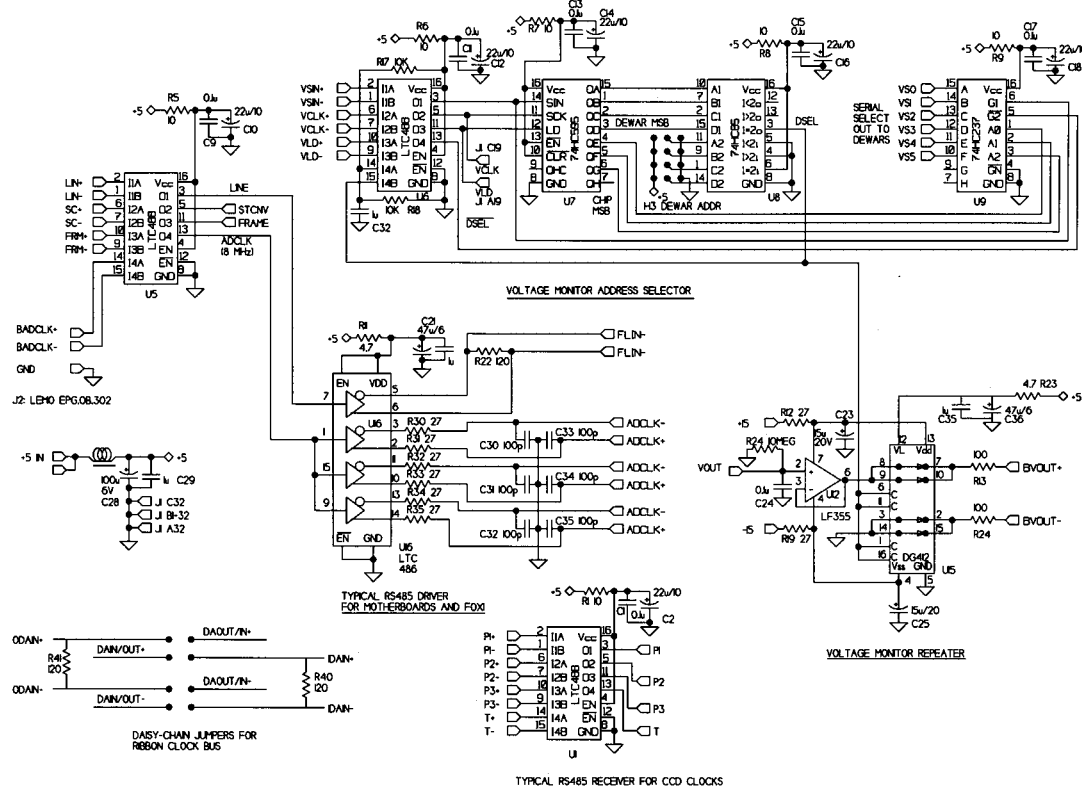


FIG. 33.—Schematic diagram of representative circuits on the bus receiver board, detailing the voltage monitor selection and monitoring circuitry and giving examples of the RS-485 handling. The long serial chain for setting the bias DACs is handled using the ribbon cable clock bus by alternately cutting the conductors on the extreme edges of the cable and setting the jumpers detailed here accordingly.

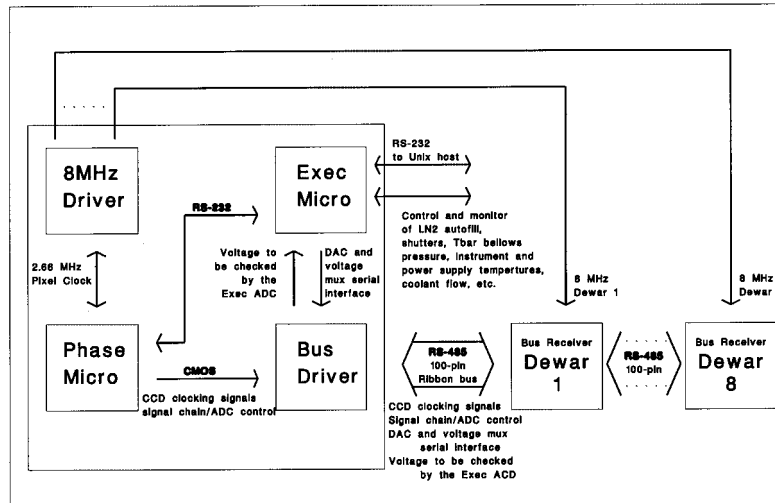


FIG. 34.—Conceptual diagram of the camera controller showing the major signal paths

CCD voltages placed on the voltage bus on one channel and to measure, among other things, the pressures and temperatures in the housekeeping data with another. The CCD voltages (the CCD temperatures are part of this set) are measured on a round-robin basis as described above. The DAC setting requires a word a little more than 10,000 bits long, which has a leading check-byte that is received back at the bus driver after making the entire rounds. The clock is slow, 10 kHz, and so the setup time is about 1 s. All signals are sent from the bus driver by balanced RS-485 transmitters and received at each dewar by complementary receivers. All signals except the 8 MHz master clock are carried on a 100-conductor ribbon cable bus; each 8 MHz line, one to each dewar and one to each FOXI card, has a dedicated shielded twisted pair cable from the star driver.

The executive has considerable flexibility in controlling the chips; we implement on-chip binning both horizontally and vertically (independently) and allow some control of the sampling interval. Several clocking schemes are stored in ROM, including one in which the video switch I+ is never turned on to allow setting the I-TRM video levels, one in which there is no data sampling to allow quick access to any row in the chip for partial readout, etc.

7.10. The Power System

Each dewar has its own power supply, each of which is implemented using small encapsulated linear (dictated by noise considerations) supplies on a single 20×25 cm 3 mm thick printed circuit card. Each supply carries a fairly sophisticated monitoring and shutdown system mounted on a separate smaller PC card. A set of LEDs and a digital meter allows one to read any selected voltage, display the status of all voltages (in-range or out, selected or not for the meter). A sufficiently out-of-range voltage shuts down the whole supply, but the culprit is still displayed on the status display. An error insufficient to cause alarm but still out-of-spec (the thresholds are typically set at 3% and 5% of the desired value) illuminates the out-of-range LED for that voltage but does not cause a shutdown; in this way drifts can often be caught before shutdown occurs. The power supply boards are mounted in their own enclosures mounted on a structure called the *saddle* (see § 8) which stays with but is not mechanically tied to the camera.

The DC power lines go from the supply chassis through the camera enclosure and then through DB-25 connectors on the individual dewars to a *power distribution board*. This is a small board that carries filters for each supply, regulators to make the voltages used by the preamps (± 10 V, 5 V), the pass transistors for the CCD heaters, and the amplifier for the platinum resistor temperature sensor on the LN2 container. Power for the FOXI boards is carried directly to them and is not, for noise reasons, routed through the dewar electronics.

8. THE OVERALL STRUCTURE OF THE CAMERA AND ITS UTILITY SUPPORT

The fused quartz distortion corrector provides the metering structure for the detectors and allows us to keep the relative geometry within the focal plane extremely stable, but it is, of course, necessary to hold the corrector stably with respect to the telescope as well. This is complicated by the fact that the corrector has a very small expansion coefficient, more than an order of magnitude smaller than the steel structure of the telescope. We decided to take up the expansion difference in the design of the corrector cell, and to build the main camera structure of steel.

The corrector is mounted in a thin machined steel cylindrical cell that is sliced vertically to form 30 “leaves” that are bonded to the circumference of the corrector. These leaves are quite flexible in the radial direction owing to their small thickness (1/8 inch) but very stiff in shear tangentially to the corrector. This ring is, in turn, bolted to a very stiff steel ring girder that forms the main structural element of the camera (see Fig. 35).

The ring girder, welded from two short $\frac{1}{4}$ inch steel tubes and two $\frac{3}{8}$ inch steel rings and then machined as one piece, has an approximately 3×7 inch cross section and, with the cell, weighs about 200 pounds. This ring carries all the mass associated with the camera except the power supplies and the intermediate LN2 dewars; this “camera proper” mass is about 700 pounds. The ring is mounted to the instrument rotator bearing on the telescope on a fairly conventional classical trefoil kinematic mount, implemented in this case as three sets of double roller bearings allowing free radial movement (see Fig. 36). Each leaf of the trefoil utilizes eight rollers, four each defining a surface parallel to the radius in

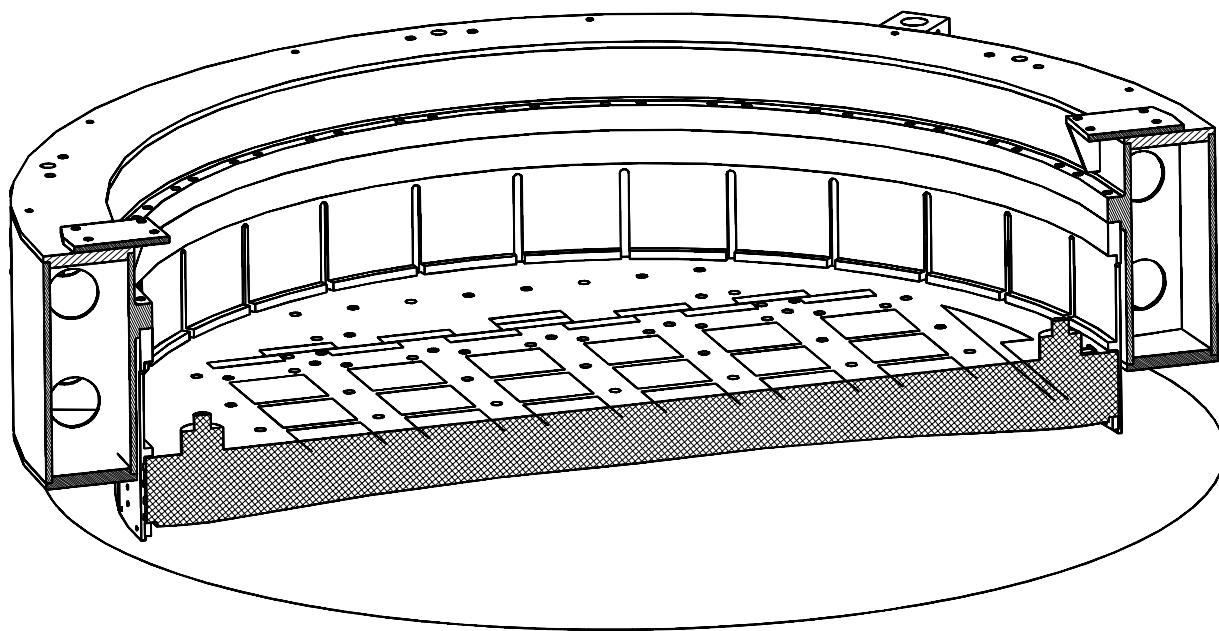


FIG. 35.—Pro/Engineer cutaway of the main camera ring and corrector in its cell. The corrector is bonded into the thin-wall slotted steel cell, and bending of the “leaves” in the cell takes up the expansion difference between the steel and quartz.

one direction and 45° from the optical axis in the other. The kinematic mount is maintained in contact by three pneumatically actuated sprung latches, one associated with each leaf, each exerting a force of 700 pounds along the axis of the camera. This arrangement, combined with the leaved cell for the corrector, results in deflections under gravity that are very small and are furthermore very well behaved. The corrector center moves by about $5\ \mu\text{m}$ with respect to the fixed (telescope) members of the kinematic mounts from the zenith to the horizon, and that deflection is to high accuracy in the direction of the local gravity vector, independent of the rotational orientation of the kinematic mount, and is accompanied by completely negligible twist. The focus change is of order $2\ \mu\text{m}$. Both the focus deflection and the lateral deflection are completely negligible compared to expected deflection effects in the telescope structure and optics.

A pneumatically operated shutter assembly is attached to the top of the leaved corrector cell (Fig. 37). This utilizes 16 hinged doors, two associated with each dewar. The opening/closing times are of the order of 1 s, and it is intended primarily as a light seal, though crudely timed exposures can be made with it.

The camera is covered on top by a welded aluminum ring structure attached to the main ring girder, which serves to carry a dust cover when the camera is stowed and offers protection to the shutter assembly and corrector. Flexible rubber gaskets seal this cover to the inside of the instrument rotator when the camera is on the telescope. This seal keeps stray light out and also serves as a crude seal for a continuous nitrogen purge between the camera and the Gascoigne corrector of the telescope, about 70 cm above the distortion corrector. This purge is primarily to keep the optics clean.

A similar shroud is attached to the bottom. This is a considerably more complex structure. It carries all the connectors for power and signals, the cooling system for the electronics, and the LN₂ plumbing, which carries nitrogen from the intermediate dewars to the camera dewars and the

vent gas from the camera dewars to the solenoid vent valves; these valves are also mounted on this ring. A conical cover is attached to the bottom of the ring and serves as a light-tight cover for the camera. The dewars are surrounded on the corrector by a machined aluminum light shield as well, the intent being that the space behind the corrector which the dewars occupy should be reasonably sealed both to gas and light, and certainly that no light from the telescope enclosure should reach the focal plane from the dewar side of the corrector. This space is also kept under nitrogen purge, the primary objective here being to keep the dewars and their associated cryogenic lines dry. A photograph of the dewars with their associated liquid nitrogen plumbing and cooling vent tubes in the rear shroud before all the wiring and insulation were added is shown in Figure 38.

The dewar power supply boards are distributed in two almost identical large chasses, each carrying four dewar supplies and an “auxiliary” supply for the microprocessors and associated control electronics, the fans, and the valves. These are mounted along with the two 10 liter intermediate LN₂ dewars on an aluminum saddle (Fig. 39) that always accompanies the camera but is mounted to the telescope independently of it. This is in order that the kinematic mount carries only what it must, and that as symmetric and stiff as possible. The saddle assembly with power supplies and dewars weighs about 300 pounds, so the camera assembly all together weighs just over 1000 pounds.

The camera and saddle are carried when off the telescope on a special cart/handling fixture (the ops cart), which rolls on fixed rails between the telescope and the “doghouse,” a sealed enclosure that houses the camera when it is not in use. A photograph of the camera alone on the telescope with the saddle on the ops cart in the doghouse is shown in Figure 40. This unusual configuration is the one used to transfer the camera to the service cart (see below) for transport for servicing. AC power, gas utilities, glycol/water coolant, signal fibers, and liquid nitrogen are carried to the camera on an umbilical that always remains attached to the

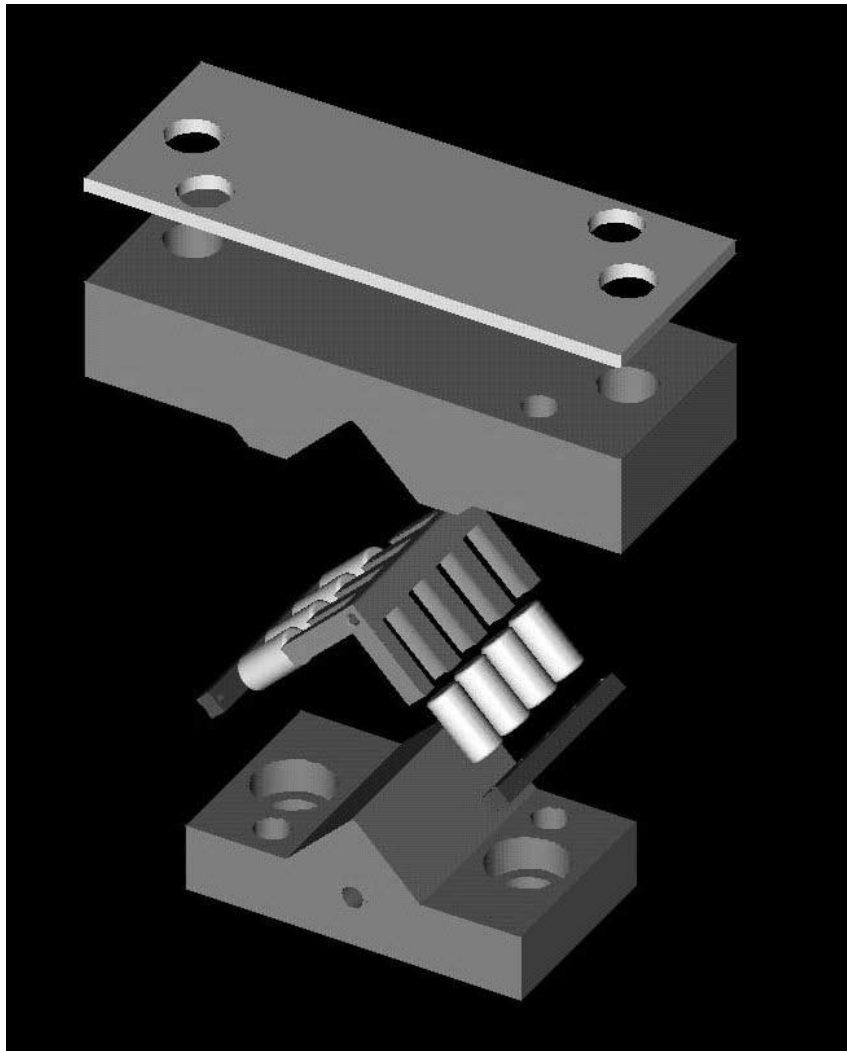


FIG. 36.—Pro/Engineer exploded view of one of the three kinematic mounts that mate the camera to the telescope. The male and female blocks are hardened EDM-cut steel. The spacer shown below the female block, which is the side mounted to the camera, is made of Ultem 2300 resin, a strong plastic that has an expansion coefficient well-matched to steel and serves as part of a system that keeps the camera electrically isolated from the telescope structure.



FIG. 37.—Photograph of the top shroud of the camera through the opening in which can be seen the shutter assembly, with the “French door” photometric shutters. Less obvious at the top are the astrometric shutter doors, also shown open in this photograph.

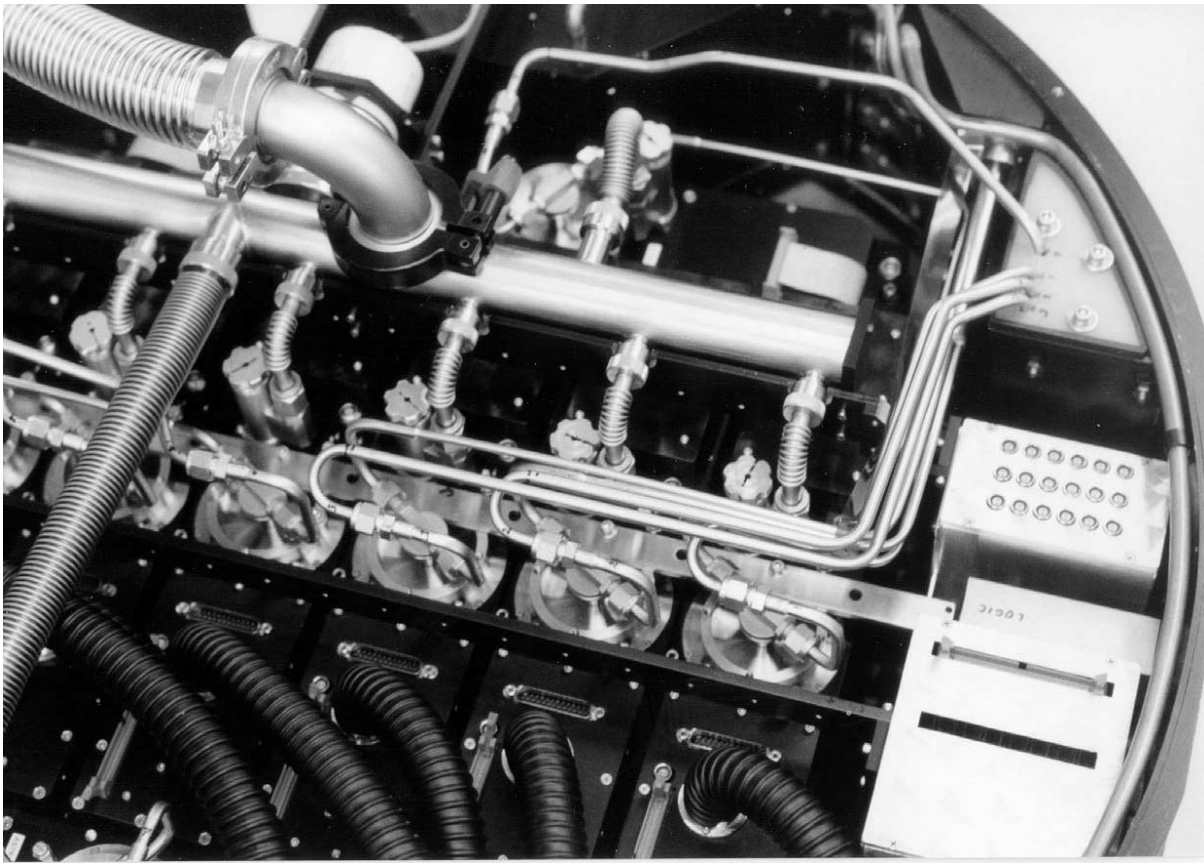


FIG. 38.—Photograph of the camera during assembly, showing the microprocessor box at the extreme right, the photometric dewar tops, the dewar vacuum manifold (here attached to a turbomolecular pump through the flex hose exiting upper left), the liquid nitrogen supply and return tubing (before the application of foam insulation), and the air cooling lines to the photometric dewars at the bottom.

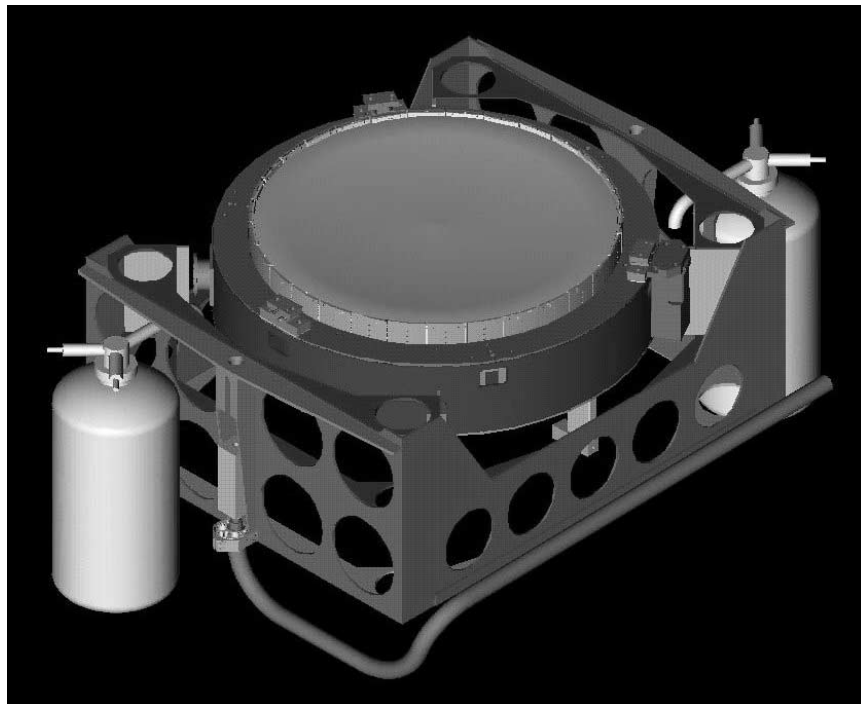


FIG. 39.—Pro/Engineer drawing of the camera with the front and rear shrouds removed and the saddle assembly as it is mounted relative to the camera. The two 10 liter intermediate supply dewars are shown mounted on the saddle, but the power supplies, which are mounted on the saddle faces adjacent to the dewars, are not shown here. Also shown is the umbilicus, the kinematic mounts, and one of the pneumatic latches (left center), which hold the camera to the telescope.

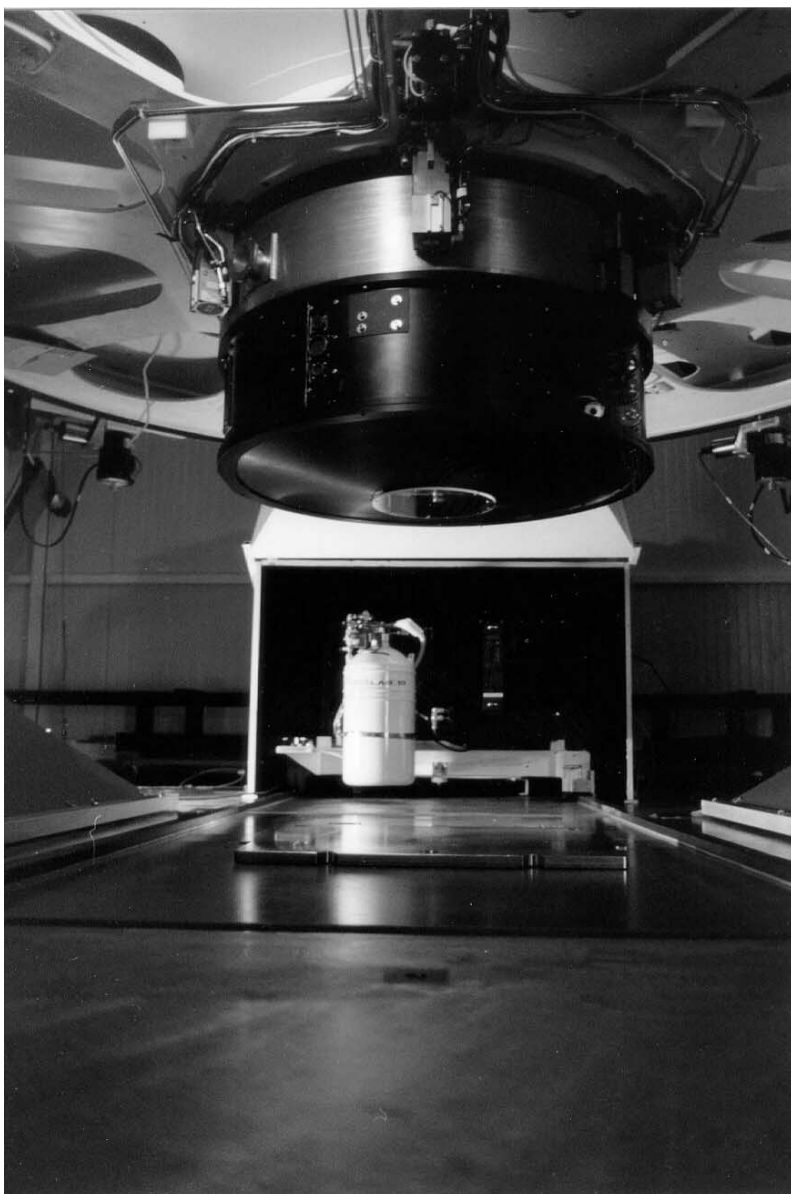


FIG. 40.—Photograph of the camera mounted alone on the telescope, with the saddle and operations cart in the doghouse in the background

camera on or off the telescope. The camera will be kept cold continuously except for times of maintenance. For serious maintenance and repairs, there is another cart (the service cart), which allows the camera to be taken to the clean room in the operations building and inverted to reach and remove the dewars (Fig. 41). This cart carries the camera alone; the saddle remains on the ops cart, though for full operation in the clean room (which is possible) the intermediate dewars and power supplies have to be removed and transported with the camera.

The camera consumes about 550 W when quiescent, and as much as 100 more at peak. The AC power is supplied by a 1 KVA motor generator through an isolating UPS. The heat dissipated is disposed of by heat exchangers, two in the camera body and three in each power supply chassis. Each power supply chassis dissipates about 160 W and the camera electronics about 220 W, though the LN₂ system in the camera disposes of more than one-half the latter. The heat exchangers are supplied with water/glycol at about 4°C below ambient by a chiller operating below the observing floor, and the instrument structure is thereby kept near

ambient temperature.

The electronics in the photometric dewars dissipate about 25 W each and those for the astrometrics about 32. One of the heat exchangers in the camera is coupled to a set of hoses through which air is blown directly into the electronics enclosures on the dewars (see Fig. 37); the other simply circulates the air in the rear camera shroud.

The communication with the outside world is reasonably simple for so complex an instrument. There are 16 data fibers, 10 for CCD data from the camera FOXIs, two for the RS-232 control signals, and four for the control of the Tbar latches by the telescope control system; AC power; water/glycol for cooling (4.5 liters minute⁻¹) and its return; low-pressure gaseous nitrogen for purge and pressurization of the intermediate dewars; vacuum and pressurized nitrogen for the dewar bellows; compressed air for the shutters; and a vacuum-jacketed liquid nitrogen line for filling the intermediate dewars. All of these are carried in the umbilical, a bundle 2.5 inches in diameter that is covered and protected by a sturdy flexible ethylene vinyl acetate hose with steel wire reinforcement.

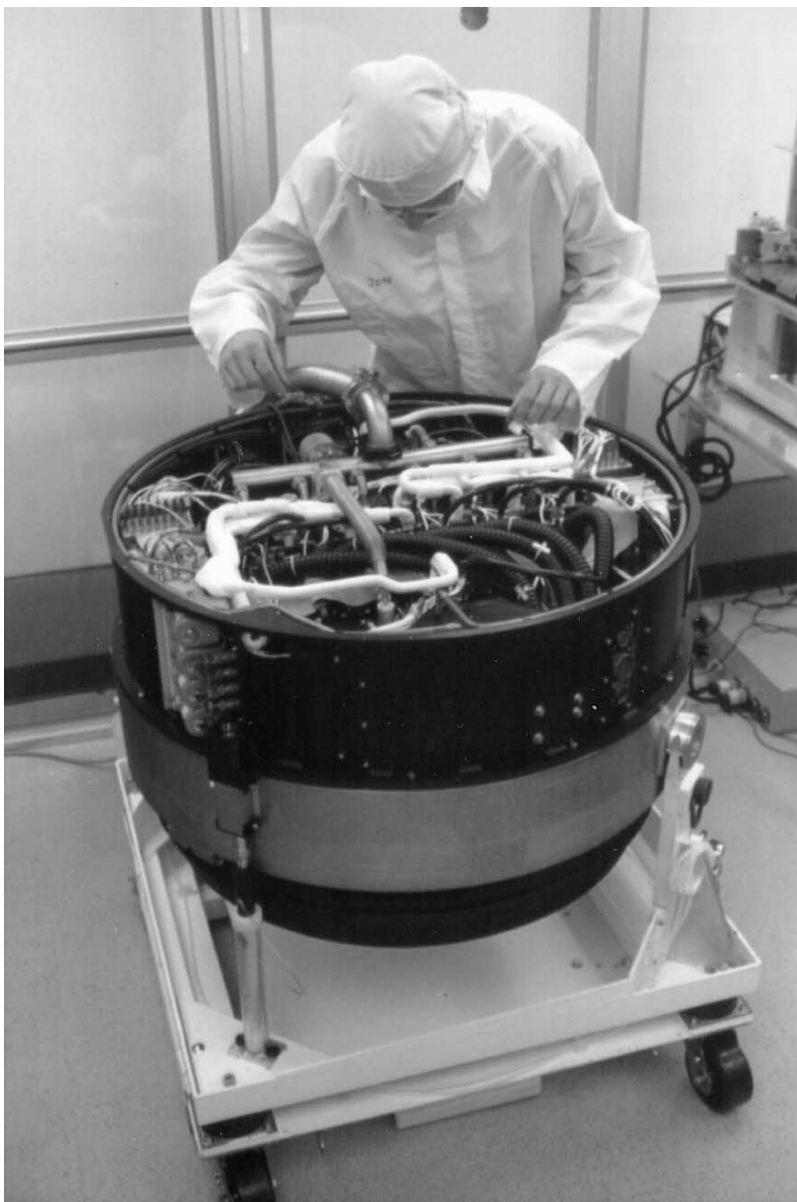


FIG. 41.—The camera inverted on the transport/service cart in the Apache Point clean room. It is shown here fully assembled except for the back cover, which is easily removed for access and for pumping the dewars, which is in progress here. The XYZ measuring engine can be seen in the upper right background.

9. CONCLUSION

We have described in this paper the construction of a large multi-CCD camera to be used in the Sloan Digital Sky Survey. The camera is currently at the Apache Point site. It has undergone extensive testing, including mechanical fit checks, mating to the data system, cold system-level tests, and final shakedown. As of this writing it has been on the sky three times, once for checkout near full moon and then two weeks later, in late 1998 May, for an official “first-light” run in the dark of the moon, and again in the next dark run in June. Though there have been the usual minor commissioning problems, no major problems have surfaced, and the data from the June dark run, taken when the telescope was much better collimated than in the May run, is quite good. The project has been both long and arduous, though very rewarding. We hope this rather detailed description will be of assistance to those building large CCD systems in the future.

The camera team would like to thank the participating institutions in the SDSS, including Princeton University, the University of Chicago, the Institute for Advanced Study, the Japanese Participation Group, Fermilab, the University of Washington, the Naval Observatory, and Johns Hopkins University, for support during often difficult times, and of course the Alfred P. Sloan Foundation and the National Science Foundation for the grants that have allowed the survey to proceed. A Grant-in-Aid for Specially Promoted Research, No. 05101002, from the Ministry of Education in Japan was awarded specifically for some aspects of the construction of this camera, and the Japanese team was supported by the Japan Society for the Promotion of Science. We also thank especially Keith Gollust for a generous gift of both money and faith that allowed the project to begin in a serious way 7 years ago, and the PI on the camera wishes to thank Barry and Bobbi Freedman and John and Karen Nichols for help at critical times that made working on the camera possible.

REFERENCES

- Abe, F. 1997, in *Variable Stars and the Astrophysical Returns of Microlensing Surveys*, ed. R. Ferlet, J. P. Maillard, & B. Raban (Paris: Frontières), 75
- Abe, F., et al. 1998, in preparation.
- Arnaud, M., et al. 1994, *Exp. Astron.*, 4, 265
- Bauer F., & de Kat, J. (for the EROS2 collaboration) 1998, in *Optical Detectors for Astronomy*, ed. J. Beletic & P. Amico (Amsterdam: Kluwer), 191
- Boroson, T., Reed, R., Wong, W., & Lesser, M. 1994, *Proc. SPIE*, 2198, 877
- Boulade, O. 1998, in *Optical Detectors for Astronomy*, ed. J. Beletic & P. Amico (Amsterdam: Kluwer), 203
- Bowen, I. S. & Vaughan, A. H. 1973, *Appl. Opt.*, 12, 1430
- Fukugita, M., Ichikawa, T., Gunn, J. E., Doi, M., Shimasaku, K., & Schneider, D. P. 1996, *AJ*, 111, 1748
- Gunn, J. E., Carr, M., Danielson, G. E., Lorenz, E. O., Lucinio, R., Nienow, V. E., Smith, J. D., & Westphal, J. A. 1987, *Opt. Eng.*, 26, 779
- Gunn, J. E., & Westphal, J. A. 1981, *Proc. SPIE*, 290, 16
- Ives, D., Tulloch, S., & Churchill, J. 1996, *Proc. SPIE*, 2654, 266
- James, E., Cowley, D., Faber, S., Hillyard, D., & Osborne, J. 1998, *Proc. SPIE*, 3355, 70
- Kashikawa, N., Yagi, M., Sekiguchi, M., Okamura, S., Doi, M., Shimasaku, K., & Yasuda, N. 1995, in *IAU Symp. 167, New Developments in Array Technology and Applications*, ed. A. G. Davis Philip, K. A. Janes, & A. R. Upgren (Dordrecht: Kluwer), 345
- Luppino, G., Metzger, M., Kaiser, N., Clowe, D., Gioia, I., & Miyazaki, S., 1996, in *ASP Conf. Ser. 88, Clusters, Lensing, and the Future of the Universe*, ed. V. Trimble (San Francisco: ASP), 229
- Miyazaki, S., 1998, *Proc. SPIE*, 3355, in press
- Schneider, D. P., Gunn, J. E., & Hoessel, J. G. 1983, *ApJ*, 264, 337
- Schneider, D. P., Schmidt, M., & Gunn, J. E. 1989, *AJ*, 98, 1951
- Sekiguchi, M., Iwashita, H., Doi, M., Kashikawa, N., & Okamura, S. 1992, *PASP* 104, 744
- Thuan, T. X., & Gunn, J. E. 1976, *PASP*, 88, 543
- Turnrose, B. 1974, *PASP*, 86, 545
- Wittman, D., Tyson, J., Bernstein, G., Lee, R., Del'Antonio, I., Fischer, P., Smith, D., & Blouke, M., 1998, *Proc. SPIE*, 3355, 626